On the phase diagram of the superconducting ferromagnet UCoGe and other unconventional superconductors

Nikitin, A.

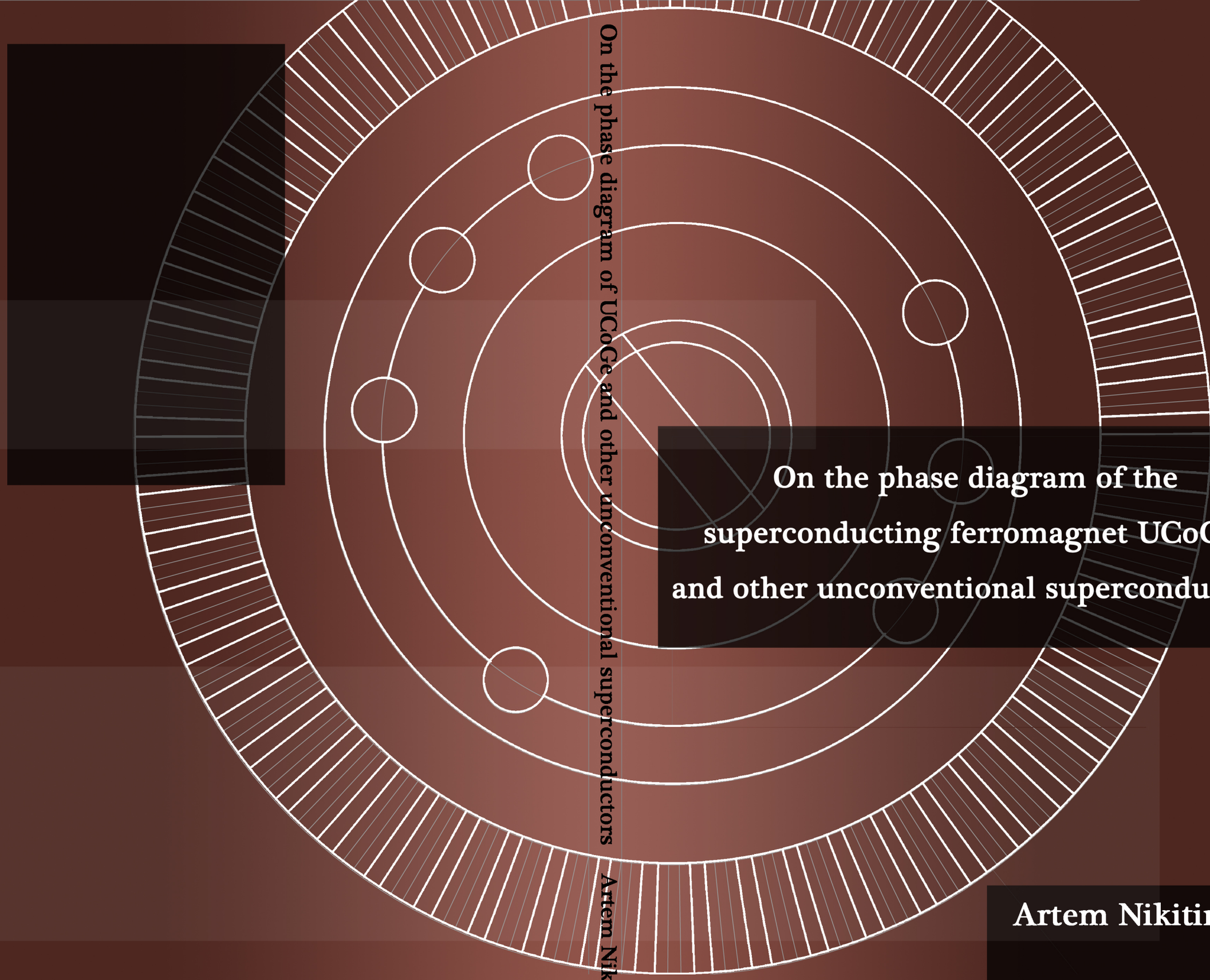

On the phase diagram of the superconducting ferromagnet UCoGe and other unconventional superconductors

Artem Nikitin

On the phase diagram of UCoGe and other unconventional superconductors Artem Nikitin

On the phase diagram of the superconducting ferromagnet UCoGe and other unconventional superconductors

Artem Nikitin

ISBN: 978-94-028-0575-8
Cover: graphical representation of the dilatometer. Cover design by Irina Dortman.

On the phase diagram of the superconducting ferromagnet UCoGe and other unconventional superconductors

ACADEMISCH PROEFSCHRIFT

ter verkrijging van de graad van doctor
aan de Universiteit van Amsterdam
op gezag van de Rector Magnificus
prof. dr. ir. K.I.J. Maex
ten overstaan van een door het College voor Promoties ingestelde commissie,
in het openbaar te verdedigen in de Agnietenkapel
op vrijdag 21 april 2017, te 12.00 uur

door

Artem Maksimovich Nikitin

geboren te Bashkortostan, Sovjet Unie

Promotiecommissie:

Promotor:	Prof. dr. M.S. Golden, Universiteit van Amsterdam
Copromotor:	Dr. A. de Visser, Universiteit van Amsterdam
Overige leden:	Prof. dr. T. Gregorkiewicz, Universiteit van Amsterdam
	Prof. dr. F.E. Schreck, Universiteit van Amsterdam
	Dr. V. Gritsev, Universiteit van Amsterdam
	Prof. dr. D. Aoki, Tohoku University
	Dr. A. McCollam, Radboud Universiteit Nijmegen
	Prof. dr. E. Brück, Delft University of Technology

Faculteit der Natuurwetenschappen, Wiskunde en Informatica

The research reported in this thesis was performed at the Van der Waals – Zeeman Institute, Institute of Physics, University of Amsterdam. This work was part of the research programme of the Foundation for Fundamental Research on Matter (FOM), which is part of the Netherlands Organisation for Scientific Research (NWO).

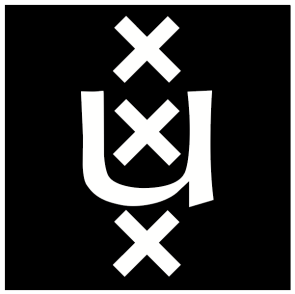

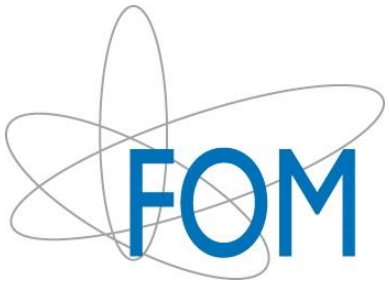

Contents

Chapter 1

Introduction

1.1 Superconductivity

Superconductivity, the phenomenon of exactly zero electrical resistance, has many applications in modern life and technologies. Superconducting magnets are used in physics for generating high magnetic fields, in medicine for magnetic resonance imaging, in chemistry for the determination of the structure of complex molecules using nuclear magnetic resonance techniques, in the field of conservation of cultural heritage, in archeology *etc*. Superconducting quantum interference devices (SQUIDs) are sensitive magnetometers used to measure extremely weak magnetic fields. The use of SQUIDs is widely spread from detecting signals from neural activity inside the brain to oil prospecting and mineral exploration. Other more exotic applications are superconducting high voltage cables which can transfer electricity without losses and powerful superconducting motors, that are being developed intensively nowadays. All of this would not be possible without an extensive theoretical investigation of the phenomenon of superconductivity and the experimental search for novel superconducting materials.

Superconductivity is observed in many materials. The experimental discovery [1] of zero resistance of mercury by H. Kamerlingh Onnes was made in 1911, but it took almost half a century to understand the physics behind it. A phenomenological approach to superconductivity has been proposed by Ginzburg and Landau in 1950 [2]. It is based on the idea that the superconducting phase transition is, in the absence of a magnetic field, a thermodynamic second-order phase transition. Thus, one can apply the general theory of second-order phase transitions to superconductivity. This eventually led to the distinction between type I and type II superconductors. In 1957 Bardeen, Cooper and Schrieffer (BCS) introduced a microscopic approach in explaining superconductivity [3]. It is based on an attractive rather than a repulsive interaction between two electrons with anti-parallel spin and opposite momentum in what is called a Cooper pair. The effective attraction is due to the interaction of the electrons with lattice vibrations. The phonon mediated Cooper pairs condense into a boson-like state. The condensation of the electron pairs can be seen as a superfluid ground state. In the past decades, the number of materials that cannot be explained by conventional BCS theory is growing. Unconventional superfluidity has been found in ^{3}He [4, 5], unconventional superconductivity in heavy-fermion systems [6, 7, 8, 9, 10, 11, 12, 13, 14], cuprates [15, 16], iron pnictides [17, 18, 19, 20] and possibly H_2S under high pressure [21].

Magnetism and superconductivity are mutually exclusive for conventional superconductors. Surprisingly, their coexistence in a single phase has been realized in a few materials: the superconducting ferromagnets (SCFMs) UGe_2 [12], URhGe [11] and UCoGe [22]. In these systems the same f-electrons are responsible for band ferromagnetism and superconductivity [23]. The emergence of this robust class of superconducting compounds requires novel theoretical insights going beyond the standard BCS formalism. A theoretical prediction of p-wave or equal-spin pairing superconductivity in itinerant ferromagnets [24] was, in fact, made long before the first SCFM were experimentally realized. Here the exchange of longitudinal spin fluctuations near a ferromagnetic quantum critical point (QCP) was proposed as a pairing mechanism for triplet Cooper pairs. However, this simple model cannot qualitatively explain the pressure–magnetic field phase diagrams of the SCFMs. Later on, more sophisticated theoretical models based on spin fluctuation approaches have appeared [25, 26, 27].

Topological superconductors belong to another fascinating class of compounds. The idea of introducing topology into condensed matter physics comes from the early 70's by Thouless and Kosterlitz [28, 29] and was recognised by the 2016 Nobel Prize for physics [30]. They identified a completely new type of phase transitions in two-dimensional (2D) systems in which topological defects play a crucial role. The theory can be applied to certain kinds of magnets and to superconducting and superfluid films and is also important for understanding the quantum theory of one-dimensional systems at very low temperatures. A few years ago, it was realized that topological order can emerge quite generally in specific two and three-dimensional (3D) materials – topological insulators (TI) [31, 32]. In 3D topological insulators, the bulk is insulating, 2D edge (or surface) states – protected by a non-trivial Z_2 topology – are conducting. The concepts developed for TIs can also be applied to superconductors, due to the direct analogy between topological band theory and superconductivity: the Bogoliubov - de Gennes Hamiltonian for the quasiparticles of a SC has a close similarity to the Hamiltonian of a band insulator, where the superconducting gap corresponds to the gap of the band insulator [33, 34]. Topological superconductivity can be viewed as a state that supports a full superconducting gap in the bulk and these systems possess surface states protected by symmetries at the boundaries of the system. The topological surface states of such superconductors can host Majorana zero modes. The experimental observation of Majorana zero mode states in solid-state systems has been heralded as

the realization of building blocks for novel quantum computers [35]. Experimentally, the most well-known candidate for topological superfluidity is the B phase of ^{3}He [36, 37, 38]. Promising candidates for topological superconductivity can be found among the doped 3D TIs $Cu_xBi_2Se_3$ [39, 40, 41] and $Sr_xBi_2Se_3$ [42], the doped semiconductor $Sn_{1-x}In_xTe$ [43], the half-Heusler platinum bismuthide family with 111 stoichiometry LaPtBi [44], YPtBi [45, 46], LuPtBi [47], and the half-Heusler palladium bismuthide family REPdBi [48, 49, 50, 51, 52].

1.2 Outline

In Chapter 2, the theoretical background of the thesis is discussed. An introduction to the concept of quantum criticality and quantum phase transitions is given. A brief overview of different types of superconducting states is presented. Then we consider the upper-critical field for different types of superconductors, including conventional and unconventional systems. The theoretical aspects of the coexistence of superconductivity and ferromagnetism, as well as recent experimental discoveries of such materials, are presented. Next, the phase diagram of UCoGe, the most recently discovered ferromagnetic superconductor, is discussed together with its theoretical explanation. The Grüneisen parameter, relevant for the thermal expansion measurements we will present in Chapter 4, is introduced. In the last part of the chapter, we address some aspects of the topological insulators and topological superconductors.

Chapter 3 summarizes the experimental techniques used in this thesis. The measurement methods, such as resistivity, susceptibility, torque magnetometry and thermal expansion, are discussed. The calibration of the dilatometer and the calibration of the angle reader of the piezo-rotators are reported in detail. The chapter ends with sample preparation techniques and an overview of the characteristics of the prepared UCoGe crystals.

In Chapter 4, measurements of the coefficient of linear thermal expansion of the superconducting ferromagnet UCoGe are reported. The superconducting and ferromagnetic phase diagram has been determined by accurate dilatometry in magnetic fields directed along the crystallographic axes of a single crystalline sample. An S-shape of the upper-critical field for $B \parallel b$ axis with the enhancement of superconductivity above 6 T was confirmed. A shift of the Curie temperature towards lower

temperatures with increasing magnetic field was found. The data are discussed in terms of spin fluctuation mediated superconductivity.

In Chapter 5, the properties of UCoGe in applied magnetic fields were investigated. Several single crystalline samples were studied by the magnetoresistance, the magnetostriction and torque magnetometry measurements for a magnetic field applied along the c-axis. We have confirmed an anomaly B^* = 9 T and associate it with a Lifshitz transition. Shubnikov-de Haas oscillations were detected for $B \parallel c$ axis.

Chapter 6 is focused on a high-pressure transport study of the upper-critical field of the topological superconductor $Sr_{0.15}Bi_2Se_3$. The resistivity was measured for magnetic fields directed along two orthogonal directions in the trigonal basal plane. The critical pressure for suppression of superconductivity $p_c \sim 3.5$ GPa was determined. The pronounced two-fold basal-plane anisotropy of the upper-critical field is enhanced under pressure. The data reveal that the unconventional superconducting state with broken rotational symmetry is robust under pressure.

In Chapter 7, a study of the magnetic and electronic properties of the noncentrosymmetric half-Heusler antiferromagnet HoPdBi is reported. Magnetotransport measurements revealed Shubnikov-de Haas oscillations which show that HoPdBi has a low carrier concentration. The magnetic phase diagram in the field-temperature plane has been determined by transport, magnetization and thermal expansion measurements. Superconductivity at T_c = 0.75 K is discovered within the antiferromagnetic phase (T_N = 2.0 K). Ac-susceptibility measurements provide solid evidence for bulk superconductivity. The upper-critical field shows an unusual linear temperature variation. Electronic structure calculations classify HoPdBi as a new topological semimetal, with a non-trivial band inversion.

Chapter 2

Theoretical aspects

In this chapter we discuss the relevant theoretical background for the description of the experimental results reported in this thesis. We present a brief discussion of heavy-fermion physics, as well as its relation to quantum criticality and quantum phase transitions. Next, we turn to unconventional superconductivity and different models for the upper-critical field that can be used to delineate the superconducting states. Finally, we present some basic aspects of the three different superconductors that we have studied. As regards UCoGe we discuss superconducting ferromagnets, and their unusual upper-critical field. For $Sr_xBi_2Se_3$ and HoPdBi we present several basic aspects of their topological nature.

2.1 Introduction

In this chapter, we will discuss the relevant theoretical background for the three different compounds UCoGe, $Sr_xBi_2Se_3$ and HoPdBi that are investigated in this thesis. These three systems are united by the fact that they become superconducting at low temperatures.

UCoGe belongs to the family of superconducting ferromagnets. It is also a moderately enhanced heavy-electron system. In heavy-electron compounds, the electrons of the partially filled $4f$ and $5f$ shells play a crucial role in the physical properties. The collective behaviour of these electrons can result in itinerant antiferromagnetism or ferromagnetism, and/or unconventional superconductivity. The Fermi-liquid model describes the properties of such strongly correlated electron systems.

$Sr_xBi_2Se_3$ is a promising candidate for the experimental realisation of topological superconductivity. The parent compound of this superconductor is Bi_2Se_3, a well-known topological insulator. A small amount of Sr intercalated between the bismuth selenide quintuple layers makes it a superconductor with $T_{sc} = 3.0$ K.

HoPdBi has a noncentrosymmetric crystal structure and exhibits superconductivity within an antiferromagnetic state. In addition, band structure calculations show that it has a non-trivial band inversion. All of this makes HoPdBi a unique tool to investigate the interplay between topology and the superconducting state.

2.2 Basic properties of heavy-fermion systems

The idea of describing the electronic properties of solid state systems by quasiparticles was introduced by Landau in 1930. A quasiparticle is defined as the collective excitations of electrons induced by various interaction mechanisms. The complex movement of the electrons in the crystal may be formalised as the effective interaction of the quasiparticles.

Heavy-fermion systems are defined as a class of intermetallic compounds characterised by a large value of the quasiparticle mass [53]. The broad use of this term refers to electron masses which are 10 to 1000 times larger than the free electron mass. Their properties stem from the electrons in the partially filled f-orbitals of rare earth or actinide compounds, which at high temperatures act as localised magnetic moments [54]. Upon decreasing the temperature these localised magnetic moments become screened by the cloud of conduction electrons, forming eventually a strong

elastic electron scattering potential [55]. The competition between the formation of the magnetic lattice and the screening effect of the conduction electrons causes the formation of heavy carriers. This can be seen as a monotonic increase of the resistivity upon cooling, while coherence sets in at low temperatures. At high temperatures, these systems behave like paramagnets. Upon cooling a magnetically ordered state is favourable. At low temperatures, the magnetic susceptibility saturates and attains an enhanced value compared to normal metals. At the same time, the electronic contribution γ to the specific heat reaches a large value. In some heavy-fermion compounds, a superconducting transition occurs at low temperatures. The presence of strong electron correlations in these systems provides arguments for a superconducting pairing mechanism that is not based on the conventional electron-phonon coupling, but rather on a spin fluctuation mechanism.

2.3 Quantum criticality

A conventional or classical phase transition can be described by an order parameter, first introduced by Landau. This parameter is a thermodynamic quantity that depends on the state of the system. Its thermodynamic average is equal to zero in the disordered phase and to non-zero in the ordered phase, *e.g.* the ordered moment of a ferromagnet or the energy gap of a superconductor. Conventional phase transitions occur at finite temperature when the growth of random thermal fluctuations leads to a change in the physical state of a system.

Condensed matter physics research over the past few decades has revealed a new class of phase transitions, called quantum phase transitions (QPTs). QPTs are a special class of continuous phase transitions that take place at absolute zero. Major examples are materials where the phase transition temperature has been driven to zero by a non-thermal control parameter, r, such as pressure, magnetic field, chemical doping or electron density. A schematic phase diagram for a QPT is shown in Fig. 2.1. By changing the control parameter one is able to tune the system to a transition point, the quantum critical point (QCP). The quantum fluctuations are dominant at very low temperatures as long as their energy is larger compared to the energy of the thermal fluctuations: $\hbar\omega >> k_B T$.

Heavy-fermion materials are unique tools for the investigation of QPTs. In these systems, the Kondo effect, that quenches the local moment of the f-electrons by

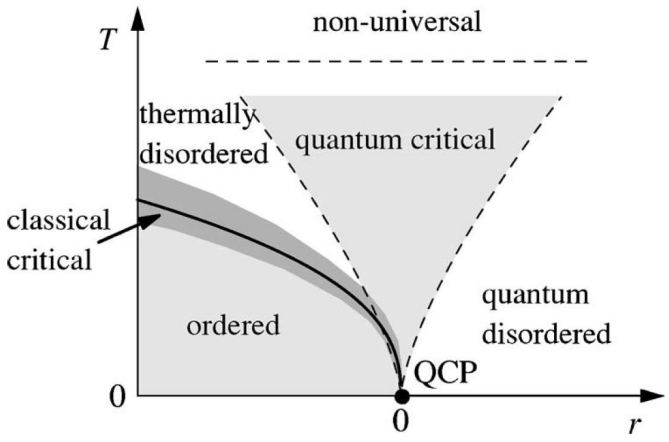

Figure 2.1: Generic phase diagram in the vicinity of a continuous quantum phase diagram. The horizontal axis represents the control parameter r used to tune the system through the QCP; the vertical axis is the temperature T. Dashed lines indicate the boundaries of the quantum critical region. The solid line marks the finite-temperature boundary between the ordered and disordered phases. Close to this line, the critical behaviour is classical. The picture is taken from Ref. [56].

conduction electron screening, competes with the Ruderman-Kittel-Kasuya-Yosida (RKKY) interaction [57, 58]. Changing the non-thermal control parameter r, for example, the magnetic field [59, 60, 61, 62, 63], pressure [64, 65, 66, 67] or chemical doping [68, 69, 70, 71, 72, 73], suppresses the magnetic ordering and tunes the system to the QPT.

2.4 Unconventional superconductivity

A microscopic theory of superconductivity (SC) has been put forward by Bardeen, Cooper and Schrieffer (BCS) [3]. They proposed that the electrons bind into Cooper pairs at low temperatures in the superconducting state in order to lower the ground state energy. A Cooper pair is a bound state of two electrons which is formed near the Fermi level by an attractive interaction. In the standard BCS theory the attractive interaction is mediated by lattice vibrations. The conduction electrons are fermions with spin $s = \pm 1/2$ and condense into boson-like particles with a total spin S = 0 or 1. The total angular momentum of the Cooper pairs can be L = 0, 1, 2, 3,... Conventional superconductors or s-wave superconductors are spin-singlet (S = 0)

with $L = 0$ and a spin-wave function:

$$\psi_{singlet} = \frac{1}{\sqrt{2}} \left(|\uparrow\downarrow\rangle - |\downarrow\uparrow\rangle \right) \tag{2.1}$$

Superconductors with a spin-singlet state and $L = 1$ are called d-wave. In the case of a spin-triplet state ($S = 1$) the spin part of the wave-function of the Cooper pairs is written as:

$$\psi_{triplet} = \begin{cases} |\uparrow\uparrow\rangle \\ \frac{1}{\sqrt{2}} \left(|\uparrow\downarrow\rangle + |\downarrow\uparrow\rangle \right) \\ |\downarrow\downarrow\rangle \end{cases} \tag{2.2}$$

The triplet-state with $L = 1$ is called p-wave and the one with $L = 3$ f-wave. Here $|\uparrow\uparrow\rangle$ and $|\downarrow\downarrow\rangle$ are called the equal-spin pairing (ESP) states.

The s-wave superconducting state is fully explained by the standard BCS theory. Unconventional superconductivity (d-wave, p-wave) has been found in many materials. Important examples are ^{3}He [5, 4], heavy-fermion SCs [6, 7, 8, 9, 10, 11, 12, 13, 14], high-temperature SCs (cuprates [15, 16] and iron pnictides [17, 18, 19, 20]).

2.5 Upper-critical field

The upper-critical field, $B_{c2}(0)$, is the magnetic field at which superconductivity is completely suppressed in a type II superconductor at $T = 0$ K. The slope of the upper-critical field at T_{sc}, $B'_{c2} = -\partial B_{c2}/\partial T|_{T_{sc}}$, and its temperature variation carries important information about the superconducting state. In a sufficiently large magnetic field all the Cooper pairs are broken. The standard analysis of B_{c2} is based on the Ginzburg-Landau (GL) theory for type II superconductors under the assumption of a spherical Fermi surface. The slope of B_{c2} can be expressed in SI units by [74]

$$B'_{c2} = -\left.\frac{\partial B_{c2}}{\partial T}\right|_{T_{sc}} = R(l) \left(1.18 \times 10^{35} \frac{\gamma^2 T_{sc}}{S_s^2} + 4480 \gamma \rho_0 \right) \tag{2.3}$$

where S_s is the part of the Fermi surface on which Cooper pairs are formed; the parameter $R(l)$ varies between $R = 1$ and 1.17 in the dirty and in the clean limit, respectively, where l is the mean free path of the quasiparticles; γ is the Sommerfeld term in the electronic specific heat (expressed per unit volume); ρ_0 is the residual resistance. In the clean limit (ρ_0 small, $l \gg \xi$, where ξ is the coherence length)

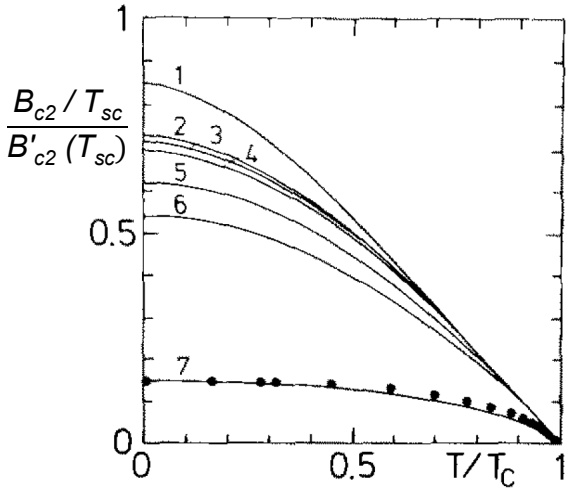

Figure 2.2: Normalized upper-critical field as a function of the residual temperature. Curve labels indicate: 1 – triplet superconductor without Pauli limiting, polar state; 2 – conventional superconductor, clean limit; 3 – triplet superconductor, Scharnberg-Klemm limit; 4 – WHH model: conventional superconductor without Pauli limiting, dirty limit; 5 – triplet superconductor, Anderson-Brinkman-Morel (ABM) state; 6 – polar state (as 1) and conventional state (as 4) with strong pair breaking; 7 – B_{c2} of $CeCu_{2.6}Si_2$. The picture is adapted from Ref. [75].

the first term of B'_{c2} dominates. In the dirty limit (ρ_0 large, $l \ll \xi$) the second term dominates. This analysis has been applied to A15 compounds (Nb_3Sn and V_3Si) [74] and heavy-fermion systems [75, 76].

There are two main mechanisms, by which a magnetic field interacts with the electrons in the superconducting state. Both are pair breaking and lead to the destruction of superconductivity at a certain critical field. These mechanisms are 1) interaction of the field with the orbital motion of the electrons, the so-called orbital pair breaking, and 2) interaction with the spins of the electrons, the so-called Pauli limiting.

Orbital pair breaking occurs in all superconductors. It determines, in the absence of any other pair-breaking effects, the initial slope B'_{c2} at T_{sc}. The B_{c2} value when $T \to 0$ varies between $B_{c2}(0) = 0.693 \times B'_{c2}T_{sc}$ for a conventional superconductor in the dirty limit [77] (Werthamer, Helfand and Hohenberg (WHH) model), and $B_{c2}(0) = 0.850 \times B'_{c2}T_{sc}$ for a polar triplet state in the p-wave model [78].

The interaction of the magnetic field with the Cooper pairs in the superconducting state depends on the spin type of the state. In a conventional supercon-

ductor (S = 0, L =0) the normal state becomes energetically more favourable for the system as soon as the magnetic energy due to the Pauli susceptibility reaches the condensation energy $(1/2\mu_0)B_c^2$ of the superconductor (the Pauli limiting effect, $B_{c2}^p = 1.84 \times T_{sc}$) [79]. In some triplet states (S_z = 1) no Pauli limiting occurs, as long as the spin part of the order parameter can rotate freely with respect to the orbital part. In heavy-fermion superconductors, that consist of atoms with high atomic number, the spin-orbit coupling is strong. This can lead to a situation in which the spin part of the order parameter cannot orientate itself freely with respect to the orbital part. In this way, an anisotropic Pauli limiting can occur even in a triplet superconductor. Strong spin-orbit scattering, on the other hand, may cause a reduction of Pauli limiting in unconventional superconductors.

In Fig. 2.2 the upper-critical field obtained for different models is plotted on the same reduced scale. Among the presented models are the Anderson-Brinkman-Morel [80] and Scharnberg-Klemm [81] limits. The most relevant theoretical models for our research are the WHH [77] (curve 4 in Fig. 2.2) and polar triplet state [78] (curve 1 in Fig. 2.2).

2.6 Superconducting ferromagnets

The first mentioning of superconducting ferromagnets (SCFMs) was in 1957 [82]. In this work, it was pointed out that superconductivity and ferromagnetism (FM) can be observed only under extraordinary circumstances, such as a sufficiently small ordered moment m_0. Later, in the 80's it was theoretically predicted that SC with ESP states (p-wave superconductivity) could exist in itinerant ferromagnets close to a FM QCP [24]. Here the pairing interaction is mediated by the exchange of longitudinal spin fluctuations, and the resulting state is analogous to the $A1$ phase of superfluid ^{3}He. In the last 15 years, the coexistence of superconductivity and ferromagnetism was reported for the uranium intermetallics: UGe_2 [11], URhGe [12] and UCoGe [22].

The main idea behind the coexistence of SC and FM near a FM QCP rests in spin fluctuation models [24]. The magnetic state can be understood in terms of a Hubbard-type exchange interaction I and a Stoner enhancement factor $S = (1 - I)^{-1}$. At a critical value I = 1, a second order phase transition occurs from the paramagnetic (PM) phase ($I < 1$) to the FM phase ($I > 1$), see Fig. 2.3(a). At very low

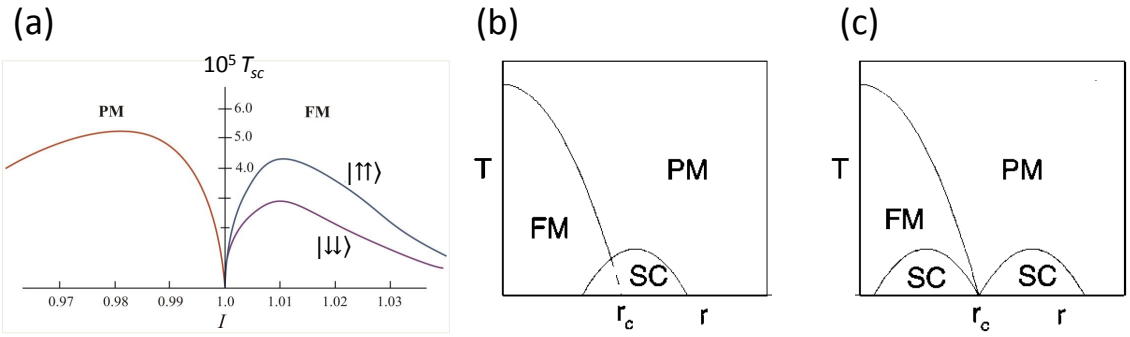

Figure 2.3: Panel (a): Theoretical phase diagram of a p-wave SC. Superconducting transition temperature T_{sc} as a function of the exchange interaction parameter I. Superconductivity is found in the FM and PM state. $|\uparrow\uparrow\rangle$ and $|\downarrow\downarrow\rangle$ indicate the ESP components. The picture is adapted from Ref. [24]. Panel (b) and (c): Temperature (T) – control parameter (r) phase diagram of a SCFM, where the superconducting transition temperature T_{sc} is finite (b) at the QCP at r_c and SC emerges in both the FM and PM phases (c) centered around the QCP at r_c. The picture is taken from Ref. [83].

temperatures p-wave pairing is possible in the FM state with different T_{sc}'s for the spin up $|\uparrow\uparrow\rangle$ and spin down $|\downarrow\downarrow\rangle$ states. This implies two superconducting phases can be present [24, 27, 26]. However, the possible emergence of these two superconducting phases depends sensitively on the details of the band structure. A schematic picture of the realisation of two superconducting domes, one in the ferromagnetic state and the other in the paramagnetic phase, is given in Fig. 2.3(c) [25, 83]. This diagram partly resembles the case of UGe_2. However, superconductivity was not observed in the PM phase in the case of UGe_2. A possible explanation is that ferromagnetic spin waves (magnons) couple to the longitudinal magnetic susceptibility which results in an enhancement of T_{sc} in the FM phase [25, 83]. The resulting phase diagram where SC coexists with FM, leading to a superconducting dome and nonzero T_{sc} at the QCP is sketched in Fig. 2.3(b). This represents the case of UCoGe.

2.6.1 UCoGe

In this section, we will focus on UCoGe. This material orders ferromagnetically at T_C = 3 K and becomes superconducting at T_{sc} = 0.6 K. Muon spin rotation/relaxation [84], nuclear magnetic resonance and nuclear quadrupole resonance [85, 86] measurements provide solid evidence that SC is driven by ferromagnetic spin fluctua-

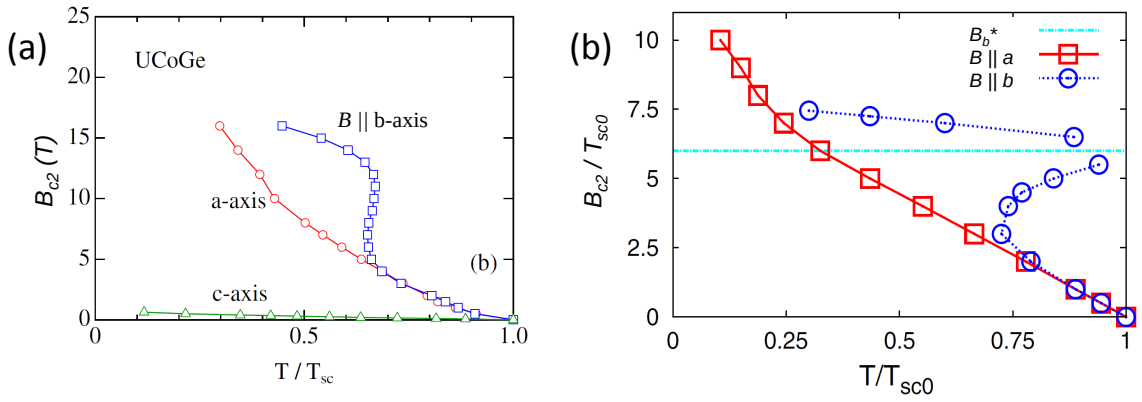

Figure 2.4: Panel (a): Temperature variation of the upper-critical field for B parallel to the a-, b- and c-axes. The temperature is normalized by the superconducting critical temperature T_{sc} at zero field. The picture is adapted from Ref. [87]. Panel (b): Model curves of the temperature variation of the upper-critical fields for $B \parallel a$-axis (red curve) and b-axis (blue curve) of UCoGe. The dashed line indicates the critical magnetic field B_b*. The picture is adapted from Ref. [88].

tions and that SC and FM coexist microscopically. Magnetoresistivity measurements on high-quality single crystals of UCoGe with fine tuning of the magnetic field direction show an anomalous behaviour of the upper-critical field [87]. The magnetic field - temperature phase diagram is shown in Fig. 2.4(a). An unusual S-shape of the upper-critical field is observed for the magnetic field directed along the b-axis (orthorhombic crystal structure). It was proposed that the origin of the S-shaped B_{c2}^b curve is closely related to the decrease of the Curie temperature with increasing field along the b-axis.

From a theoretical point of view, based on a scenario of spin-fluctuations mediated superconductivity, it is rather natural to expect an S-shaped B_{c2} curve or even reentrant superconductivity, once one simply takes into account the enhancement of spin fluctuations by the reduction of T_C [88]. For small magnetic fields, triplet superconductivity will coexist with ferromagnetism as in the zero-field case, and it is robust against the Pauli depairing effect under magnetic fields ($\perp m_0$) due to the exchange splitting of the Fermi surface, as pointed out by Mineev [89]. The description of the sharp angular dependence of the upper-critical field was developed in the framework of a specific Ising-type itinerant-electron interaction approach. A single-band model with pairing between spin-up electrons only was considered. The B_{c2} angular dependence was obtained by solving the Eliashberg equations [90]. In addition, the Dzyaloshinskii-Moriya interaction arising from the zigzag structure

of UCoGe was taken into account. As a result, it was shown (see Fig. 2.4(b)) that superconductivity can survive above B_b* where there is no exchange splitting of the Fermi surface [88]. B_b* is the critical magnetic field at which the ferromagnetism along the b-axis is suppressed.

2.7 Grüneisen parameter and Ehrenfest relation

The Grüneisen parameter is defined [91, 92] as:

$$\Gamma = \frac{V_m}{\kappa_T}\frac{\beta}{c}, \tag{2.4}$$

where V_m is the molar volume, κ_T is the bulk modulus, β is the volume expansion and c is the specific heat. The Grüneisen parameter expresses the system's volume dependence to external parameters, such as temperature or magnetic field [93, 94]. In the case that only one relevant energy scale is present, Γ is constant [95]. This comes from the fact that at low temperatures the specific heat and the volume expansion exhibit the same temperature variation, for example, the lattice or phonon contribution ($\propto T^3$) or electronic term ($\propto T$). The bulk modulus κ_T is weakly temperature dependent. The Grüneisen parameter gives an estimate of the volume dependence of the dominant energy scale of the material.

The Ehrenfest relation can be defined as:

$$\frac{dT_{C,sc}}{dp} = \frac{V_m \Delta\beta}{\Delta c / T_{C,sc}} \tag{2.5}$$

where $T_{C,sc}$ is the Curie or the superconducting transition temperature, p is pressure, $\Delta\beta$ is the step in the coefficient of the volume expansion at a critical temperature, and $\Delta c/T_{C,sc}$ is the step in the specific heat at the critical temperature divided by T. With help of the Ehrenfest relation the initial pressure dependence of the critical temperatures can be calculated.

2.8 Topological superconductors

In topological insulators (TIs) an unusual state of quantum matter is realised that can be distinguished by topological invariants of the bulk band structure, rather

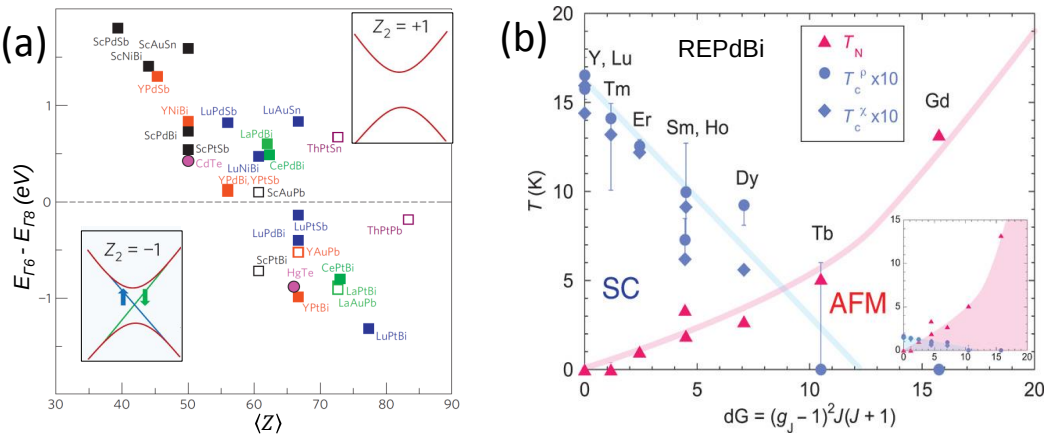

Figure 2.5: Panel (a): The band inversion strength for several half-Heusler compounds defined by the energy difference $E_{\Gamma 6} - E_{\Gamma 8}$ as a function of the average spin-orbit coupling strength represented by the average nuclear charge $\langle Z \rangle$. When $E_{\Gamma 6} - E_{\Gamma 8} > 0$, there is no band inversion (upper inset), whereas $E_{\Gamma 6} - E_{\Gamma 8} < 0$, band inversion is present (lower inset). The picture is adapted from Ref. [96, 97]. Panel (b): Evolution of superconducting and antiferromagnetic ground states of the REPdBi (RE: rare earth) series as a function of de Gennes factor $dG = (g_J - 1)^2 J(J+1)$, where g_J is the Landé factor and J is the total angular momentum of the R ion. The plotted T_c is scaled by a factor of 10. The picture is taken from Ref. [51].

than by spontaneously broken symmetries [98, 99, 100]. TIs have a full insulating gap in the bulk, but topologically protected gapless surface or edge states on the outside. It was predicted [101] that the family of Bi_2Se_3, Bi_2Te_3 and Sb_2Te_3 alloys should be topological insulators. This was experimentally confirmed by mapping the surface band structure of Bi_2Se_3 using angle resolved photoemission spectroscopy (ARPES) [102, 103]. In fact, not only the binary Bi-based compounds have topologically protected surface states. Electronic structure calculations show that several half-Heusler compounds with 111 stoichiometry also exhibit topological band inversion [96, 97]. The band inversion takes place between the twofold-degenerate s-like Γ_6 and fourfold-degenerate p-type Γ_8 energy states and depends strongly on the magnitude of the spin-orbit coupling as is shown in Fig. 2.5(a). The systems can be either topologically non-trivial, $\Gamma_6 - \Gamma_8 < 0$, or topologically trivial, $\Gamma_6 - \Gamma_8 > 0$. Amongst these topologically non-trivial half-Heusler compounds, some materials are found to be superconducting: YPtBi [45, 46], LaPtBi [44], LuPtBi [47], and REPdBi [48, 49, 50, 51, 52, 104], where RE = Er, Ho, Tm, Yb and Lu (see Fig. 2.5(b)).

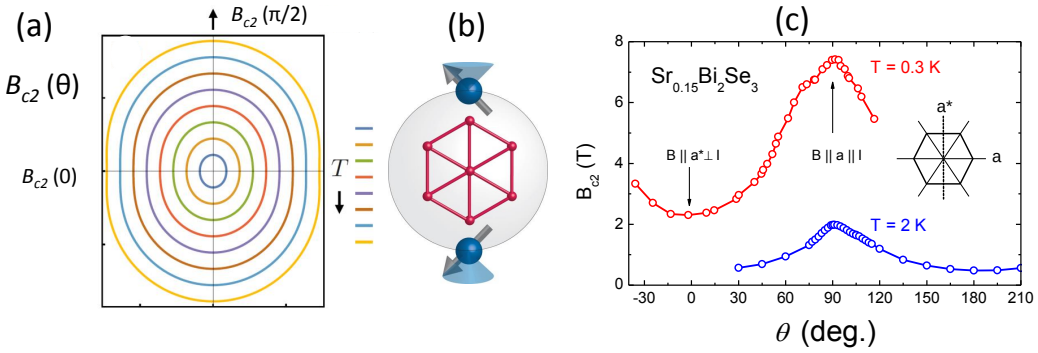

Figure 2.6: Panel (a): Calculated polar plot of the angular dependence of the upper-critical field, $B_{c2}(\theta)$, in the presence of a symmetry-breaking field (in arbitrary units of B). Different curves represent different temperatures. The picture is taken from Ref. [105]. Panel (b): Pictorial representation of spin-triplet Cooper pairs in the superconductor $Cu_xBi_2Se_3$, with zero total spin projection along a particular direction (that is the vertical axis) in the lattice plane. The picture is taken from Ref. [106]. Panel (c): Angular variation of B_{c2} in the basal plane (aa^*-plane) for $Sr_{0.15}Bi_2Se_3$ at temperatures as indicated. The data are obtained from magnetoresistance measurements at fixed T. The angle $\theta = 0^\circ$ corresponds to $B \parallel a^* \perp I$ and $\theta = 90^\circ$ to $B \parallel a \parallel I$. The a and a^* directions in the hexagonal basal plane are defined as in the figure in the upper right corner. The picture is taken from Ref. [42].

Another interesting family of potential topological superconductors can be found among the doped TI Bi_2Se_3: $Cu_xBi_2Se_3$ [39], $Sr_xBi_2Se_3$ [107], $Nb_xBi_2Se_3$ [108] and $Tl_xBi_2Se_3$ [109]. The first compound is the most well studied. A small amount (typically 10%) of Cu (Sr, Nb) intercalated into the van der Waals gaps between the Bi_2Se_3 quintuple layers makes the system superconducting. ARPES experiments on $Cu_xBi_2Se_3$ show that the topological character is preserved [110]. Recent field-angle dependent magnetotransport [42] and calorimetry [111] measurements reveal a large anisotropy of the upper-critical field when the magnet field is rotated in the basal plane of the trigonal crystal structure. The large two-fold anisotropy, while six-fold is anticipated, cannot be explained with the Ginzburg-Landau anisotropic effective mass model or flux flow induced by the Lorentz force. The rotational symmetry breaking of B_{c2} indicates unconventional superconductivity with odd-parity spin-triplet Cooper pairs (Δ_4-pairing) recently proposed for rhombohedral topological superconductors [112]. Δ_4 states are predicted to be nematic superconducting states with a non-zero nematic order parameter [113].

The measurement of the upper-critical field is a direct method of detecting nematic superconductivity. The theoretical calculations of B_{c2} within the framework

of Ginzburg-Landau theory demonstrated that the upper-critical field exhibits a twofold anisotropy with characteristic angle and temperature dependence when the degeneracy of the two components is lifted [105]. Contrary to typical GL theories which have an emergent U(1) rotational symmetry obscuring the discrete symmetry of the crystal, the theory of two-component superconductors in trigonal D_{3d} crystals reflects the true crystal rotation symmetry. The resulting angular variation of B_{c2} is shown in Fig. 2.6(a) with comparison to the experimentally observed B_{c2} of $Sr_{0.15}Bi_2Se_3$ (Fig. 2.6(c)). The superconducting state is formed by spin-triplet pairing between electrons on two different orbitals, with the property that the total spin projection of the Cooper pair is zero along certain in-plane directions, as shown in Fig. 2.6(b). Nematic superconductivity for this materials is predicted to possess a unique topological nature associated with odd parity.

Chapter 3

Experimental methods

In this chapter we focus on the experimental techniques used in this thesis. The cryogenic equipment and the measurement methods, among which resistivity, susceptibility, torque magnetometry and thermal expansion are presented. Special attention is given to the design and construction of a new dilatometer that enables us to measure the thermal expansion down to very low temperatures (30 mK). We present its calibration and discuss its performance. Moreover, the dilatometer can be rotated in the magnetic field using a piezo-electric motor. We present the design of the rotators and a dedicated rotation gear mechanism. The chapter ends with a description of the sample preparation techniques and an overview of the sample characteristics of the prepared polycrystalline and single crystalline UCoGe samples.

3.1 Cryogenics

Low temperature experiments were performed using the following experimental setups.

A Physical Property Measurements System (PPMS, Quantum Design), in which magnetic and transport measurements were carried out in the temperature range 1.8 - 300 K. The PPMS is equipped with a superconducting magnet with a field up to 9 T.

A ^{3}He refrigerator, for temperatures in the range $T = 0.24 - 10$ K (Heliox, Oxford Instruments) and magnetic fields up to 14 T. A calibrated RuO_2 thermometer and a heater were mounted close to the sample and read out by an ORPX resistance bridge. A new set of low resistance wires was mounted in the Heliox insert to supply the driving voltage of the piezoelectric rotators. In the Heliox the following measurements were made: resistivity, ac-susceptibility, thermal expansion, magnetostriction and torque magnetometry.

A ^{3}He–^{4}He dilution refrigerator (Kelvinox, Oxford Instruments), for temperatures in the range $T = 0.03 - 1$ K and B up to 17 T. A multi-purpose sample platform was mounted with a temperature control set-up (thermometer-heater) similar to the one used in the Heliox. Magnetoresistance, torque magnetometry and thermal expansion measurements were carried out in the Kelvinox.

In addition, torque magnetometry experiments were carried out at the High Field Magnet Laboratory in Nijmegen in a ^{3}He refrigerator and at fields up to 30 T.

3.2 Resistivity and susceptibility

Resistivity data were acquired using a low-frequency (f = 16 Hz) resistance bridge LR 700 or a phase sensitive detection technique using a lock-in amplifier EG&G 7260 with a low excitation current ($I \leq 200$ μA). The resistance, R, was measured using a standard four-point method. The resistivity, ρ, is calculated using the relation $\rho = R\frac{A}{l}$, where A is the cross section of the sample and l is the distance between the voltage contacts. Low-noise pre-amplification of the magnetoresistance signal was achieved by mounting a low impedance transformer into the field compensated region of the dilution refrigerator [114].

The ac-susceptibility was measured with a mutual inductance transformer method using a home-built coil set. The coil set consist of a primary and two oppositely

wound secondary coils. Low frequency current is applied to the primary coil which generates a small driving magnetic field of 10^{-5} T. The induced voltage is measured by the secondary (pick-up) coils using a EG&G 7260 lock-in amplifier. The measured voltage is proportional to the ac-susceptibility signal.

3.3 Pressure cell

High-pressure magnetotransport measurements were carried out with help of a hybrid clamp cell. It is made of nonmagnetic and strong NiCrAl and CuBe alloys. The maximum pressure which this particular cell can achieve is 2.5 GPa. The inner and outer diameters are 6 mm and 25 mm respectively. The total length of the cell is 70 mm and varies slightly with pressure. The sample space is 4.7 mm in diameter and 8 mm long. A hand press LCP 20 was used to pressurize the cell via a piston. The sample is mounted on a plug that was placed in a Teflon cylinder with Daphne oil 7373 as a hydrostatic pressure transmitting medium. For the resistance measurements in a 4-point configuration, thin gold wires were attached to the flat sides of the crystals using silver paste. Sample mounting was done with help of Dr. T. Naka. The pressure calibration of the cell has been carried out by Dr. T.V. Bay by measuring the superconducting transition of a Sn sample via ac-susceptibility [115]. The pressure efficiency, the ratio between real and nominal pressure, of the cell after cooling to liquid helium temperatures was found to be 85 %. The pressures given throughout this thesis refer to the real pressure.

3.4 Cantilever magnetometry

The torque magnetometry technique is based on a thin cantilever. The deflection of the cantilever is measured using a capacitance method, where the torque, τ, is proportional to a change in capacitance, ΔC. The home-built magnetometer consists of a flexible and a fixed BeCu plate (size 5×5 mm^2) which form a parallel plate capacitor. A schematic of the cantilever magnetometer is shown in Fig. 3.1. The distance between the plates is about 100 μm. The torque that bends the flexible plate is linked directly to the magnetisation M of the measured material: $\vec{\tau} = \vec{M} \times \vec{B}$. The sample was glued on the top part of the flexible plate using GE varnish. The cantilever was mounted on the single-axis piezo-rotator ANRv51/RES (Attocube). The signal of

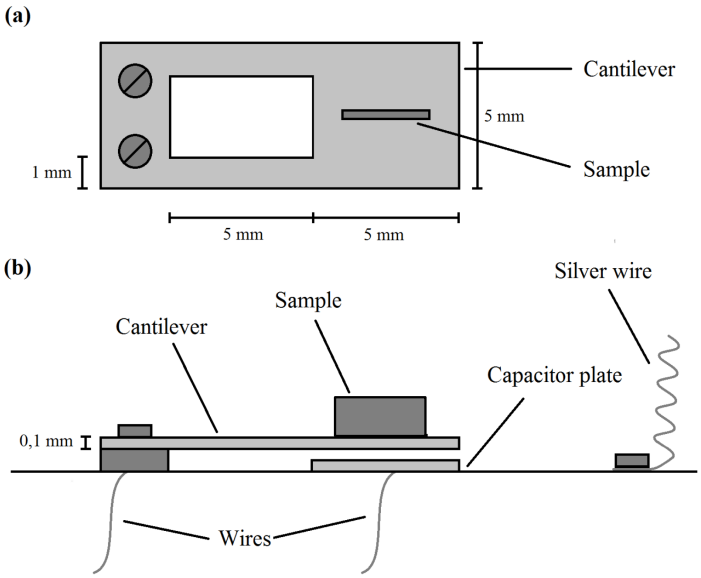

Figure 3.1: Schematics of the cantilever and torque magnetometry setup. (a) Top view: the sample is mounted on its side on the sample plate of the cantilever. (b) Side view: the capacitance is measured between the sample plate and the bottom plate. A silver wire is used for the thermalization of the cantilever. The picture is adapted from Ref. [116]

the empty cantilever was measured at T = 0.25 K and in applied magnetic fields up to 12 T. The measured torque was of the order of $\Delta C = 5 \times 10^{-5}$ pF, which is four orders of magnitude smaller than the torque obtained for the UCoGe samples. The empty cantilevers used in this work were kindly provided by Dr. A. McCollam (Radboud Universiteit Nijmegen).

3.5 Dilatometry

3.5.1 Thermal expansion

Dilatometry measurements have been performed employing a parallel-plate capacitance method. The capacitance for this case is given by a simple relation:

$$C = \frac{\epsilon A}{d} \tag{3.1}$$

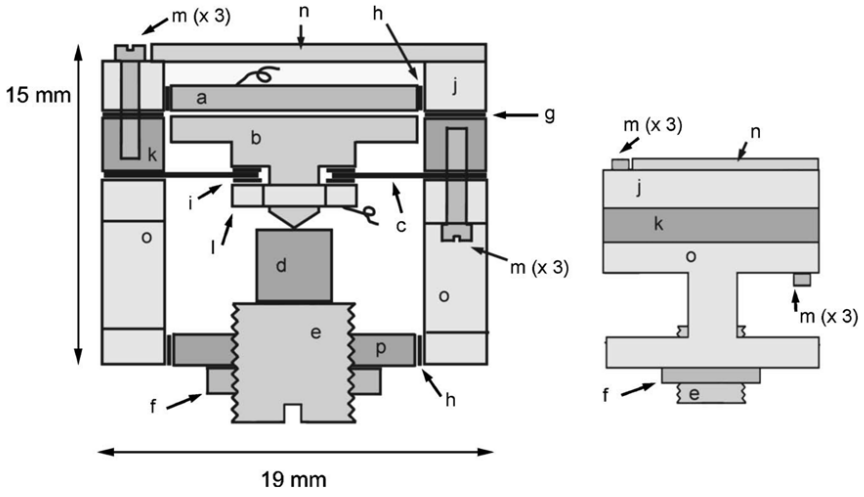

Figure 3.2: Schematics of the capacitive dilatometer taken from Ref. [117], where *a* – upper (fixed) capacitor plate, *b* – lower (movable) capacitor plate, *c* – BeCu spring, *d* – sample, *e* – sample platform, *f* – lock ring, *g* – copper shims, *h* – electrical isolation (Stycast 2850FT), *i* – electrical isolation (Kapton washers), *j* – upper guard ring, *k* – lower guard ring, *l* – nut, *m* – copper screws (6 in total), *n* – mounting plate, *o* – main body and *p* – lower fixation body.

where $\epsilon = \epsilon_0\epsilon_r$, $\epsilon_0 = 8.854 \times 10^{-12}$ F/m is the vacuum permittivity, ϵ_r is the dielectric constant of the medium between the plates, A is the area of the plates and d is the distance between them. A schematic drawing of the thermal expansion cell is shown in Fig. 3.2. By mounting a sample (*d*) in mechanical contact with the movable plate (*b*) it is possible to determine the length change of a sample as: $\Delta L = -\Delta d$. Here the BeCu flat spring (*c*) fixes the movable plate and allows the lower capacitance plate to move with respect to the cell body.

The capacitance of the dilatometer is measured with a three-terminal technique [118]. The measurements were performed with an Andeen-Hagerling capacitance bridge (AH 2500A or AH 2700A). The capacitance resolution of these bridges is 1×10^{-7} pF. The design of the cell is taken from Schmiedeshof *et al.* [117]. The cell is manufactured at the Technology Centre of the University of Amsterdam (TC UvA). The Schmiedeshof cell has a number of advantages. It is compact (less that 20 mm

in diameter) which allows for its rotation in the limited space in the magnet bore of the cryostat. The cell also has a small cell effect at low temperatures, which makes it a perfect instrument to measure length changes at low temperatures.

3.5.2 Calibration of the dilatometer

A room temperature calibration is needed to define the ϵA value which determines the functional dependence between the capacitor gap d and the measured capacitance C. For the calibration data presented in Fig. 3.3(b), we place the dilatometer on a flat surface, in air, at room temperature and attached to a protractor. Calibration has been done on a cylindrical Cu sample with a diameter and height of both 4 mm. The sample was made from the same oxygen free high conductivity Cu piece as the dilatometer. The dilatometer was inverted with respect to its normal orientation. The sample platform is then rotated (tightened) in small steps. After each step the angular position of the sample platform θ and the capacitance C are measured. The results plotted as d vs $1/C$ are shown in Fig. 3.3(b). The capacitance gap $d(\mu\text{m})$ is related to $\theta(deg)$ as d = 36/25 θ. The constant 36/25 comes from the fact that the sample platform has 4 threads per mm. The slope of the linear fit to the data determines $\epsilon A = 13.3 \pm 0.3 \times 10^{-16}$ Fm. The uncertainty in the determination of this value gives an accuracy of 5% on the absolute value of the experimental data. The influence of a small amount of He gas ($\epsilon_r \simeq 1.00006$) present between the capacitance plates during the experiment ($p \simeq 10^{-5}$ mbar) on the dielectric constant can be neglected.

An another important aspect is plane-parallelity of the capacitor plates. If the capacitor plates are not flat or not parallel, C is no longer proportional to $1/d$ and an additional term has to be added to Equation 3.1 [119]. If the lower plate is tilted with respect to the upper plate then the distance between the plates varies from d-a on one side to d+a on the other side. The capacitance is then determined as:

$$C = \frac{\epsilon A}{d}(1 + \frac{a^2}{4d^2}). \tag{3.2}$$

The correction to the capacitance depends quadratically on the misalignment. Significant corrections are only expected for a large misalignment of the plates. For example, if the misalignment a = 10 μm with d = 100 μm the correction will be $a^2/4d^2$ = 0.0025 or 0.25 %. For all data in this thesis we neglect this effect.

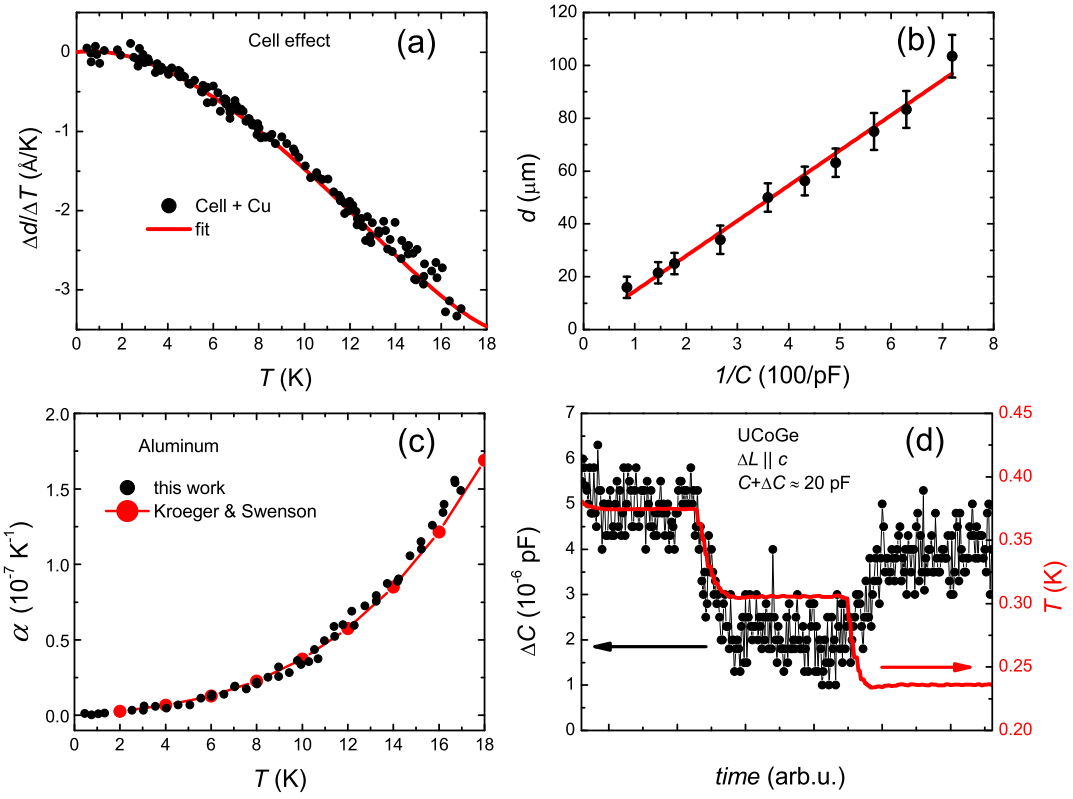

Figure 3.3: (a) Typical data showing $\Delta d/\Delta T$ for the dilatometer as a function of temperature measured on a copper sample (the cell effect). The solid line is a polynomial fit to the data $\frac{\Delta d}{\Delta T} = \sum_{i=1}^{5} B_i T^i$ (see text). (b) Room temperature calibration data of Equation 3.1: the capacitor gap, d, as a function of inverse capacitance, $1/C$, of the dilatometer. The solid line is a linear fit (the coefficient of determination $R^2 = 0.987$) to the calibration data, where the slope of the curve determines $\epsilon A = 13.3 \pm 0.3 \times 10^{-16}$ Fm. (c) The temperature dependence of the linear thermal expansion coefficient of aluminum (circles) compared with the literature values [120]. (d) Typical capacitance data (left axis, circles) and temperature (solid line, right axis) as a function of time during measurements of the α of UCoGe.

A low temperature calibration is needed to determine the cell effect. The cell effect is the thermal expansion of the dilatometer itself. It was measured on the same Cu sample as used for the room temperature calibration of ϵA. The linear thermal expansion coefficient is defined as $\alpha = L^{-1}\Delta L/\Delta T$, where L is the length of the sample. The linear thermal expansion coefficient of the sample is calculated from:

$$\alpha = -\frac{1}{L}\left(\frac{\Delta d}{\Delta T}\right)_{cell+sample} + \frac{1}{L}\left(\frac{\Delta d}{\Delta T}\right)_{cell+Cu} + \alpha_{Cu}. \tag{3.3}$$

Here, the first term corresponds to the length change of the cell with a sample mounted, or the measured signal, the second term is the cell effect and the last term is the thermal expansion of copper. The thermal expansion of copper is well known from the literature [120]. The cell effect was measured at low temperatures and is shown in Fig. 3.3(a). The data can be well described with a fifth order polynomial function:

$$\frac{\Delta d}{\Delta T} = \sum_{i=1}^{5} B_i T^i \tag{3.4}$$

where B_1 = 0.03666 Å/K^2, B_2 = -0.03078 Å/K^3, B_3 = 0.00201 Å/K^4, B_4 = -1.0376$\times 10^{-4}$ Å/K^5 and B_5 = 2.65796$\times 10^{-6}$ Å/K^6.

The cell effect is very small at temperatures below 2 K, which allowed us to determine the linear thermal coefficient of small samples with a good precision. α was measured using a step-heating method with a few variable parameters: the temperature step, the waiting time for stabilization after heating (cooling) and the number of (T, C) points over which to average the capacitance step. For the automation of the experiment a dedicated LabVIEW program has been written with a help of G. Hardeman (TC UvA). The working principle of this program is as follows. A user sets the temperatures, the waiting time for each step and the number of points for averaging. The temperature is controlled using the ORPX heater (in the Kelvinox and the Heliox for T $<$ 1.5 K) and the standard PID heater in the Heliox (for T $>$ 1.5 K). The ORPX heater was mounted next to the dilatometer. The cell effect and the expansion of the copper are subtracted from the signal. All the important parameters such as the capacitance, the temperature and the linear thermal expansion coefficient are displayed on the screen while running the measurements and saved to file.

To show how sensitive the dilatometer is we have measured the linear thermal expansion of the 4 mm long aluminium (Al) sample. The data are shown in

Fig. 3.3(c). Here we compare our data with the literature [120]. This demonstrates that our thermal expansion cell can resolve α with a precision of 1×10^{-8} K^{-1} at $T < 4$ K.

The step-heating (-cooling) method of measuring the linear thermal expansion coefficient is demonstrated in Fig. 3.3(d). In this graph we show the time dependence of the capacitance signal and the corresponding temperature measured for a UCoGe sample. The scatter in ΔC is $\pm\, 1 \times 10^{-6}$ pF, which is one order of magnitude higher that the resolution of the AH 2500A bridge. The smallest detectable step in the capacitance signal we can resolve is 2×10^{-6} pF on a 1 mm long UCoGe sample, at $T < 0.5$ K with $\Delta T = 0.07$ K and $C = 20$ pF. Using the relation $\Delta L = \frac{\epsilon A}{C^2}\Delta C$ we calculate the resolution of the dilatometer is $\Delta L = 0.033$ Å.

The Schmiedeshof dilatometer can show some glitches in the data, both in temperature and in the field dependent data [1]. These glitches manifest themselves as irreversible jumps in the capacitance. They are easy to detect because they are not reproducible and do not affect more than one or two data points. One can attribute these to stress relief processes in the copper, but they can also be caused by two materials (with different thermal expansions) sliding across each other (e.g. the copper sample platform and the sample). These glitches can cause non-trivial errors in measurements of ΔL. One can avoid this problem by plotting the capacitance and temperature as a function of time, and then removing erratic data points due to the glitches.

3.5.3 Magnetostriction cell effect

The magnetostriction is defined as the length change of a material in applied magnetic field, $\Delta L(B)$. The coefficient of magnetostriction is defined as $\lambda' = L^{-1}\Delta L/\Delta B$. In order to investigate the effect of an external magnetic field on the behaviour of the cell a 4-mm long copper sample was mounted and the magnetostriction measured. The results are presented in Fig. 3.4. The relative length change, $\Delta L/L$, depends on the magnitude of the applied field and the sweep rate. The measured expansion is smaller, when the field is constant. In Fig. 3.4(a) $\Delta L/L$ is shown as a function of time and B. The magnetic field was increased or decreased in steps of 0.5 T. This

[1] An appearance of glitches in the raw data is the downside of this particular design of the dilatometer. On the other hand, the Schmiedeshof dilatometer allows measuring the thermal expansion on the sample with non-plane-parallel surfaces.

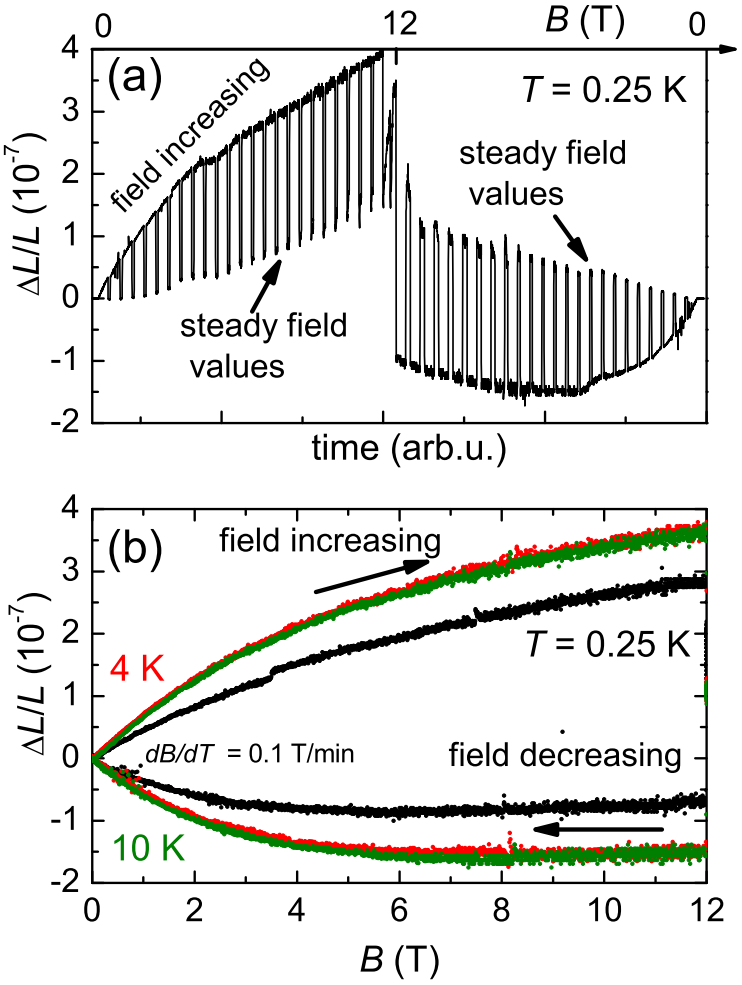

Figure 3.4: (a) The relative length change, $\Delta L/L$, of the dilatometer measured on a copper sample as a function of time at temperature T = 0.25 K. The magnetic field was applied in steps of 0.5 T after which the field was kept constant for 30 s. The top axis gives the magnitude of B. (b) $\Delta L/L$ as a function of the applied magnetic field at temperatures T = 0.25 K, 4 K and 10 K as indicated. The arrows shows increasing or decreasing magnetic field. B changes continuously. The dilatation direction is along the field direction, $\Delta L/L \parallel B$, for both figures.

increase or decrease was followed by a 30 s stabilization time at fixed B. During this short stabilization period the $\Delta L/L$ signal drops. The nature of such a behaviour of the dilatometer can be explained by eddy-currents. When the magnetic field is changed, eddy-currents are induced in the Be-Cu spring inside the thermal expansion cell. This can lead to an extra contribution to the measured capacitance signal due to a magnetic torque on the spring. The direction of the eddy-currents depends on the vector of the applied field, which results in different sign of $\Delta L/L$ for increasing and decreasing field. The increasing B gives a positive outcome (or expansion) in the magnetostriction of the cell itself, while the decreasing B results in shrinking. $\Delta L/L$ as a function of B measured with a continuous field sweeps (rate = 0.1 T/min) is shown in Fig. 3.4(b). The magnetostriction cell effect is at least two order of magnitude smaller than the measured magnetostriction signal of a ferromagnetic material, such as UCoGe, in the high field regime. The relative length change has a weak temperature dependence.

3.6 Rotators

In order to carry out field angular dependent measurements of for instance magnetoresistance or thermal expansion in an applied field, *in situ* rotation in the cryostat is required. Such a rotator must satisfy the following conditions. It should have a small size in order to fit in the magnet bore, be able to rotate a load of up to 40 g, be equipped with a high-precision angle read-out and have a low heat input. For this purpose, we have used the piezo-based rotators from Attocube. In this section the implementation of the rotators in the Heliox and Kelvinox is discussed.

3.6.1 Piezo-based rotators

The working principle of a motor with a piezo-element is based on moving an object under friction by impulsive force. It utilizes static friction and impulsive force caused by the rapid displacement of the piezo-actuator. The motion mechanism basically consists of three parts: the main body, the actuator and the internal weight. When the actuator executes rapid expansion or contraction, a strong inertial force is generated and the main body is moved against static friction. When the actuator executes slow retraction, the static friction may exceed the inertial force so that the

Table 3.1: Specification of the Attocube rotators

	ANRv51/RES	ANRv220/RES
footprint; height	10 x 20; 21 mm	27 x 12; 28.5 mm
weight	10 g	38 g
maximum dynamic torque around axis	0.2 Ncm	0.7 Ncm

main body keeps the position. Repeating these fast and slow actuator displacements carries out the motion [121].

We have used two different rotators: the ANRv50/RES and the ANRv220/RES. The specifications of both are shown in Table 3.1. Both rotators are made from a Be-Cu alloy. The ANRv50/RES has a small dynamic torque of 0.2 Ncm. This is enough to move a typical sample holder which has a mass of 10 g. The technical drawing of this rotator with a resistance sample holder mounted and a photograph are shown in Fig. 3.5. The ANRv220/RES has a dynamic torque of 0.7 Ncm. This rotator was factory adapted to fit our gear mechanism and enables rotation of the dilatometer with a mass of 40 g.

The controller ANC350 was used for operating the rotators. The rotation is produced by two main parameters: the amplitude of the voltage pulses V and the frequency of pulses f. In order to achieve a slow, low heat generation motion, typical values of V = 10 - 50 V and f = 10 - 60 Hz were applied.

3.6.2 Wiring

The wiring is important in two aspects. First, it has to deliver the driving voltage to power the rotator without significant losses. Low resistance wires are recommended by Attocube. A room temperature test of the ANRv51/RES showed that wires with $R > 10\ \Omega$ reduce the power available to drive the rotator significantly. Secondly, the heat load on the low temperature platform has to be kept low. For the Heliox it implies that during rotation the temperature at the sample should not exceed 6 K, while for the Kelvinox this is 1 K.

The Kelvinox is equipped with two low-ohmic coaxial cables with $R = 3\ \Omega$ and these were used to drive the rotator. In the Heliox new wires were installed. Copper wires were fitted between the top of the insert (room temperature) and the 4.2 K flange. For a low heat input at the sample platform, superconducting wires (NbTi) were used in the ^{3}He section in the vacuum can. In fact we had to use several

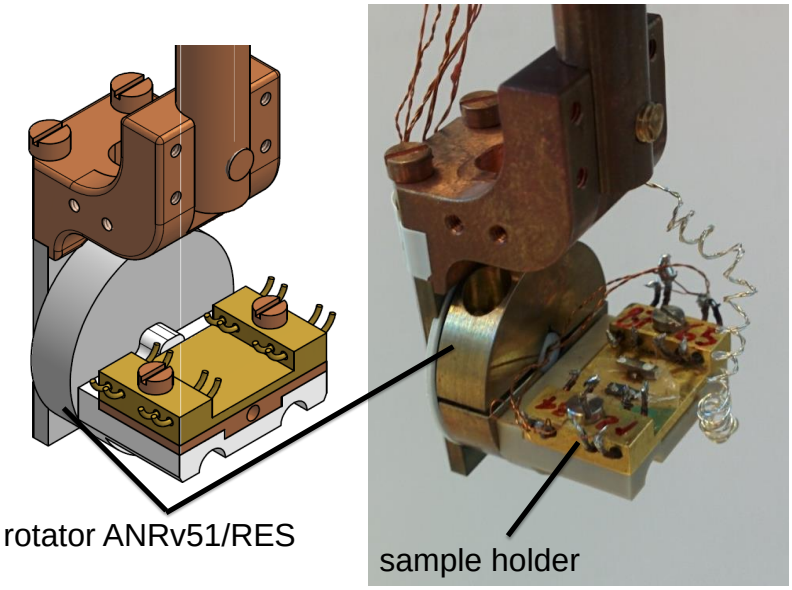

Figure 3.5: Technical drawings (left side, courtesy of R. Manuputty, TC UvA) and a photograph (right side) of the piezoelectric rotator ANRv51/RES with a resistance sample holder as indicated.

superconducting wires in parallel in order to reduce the normal state resistance to below 6 Ω. When applying the voltage across the wiring system at low temperatures we found that they become resistive quite rapidly. Therefore, a reduced resistance was obtained by connecting six wires in parallel. Introducing the new wires in the Heliox has some impact. The working cycle, *i.e.* the time window for keeping the lowest temperature without recondensation, was reduced from 48 hours to 6 hours.

3.6.3 Calibration of the angle reader

Precise knowledge of the angle between the axis of the crystal and the direction of the magnetic field is required. The Attocube rotators are equipped with an angle reader – the positioner or RES. The positioner is a resistive sensor. The resistance of the sensor is measured using a four-point technique and translated to degrees. The calibration of the positioner has been made at room temperature by Attocube. Therefore, an additional low temperature calibration required for our application. A miniature Hall probe (Arepoc company) was used to determine the angle. Its Hall effect is linear at low magnetic fields. When a current, I, is applied to the sensor it

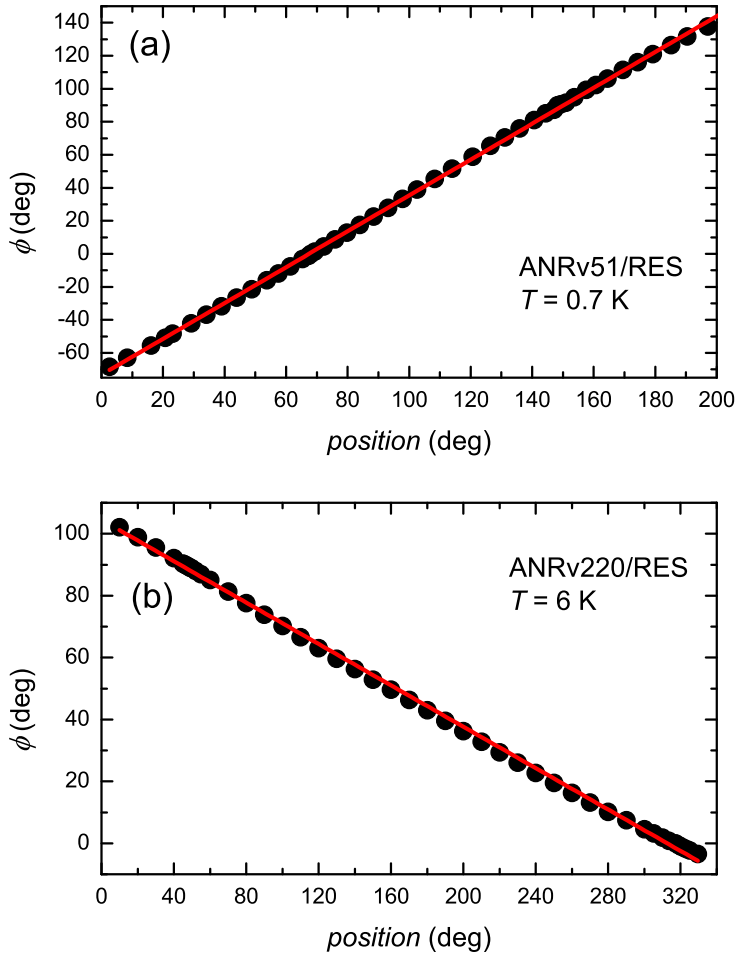

Figure 3.6: The low temperature calibration of the positioner of the Attocube rotators made with help of the miniature Hall probe at B = 1 T. (a) The angle between the applied magnetic field and the surface of the Hall probe, ϕ, as a function of the positioner of the ANRv51/RES (circles) measured at T = 0.7 K. The solid line represents a linear fit (R^2 = 0.9987) to the data: $\phi = 1.09 \times position(RES) - 73.30°$. (b) The angle between the applied magnetic field and the surface of the Hall probe, ϕ, mounted on the main body of the dilatometer as a function of the positioner of the ANRv220/RES (circles) measured at T = 6 K. The dilatometer was attached with help of a gear mechanism to the rotator with gear ratio 1:3. The solid line represents a linear fit (R^2 = 0.9988) to the data: $\phi = 104.50° - 0.33 \times position(RES)$. The error bars are within the size of the points.

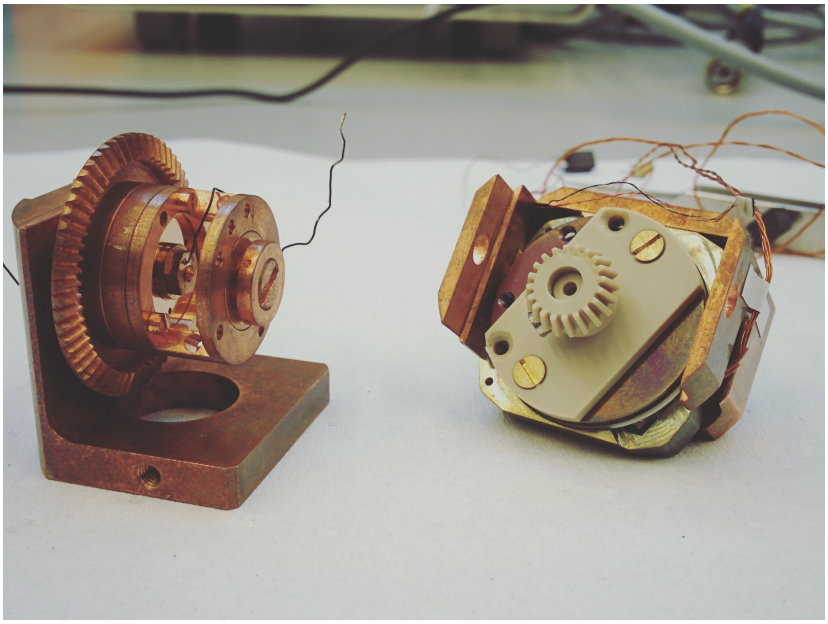

Figure 3.7: A photograph of the smaller cogwheel, the rotator ANRv220/RES and the support plate (right) and the large cogwheel of the gear mechanism and the dilatometer (left).

results in a Hall voltage:

$$V_{Hall} = \frac{I}{ne} B cos(\phi), \tag{3.5}$$

where ϕ is the angle between the surface of the sensor and the applied magnetic field, n is the charge carrier density, e is the electron charge. By measuring V_{Hall} at B = 1 T during rotation it was possible to calibrate the positioners.

The Hall probe was glued on the sample holder using GE varnish. The calibration of the ANRv51/RES was performed in the Heliox at T = 0.7 K. For each data point the value of the Attocube RES, the position, was recorded together with the Hall voltage. The resulting angle ϕ was calculated using Equation 3.5. In Fig. 3.6(a) we show the calibration data with the angle ϕ on the vertical axis and the angle of the positioner on the horizontal axis. The solid line represents a linear fit to the points: $\phi = 1.09 \times position(RES) - 73.30°$.

3.6.4 Rotation of the dilatometer

Rotation of the dilatometer inside the cryostat was achieved by introducing a dedicated gear mechanism. Due to the limited space – the diameter of the vacuum can

of the Heliox being only 39.6 mm – we decided to use a gear mechanism to transfer the rotation axis from vertical to horizontal as shown in Fig. 3.8. In this drawing the ANRv220/RES (item 5) is fixed with screws to the support plate (green in Fig. 3.8). The vertical axis of the piezoelectric rotator is translated to horizontal using set of gears comprising a smaller ceramic cogwheel (item 4) and a larger copper cogwheel (item 3). The gear ratio is 1:3, which improves threefold the angular resolution of the rotation of the dilatometer. The angular resolution was shown to be 0.05°. The dilatometer (item 1) is attached to the large cogwheel. A special ball bearing mechanism (item 2) enables rotation at very low temperatures with reduced friction. Special care in the design of the rotation mechanism was taken as regards the position of the sample, so as to ensure that the latter remains fixed in the center position of the superconducting magnet. In this configuration the applied magnetic field is always perpendicular to the dilatation direction of the sample. A photograph of the disassembled parts is shown in Fig. 3.7.

The rotational calibration of the complete Attocube ANRv220/RES + gears + dilatometer set-up has been made in the Heliox. To do this, the Hall probe was mounted on the main body of the dilatometer. The temperature during the rotation was around 6 K. In Fig. 3.6(b) we show the calibration data, where the angle ϕ is plotted on the vertical axis and the angle of the positioner on the horizontal axis . The solid line represents a linear fit to the points: $\phi = 104.50° - 0.33 \times position(RES)$.

3.7 Sample preparation

All the single crystalline samples used for this thesis were prepared at the University of Amsterdam by Dr. Y.K. Huang, except for one crystal of UCoGe (RRR = 40) which was grown by Dr. D. Aoki at CEA, Grenoble. HoPdBi single crystals were prepared using the flux technique and $Sr_xBi_2Se_3$ crystals by the Bridgman method. Details of the sample preparation processes for each material are given in the experimental section of each chapter, except for the UCoGe crystals whose preparation is described below.

3.7.1 UCoGe

The preparation of high quality single crystals of UCoGe is a complex procedure and involves three major steps. First, a polycrystal has to be prepared. Secondly, the

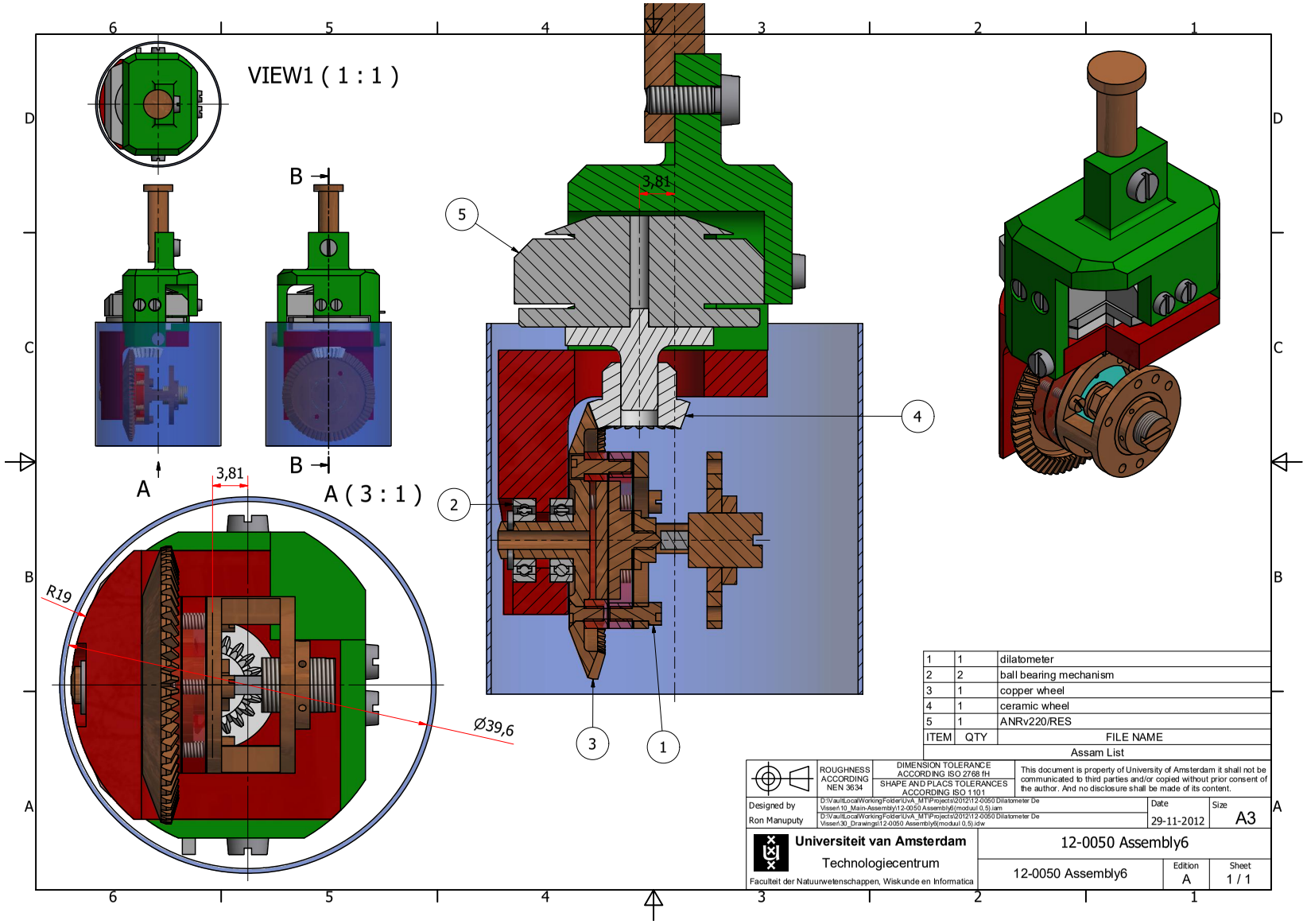

Figure 3.8: Drawings of the rotation mechanism with ANRv220/RES and dilatometer.

Table 3.2: Polycrystalline sample characterisation

batch	label	U used	RRR	annealing	T_C, T_{sc}
Uranium	U	Goodfellow	5		
	U	New Brunswick	11		
	U	CEA France	18		
	U	Ames	22		
UCoGe 281112	UCoGe	Goodfellow	12 - 17	10 days, T = 950°C	2.9 K, 0.7 K
	$U_{1.02}$CoGe	Goodfellow	17 - 20	10 days, T = 950°C	3.0 K, 0.7 K
	$U_{1.02}Co_{1.02}$Ge	Goodfellow	25	10 days, T = 950°C	3.1 K, 0.75 K
UCoGe 050413	$U_{1.02}Co_{1.02}$Ge#1	New Brunswick	3	10 days, T = 950°C	3.1 K, not SC
	$U_{1.02}Co_{1.02}$Ge#2	CEA France	5	10 days, T = 950°C	2.9 K, 0.3 K
	$U_{1.02}Co_{1.02}$Ge#3	Ames	5	10 days, T = 950°C	2.7 K, 0.4 K
UCoGe 11062013	UCoGe	CEA France	41	10 days, T = 950°C	3.0 K, 0.75 K
	$U_{1.02}$CoGe	CEA France	20 - 22	10 days, T = 950°C	2.0 K, 0.68 K
	$U_{1.02}Co_{1.02}$Ge	CEA France	7	10 days, T = 950°C	1.4 K, 0.4 K
UCoGe 20130416		Ames	10	10 days, T = 950°C	2.8 K, –

single crystal is grown by the Czochralski technique. Thirdly, a long annealing process finalizes the procedure. Typically it might take more than a month to prepare and characterize a crystal.

The polycrystalline samples were prepared in a home built mono-arc furnace. The melting process takes place in a high purity argon atmosphere of 0.5 bar. The high purity of the starting materials is 3N for U, 4N for Co and 5N for Ge. Pure U metal was obtained from different companies/laboratories: Goodfellow, New Brunswick, CEA France and Ames Laboratory. In order to test the purity of the uranium batches small polycrystalline buttons with a typical mass of 1 g were prepared. Bars were cut by spark erosion from the (unannealed) buttons and the residual resistance ratio, RRR = R(300 K)/R(4 K), was measured. The resulting RRR values are reported in Table 3.2 and range from 5 (Goodfellow) to 22 (Ames).

For this thesis project we have prepared several batches of polycrystalline UCoGe, using U from different sources and with a small variation in stoichiometry. Some characteristics of the polycrystalline batches are presented in Table 3.2. The highest RRR = 41 was determined for crystal with nominal composition UCoGe grown using U provided by CEA France. All polycrystalline samples were annealed under high vacuum in quartz ampoules for 10 days at T = 950°C. The single crystals are

Table 3.3: Single crystalline sample characterisation

batch	label	U used	RRR	annealing	T_C, T_{sc}
UCoGe sc 2013	ann 1	Ames	6.5	14 days, T = 880°C	1.5 K, 0.55 K
	ann 2 TE			21 days, T = 880°C	
	ann 2 bar		5 - 8	21 days, T = 880°C	1.5 K, 0.45 K
UCoGe sc 2014	ann 1	CEA France		21 days, T = 880°C	
	ann 2		6 - 7	1 day, T = 1250°C	–, 0.5 K
				and 14 days, T = 880°C	
	ann 3		6.5	21 days, T = 880°C	–, 0.37 K
UCoGe sc 1214	unannealed	Ames	8		–, 0.4 K
	ann 1		7.5	14 days, T = 880°C	1.5 K, 0.58 K
	ann 2		7	7 days, T = 900°C	
	ann 3		4.6	7 days, T = 900°C	–, 0.49 K
	ann 4		3.5	7 days, T = 900°C	–, 0.40 K
	ann 5		3.5	21 days, T = 900°C	–, 0.42 K
UCoGe sc 2015	unannealed	Ames	3		–, not SC
	ann 1		2	21 days, T = 900°C	–, 0.42 K
	ann 1 TE			21 days, T = 900°C	

grown using the Czochralski method in a tri-arc furnace from polycrystalline samples with a mass of more than 10 g. The single crystallinity is checked using X-ray backscattering Laue diffraction. The same technique is afterwards used to orient the single crystalline samples. Different sample shapes are generated using a spark erosion machine, whereby bars and cube-shaped samples are cut from the boule by use of a conducting (Cu) wire immersed in oil. The surfaces of the samples are polished afterwards to remove the surface layer damaged by the spark cutting process.

The last and very important step in the sample preparation process is an annealing procedure. The single crystalline samples are wrapped in Ta foil and annealed in evacuated quartz ampoules ($p \simeq 10^{-7}$ mbar) or in a long quartz tube that is evacuated continuously by a turbo-pump for a period ranging from 7 to 21 days. A list of prepared single crystals, their annealing procedure and RRR values is reported in Table 3.3. In the framework of this PhD project, we did not manage to prepare single crystals of UCoGe with RRR greater that eight. In some cases (sc 1214 and sc 2015) annealing did not improve the RRR and the ampoules and Ta foil had a yellow trace after annealing. The yellow trace most probably is due to uranium oxide. Therefore,

for part of the experiments high quality single crystals, prepared earlier by Dr. Y.K. Huang and Dr. N.T. Huy (RRR = 30), and by Dr. D. Aoki (RRR = 40), were used.

Chapter 4

Superconducting and ferromagnetic phase diagram of UCoGe probed by thermal expansion

We report thermal expansion measurements on a single crystal of the superconducting ferromagnet UCoGe for magnetic fields applied along the main orthorhombic axes. The thermal expansion cell was mounted on a piezo-electric rotator in order to fine-tune the magnetic field angle. The superconducting and magnetic phase diagram has been determined. With our bulk technique we confirm the *S*-shape of the upper-critical field, B_{c2}, for $B \parallel b$ and the enhancement of superconductivity above 6 T. At the same time the Curie point shifts towards lower temperatures on increasing the field along the *b*-axis. This lends further support to theoretical proposals of spin-fluctuation mediated enhancement of superconductivity for $B \parallel b$.

This chapter has been accepted for publication in Phys. Rev. B.

4.1 Introduction

The quest for superconducting ferromagnets (SCFMs) goes back to the pioneering work of Ginzburg [82]. Later, in the 1970s, it was predicted, on theoretical grounds, that weak itinerant ferromagnets could exhibit p-wave, equal-spin-pairing superconductivity [24]. Here, the superconducting state is mediated by the exchange of longitudinal spin fluctuations, rather than by phonons as in the standard Bardeen, Cooper, Schrieffer (BCS) scenario. The experimental discovery of superconductivity in the itinerant ferromagnets UGe_2 (under pressure, Ref. [11]), URhGe [12] and UCoGe [22], opened up the opportunity to investigate the coexistence of superconductivity and ferromagnetism and their interplay in detail. In SCFMs the superconducting transition temperature T_{sc} is smaller than the Curie temperature T_C. The uranium $5f$-electrons are responsible for both ferromagnetic order and superconductivity. In the past decade ample evidence has been provided that spin-fluctuations in the proximity to a magnetic quantum critical point provide the attractive pairing interaction for odd-parity superconductivity (for recent reviews see Refs. [122, 123]). Although these SCFMs share common features, they are also quite distinct, notably as regards the phase diagrams in the magnetic-field $-$ temperature and the pressure $-$ temperature plane.

UCoGe crystallizes in the orthorhombic TiNiSi structure with space group P_{nma} [124]. Superconductivity at $T_{sc} = 0.6$ K and itinerant ferromagnetism at $T_C = 3.0$ K was first observed for polycrystalline samples [22]. The coexistence of ferromagnetism and superconductivity on the microscopic scale was demonstrated by muon spin rotation and relaxation (μSR) [84] and ^{59}Co nuclear quadrupole resonance (NQR) [85] experiments. Magnetization measurements on single-crystals showed that UCoGe is an uniaxial ferromagnet with a spontaneous magnetic moment, $m_0 = 0.07\ \mu_B$ per U-atom, that points along the c-axis [125]. Superconductivity shows a strongly anisotropic response to a magnetic field. For B parallel to the easy-magnetization axis (c-axis) superconductivity is suppressed in 0.5 T ($T \to 0$). On the other hand, for B perpendicular to the easy-magnetization axis, the upper-critical field, $B_{c2}(0)$, attains extremely large values and largely exceeds the Pauli limit for spin-singlet superconductivity [125, 87]. Moreover, $B_{c2}(T)$ measured for $B \parallel b$-axis [87] shows a striking S-shape which signals enhanced superconductivity in fields exceeding 6 T. The pronounced anisotropy of B_{c2} is arguably coupled to spin-fluctuation mediated pairing: for $B \parallel c$ the ferromagnetic fluctuations are sup-

pressed and superconductivity vanishes, while for $B \perp c$ spin fluctuations are robust and superconductivity persists up to high fields. Solid experimental evidence on the microscopic level for this scenario has been provided by ^{59}Co nuclear magnetic resonance (NMR) [126, 86] and inelastic neutron scattering [127] experiments. The superconducting phase diagram was qualitatively explained by a microscopic theory employing the coupling between the electrons by means of magnetization fluctuations in ferromagnetic metals [90]. A related approach was based on the Eliashberg theory by taking into account the Dzyaloshinskii-Moriya interaction arising from the zigzag chain crystal structure [88]. Here the S-shaped B_{c2}-curve is qualitatively explained as a result of the enhancement of the spin fluctuations due to the decrease of the Curie temperature when the field $B \parallel b$ is increased.

In this chapter we report the ferromagnetic and superconducting phase diagram in the $B - T$ plane of UCoGe obtained by thermal expansion measurements in fixed magnetic fields applied along the a-, b- and c-axes. Hitherto, the phase diagram was mainly studied using transport experiments [87]. Its determination by thermal expansion has the advantage that it involves a thermodynamic, bulk probe. Moreover, since the phase diagram depends sensitively on the alignment of the field with respect to the a- or b-axes [87], we mounted our thermal expansion cell on a piezoelectric rotator to enable tuning of the field-angle, as described in Chapter 3. We observe that the Curie point for $B \parallel b$ shifts gradually to lower temperatures and we present bulk-sensitive evidence for the S-shaped B_{c2}-curve for the same field orientation. Our results lend further support to the theoretical proposal of spin-fluctuation mediated enhancement of superconductivity in a magnetic field ($B \parallel b$).

4.2 Experimental

Single crystals of UCoGe were prepared in a tri-arc furnace (crystal 1) and in a tetra-arc furnace (crystal 2) using the Czochralski technique. Crystal 1, with residual resistance ratio RRR = 30, was cut from the grown crystal boule by means of spark erosion so as to give a bar shape with dimensions $a \times b \times c = 1.0 \times 5.0 \times 1.1$ mm^3. Sample 2 has RRR = 40 and was cut into a rectangular parallelepiped with dimensions $a \times b \times c = 1.4 \times 1.1 \times 1.0$ mm^3. Here RRR is defined as R(300K)/R(0K), where R(0K) is obtained by extrapolating the normal state resistance $R_n(T)$ to 0 K. The uncertainty in the alignment of the main crystallographic axes with the spark

cut planes is typically 2°. Additional information about the crystal growth, annealing procedure and characterization can be found in Refs. [128, 129].

The coefficient of linear thermal expansion, $\alpha = L^{-1}(dL/dT)$, with L the sample length, was measured using a three-terminal parallel-plate capacitance method. The home-built sensitive dilatometer (see Chapter 3) was based on the design reported in Ref. [117]. The sensitivity of the thermal expansion cell amounts to 0.03 Å. The dilatometer was used in two configurations: longitudinal, *i.e.* with the field along the dilatation direction $B \parallel \Delta L$, and transversal with $B \perp \Delta L$. In order to tune the magnetic field-angle with respect to the crystal axes in the transverse configuration, we have implemented an *in situ* rotation mechanism described in Chapter 3. The magnetic field is always perpendicular to the fixed dilatation direction when the cell is rotated. The standard field-angle reader of the rotator, the positioner, was calibrated at low temperatures using a miniature Hall-probe (Arepoc company) mounted on the main body of the cell and the angular resolution was shown to be 0.05°. We remark that since we can rotate over one axis only, a possible remaining absolute misorientation of $\sim 2°$ due to orienting and cutting the crystal cannot be avoided. The dilatometer and rotator were attached to the cold plate of a Helium-3 refrigerator for temperatures in the range $T = 0.24 - 10$ K (Heliox, Oxford Instruments) and magnetic fields up to 14 T, and to the cold finger of a dilution refrigerator (Kelvinox, Oxford Instruments) for $T = 0.03 - 1$ K and B up to 17 T. An additional heater and thermometer were mounted, thermally anchored to the thermal expansion cell, for the step-wise heating method to measure $\alpha(T)$ described in Chapter 3.

4.3 Results

4.3.1 Thermal expansion in zero field

Fig. 4.1 shows the thermal expansion coefficient, $\alpha_i(T)$, where i refers to the crystal axis a, b or c, of UCoGe crystal 1 (upper panel) and crystal 2 (lower panel), measured in the temperature range 0.05 - 6.0 K. The data for α_b in the upper panel are taken from Ref. [130], since the sample length of crystal 1 along the b-axis (5 mm) is too large to fit in the improved dilatometer developed in this thesis. The data were measured on a different crystal with RRR = 30 prepared from the same batch and using the previous dilatometer which possessed a large cell effect at low temperatures [94].

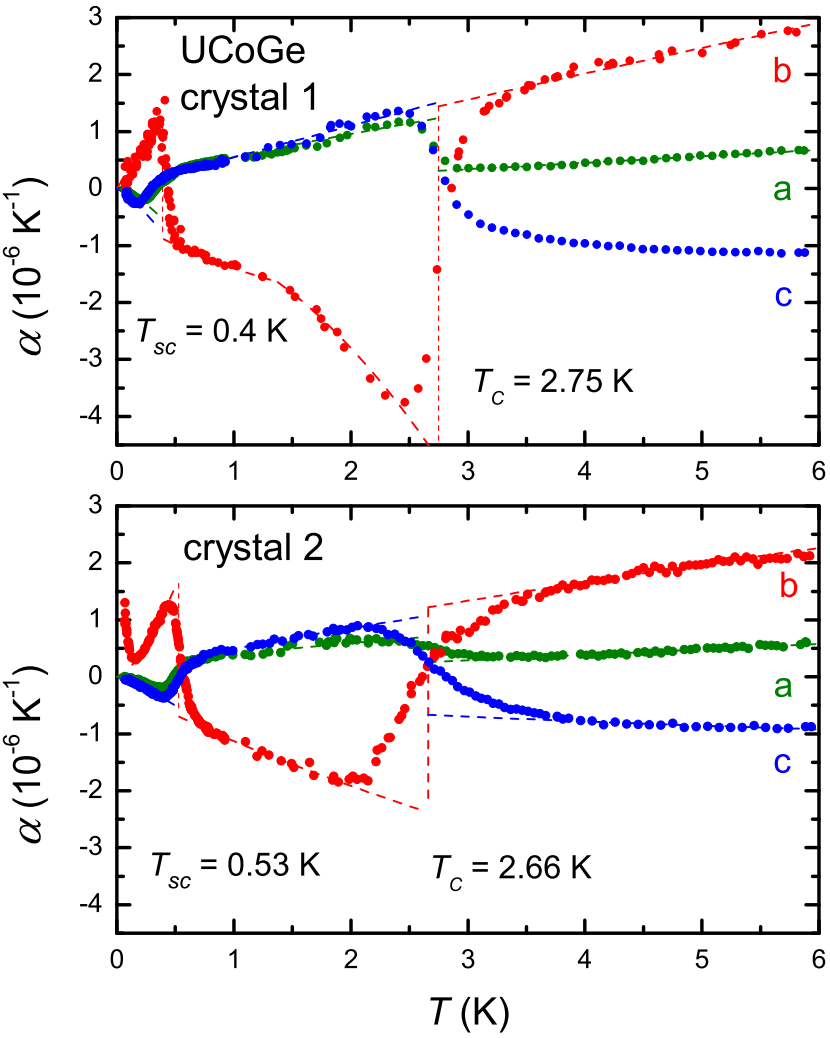

Figure 4.1: Temperature variation of the coefficient of linear thermal expansion of UCoGe along the orthorhombic *a*-, *b*- and *c*-axes, as indicated, for crystal 1 (top panel, RRR = 30) and crystal 2 (bottom panel, RRR = 40). The data for α_b in the top panel are taken from Ref [130]. The dashed lines indicate idealized, stepped phase transitions based on an equal-length construction (see text).

Overall $\alpha_i(T)$ of both crystals is very similar and in good agreement with the data reported in Ref. [130], forming a sound basis for the detailed angular dependent studies presented in the following. The thermal expansion coefficient is strongly anisotropic in the paramagnetic state. Below T_C, $\alpha_a(T)$ and $\alpha_c(T)$ behave similarly, while a strongly pronounced and opposite variation is found for $\alpha_b(T)$. The steps in $\alpha_i(T)$ at T_C and T_{sc} are relatively broad. For the ferromagnetic transition they have a positive sign (when cooling) along the *a*- and *c*-axes, and a negative sign along the *b*-axis. At the superconducting phase transition the signs are reversed. The dashed lines in Fig. 4.1 represent idealized transitions, based on an equal-length construction, with T_{sc} = 0.40 K and T_C = 2.75 K for crystal 1 and T_{sc} = 0.53 K and T_C = 2.66 K for crystal 2. The construction implies an overall equal-length change is imposed for the broadened and idealized contributions when integrating $\alpha_i(T)$ with respect to the background.

The different values of both T_{sc} and T_C for the two crystals demonstrate the intimate interplay between ferromagnetism and superconductivity in UCoGe. For the crystal with lower T_C, the superconducting transition temperature is slightly higher, which is in-line with the enhancement of superconductivity when the magnetic quantum critical point is approached [131]. We remark that the data for crystal 2 show a pronounced upturn in α_b at very low temperatures ($T < 0.15$ K), measured using the improved dilatometer. This anomalous behavior is only observed for α_b, and not for α_a and α_c. Its origin is not understood as will be discussed in section 4.4.3. In the following sections we present the thermal expansion data recorded for the magnetic field in the longitudinal and transverse geometry for crystal 2.

4.3.2 Longitudinal thermal expansion in magnetic field

In Fig. 4.2 we present the longitudinal thermal expansion of crystal 2 around the Curie point in fields up to 12 T ($B \parallel \Delta L_i$). In this configuration the thermal expansion cell is directly attached to the cold plate of the Heliox or cold finger of the Kelvinox, *i.e.* without rotator, thus tuning of the field-angle is not possible. The response to the magnetic field is different for each direction. For $B \parallel \Delta L_c$ (lowest panel), the ferromagnetic phase transition smears out rapidly. In 0.75 T $\alpha_c(T)$ is quasi temperature independent and close to zero. This is expected since the field is parallel to the ordered moment m_0 and the phase transition becomes a cross-over phenomenon. For the other two directions $B \perp m_0$, and thus the Curie point remains clearly visible in

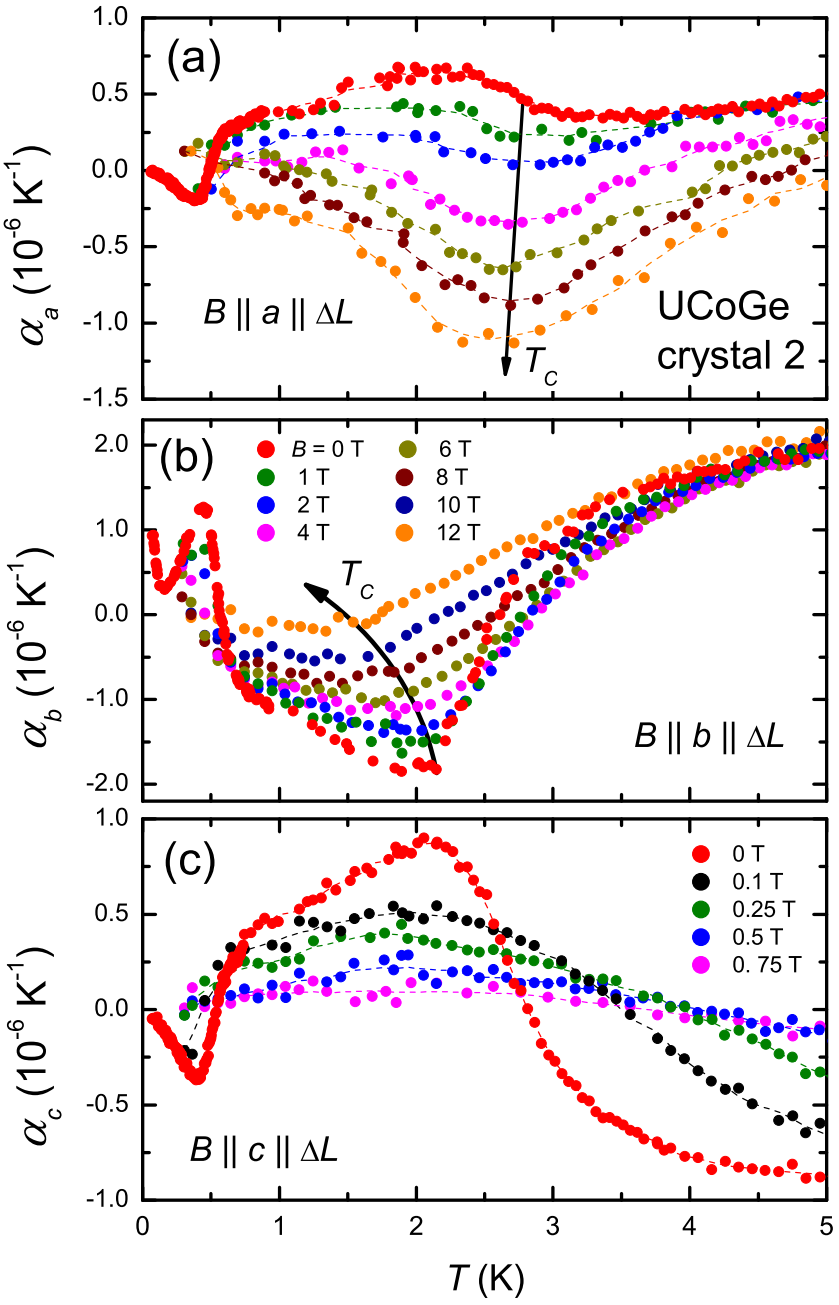

Figure 4.2: Coefficient of linear thermal expansion α_i, where i is a, b or c, of UCoGe crystal 2 in longitudinal magnetic fields $B \parallel a, b, c$ as indicated (the colour configuration for the top two panels is identical). Arrows indicate the field variation of T_C for $B \parallel a$ and $B \parallel b$.

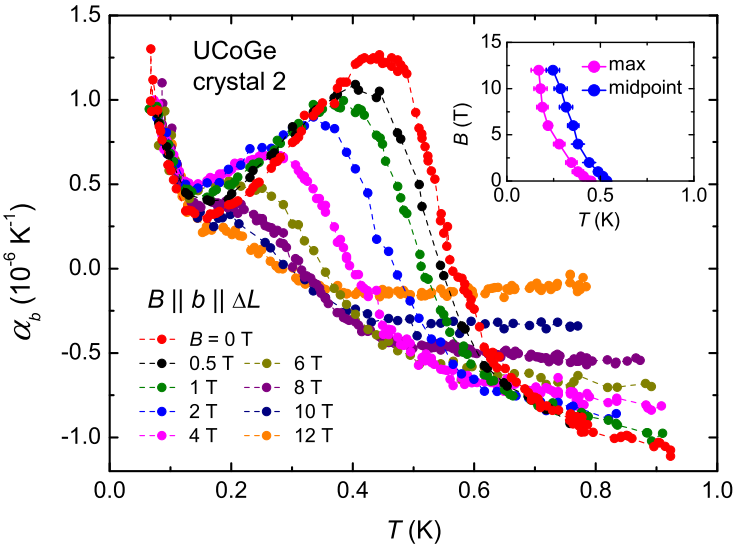

Figure 4.3: Coefficient of linear thermal expansion α_b of UCoGe crystal 2 in magnetic fields $B \parallel \Delta L_b$ up to 12 T. Inset: B-T phase diagram. Here T_{sc} is obtained by tracking the maximum in $\alpha_b(T)$ (magenta points) and by the midpoints of the transition (blue points).

the data. In the case of $B \parallel \Delta L_a$ (top-most panel), the magnetic contribution to α_a changes from positive to negative between 2 T and 4 T. In higher fields the magnetic component grows further, while the transitions broadens. The Curie temperature, which we identify by the minimum in $\alpha_a(T)$ at higher fields, is only weakly field dependent. For $B \parallel b \parallel \Delta L$ the magnetic contribution becomes weaker as the field grows, and T_C shifts towards lower temperatures. Comparing the field data for crystal 2 with those reported in Ref. [130] we find a good agreement for $B \parallel \Delta L_c$. For the other two directions the literature data show a more pronounced magnetic contribution in the field. This we attribute to the more developed ferromagnetic phase in the crystal measured in Ref. [130] (just like for crystal 1 in zero-field, as can be seen in Fig. 4.1). The longitudinal thermal expansion around the superconducting transition was measured in field only for α_b and is shown in Fig. 4.3. The superconducting transition observed at $T_{sc} = 0.53$ K in zero field shifts to lower temperatures with increasing field and remains clearly visible up to 12 T. The data in also show the upturn in $\alpha_b(T)$ below 0.15 K persists all data, up to and including the highest field used of 12 T.

4.3.3 Transverse thermal expansion in magnetic field

The upper-critical field, B_{c2}, of UCoGe is strongly anisotropic [125]. For $B \parallel c$ $B_{c2}(0) = 0.5$ T ($T \to 0$), but when the field is precisely aligned along the a- or b-axes, $B_{c2}(0)$ attains extremely large values with 16 T for $B \parallel b$ and close to 25 T for $B \parallel a$ [87]. A field-tilt of a few degrees away from the a- or b-axes results in a dramatic reduction of $B_{c2}(0)$. In order to fine-tune the field angle, the dilatometer was mounted on the rotator and the transverse thermal expansion was measured. The suppression of the superconducting state in the case $B \parallel c$ was measured for $B \parallel c \perp \Delta L_a$. The data are shown in Fig. 4.4(a). The superconducting transition temperature is gradually reduced with increasing field, and superconductivity is no longer observable at $B = 0.5$ T. The suppression of the superconducting state for $B \parallel a(b)$ was measured for $B \parallel a(b) \perp \Delta L_c$. To achieve an optimal alignment of the field along the a- and b-axes we have used the following strategy. $\alpha_c(T)$ around the superconducting transition was measured in a field of 1 T, then the dilatometer was rotated over typically 0.5° and $\alpha_c(T)$ was measured again. After obtaining several data sets in this way we selected the optimal orientation $B \parallel a(b)$ as the one in which $\alpha_c(T)$ shows the highest T_{sc}. The $B \parallel a$ and $B \parallel b$ data recorded for these optimised field orientations are presented in Fig. 4.4(b) and (c). For $B \parallel a$ the superconducting transition broadens rapidly and we can follow it only to 4 T. For $B \parallel b$ we find a very different behavior. The superconducting transition - as seen in the thermal expansion - firstly reduces with increasing $B \parallel b$, but this reduction then billows out and there are even indications that T_{sc} edges back up for $B \parallel b$ = 8 and 10 T before sinking again for B = 12 T. We do note that for larger fields, the noise level becomes higher than the idealized step in the linear thermal expansion coefficient at T_{sc}. Nevertheless, the step-like feature is still clearly present in the raw data for the filed as high as 10 T.

In Fig. 4.5 we show the resulting $B - T$ phase diagram obtained by tracking T_{sc} via three methods: the onset of the superconducting transition, the step in the idealized transition and the temperature of the local minimum in $\alpha_c(T)$. It is clear from Fig. 4.5 that the upper-critical field for $B \parallel b$ displays an S-shape curve with enhancement of B_{c2} for fields above 6 T.

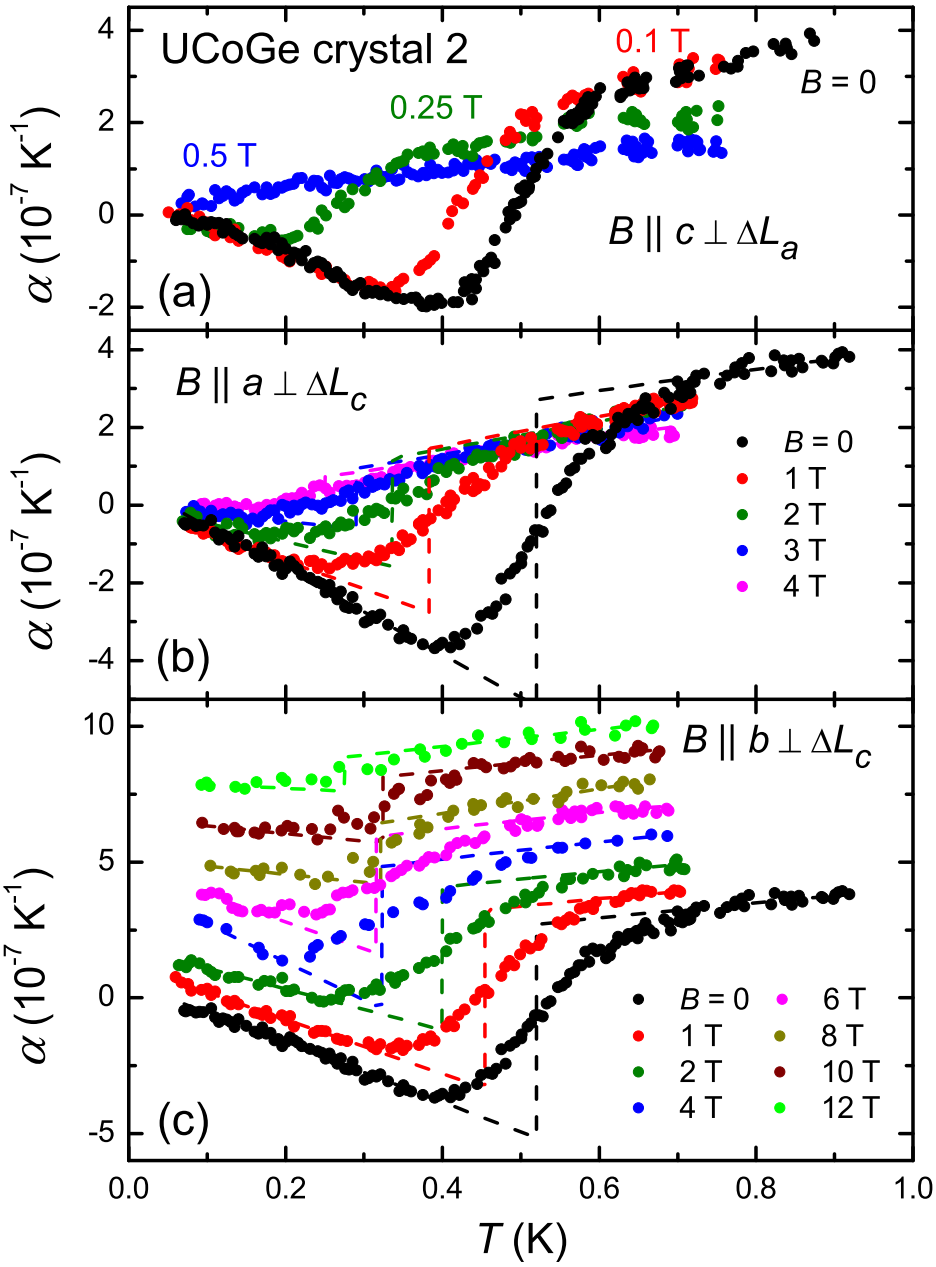

Figure 4.4: Coefficient of linear thermal expansion of UCoGe crystal 2 in transverse magnetic fields. Panel (a): For ΔL_a and $B \parallel c$ (up to 0.5 T as indicated). Panel (b): For ΔL_c and $B \parallel a$ (up to 4 T). Panel (c): For ΔL_c and $B \parallel b$ (up to 12 T). In panel (c) the curves in field are shifted upwards for clarity. The dashed lines indicate idealized step-like transitions.

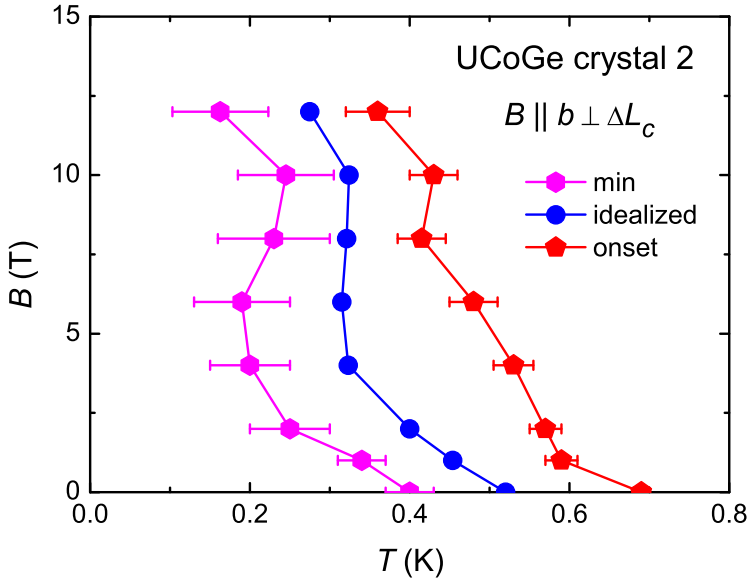

Figure 4.5: B-T phase diagram. T_{sc} obtained from transverse configuration $B \parallel b \perp \Delta L_c$ by tracking the onset in $\alpha(T)$ data (red points), idealized transition (blue points) and minimum of the curve (magenta points).

4.4 Analysis and discussion

4.4.1 Uniaxial and hydrostatic pressure dependence of critical temperatures

The uniaxial and hydrostatic pressure dependence of T_C and T_{sc} of crystal 2 have been determined with help of the Ehrenfest relation. For a second-order phase transition $\frac{\partial T_{C,sc}}{\partial p_i} = \frac{V_m \Delta \alpha_i}{\Delta(c/T)}$, where the subscript i refers to the orthorhombic axis, $V_m = 3.14 \times 10^{-5}$ m^3/mol is the molar volume and $\Delta(c/T)$ is the step in the specific heat divided by temperature at the transition. The specific heat data we use for the Ehrenfest analysis are shown in Fig. 4.6 and we obtain the idealized steps $\Delta(c/T)_{FM} = 16.6$ mJ/molK^2 and $\Delta(c/T)_{sc} = 43.6$ mJ/molK^2. We remark that these particular data were obtained [129] on a different UCoGe crystal (RRR = 87) cut from the same batch as crystal 2. The step sizes in α_i and the resulting uniaxial and hydrostatic pressure dependencies are given in Table 4.1. The largest uniaxial pressure effect is along the b-axis (p_b) for both the ferromagnetic and superconducting phase transitions. For p_a and p_c the effect is smaller and the sign is reversed compared to p_b. The calculated

Table 4.1: Idealized steps in α_i at the ferromagnetic (FM) and superconducting (SC) phase transitions for $i = a$, b and c and the volume effect for UCoGe crystal 2 in zero field. The uniaxial and hydrostatic pressure dependencies of T_C and T_{sc} are calculated using the Ehrenfest relation (see text).

	a	*b*	*c*	*volume*
$\Delta\alpha_{FM}$ (10^{-7}/K)	3.3 ± 0.5	-33.2 ∓ 2.3	16.7 ± 1.1	-13.2 ∓ 2.0
$\partial T_C/\partial p_i$ (K/kbar)	0.06 ± 0.01	-0.63 ∓ 0.04	0.32 ± 0.02	-0.25 ∓ 0.04
$\Delta\alpha_{SC}$ (10^{-7}/K)	-4.9 ∓ 0.3	21.1 ± 2.3	-7.5 ∓ 0.5	8.7 ± 0.9
$\partial T_{SC}/\partial p_i$ (K/kbar)	-0.03 ∓ 0.001	0.15 ± 0.01	-0.05 ∓ 0.003	0.07 ± 0.01

hydrostatic pressure variations amount to $\partial T_C/\partial p = -0.25$ K/kbar and $\partial T_{sc}/\partial p$ = 0.07 K/kbar. These values should be compared to $\partial T_C/\partial p = -0.79$ K/kbar and $\partial T_{sc}/\partial p$ = 0.10 K/kbar calculated with the Ehrenfest relation on a crystal comparable to crystal 1 as reported in Ref. [130]. Our calculated values for the data shown here are close to the $\partial T_C/\partial p = -0.21$ K/kbar and $\partial T_{SC}/\partial p$ = 0.03 K/kbar values extracted from pressure dependent experiments [132, 131, 133].

4.4.2 Grüneisen analysis

In the top panel of Fig. 4.6 we present the volumetric thermal expansion coefficient divided by temperature, β/T, of UCoGe crystal 2, whereby $\beta = \alpha_a + \alpha_b + \alpha_c$. The ferromagnetic ordering results in a broad drop in β/T below T_C, while the superconducting transition results in a sharp peak. In the paramagnetic phase, β follows a linear temperature variation $\beta_P = a_P T$ ($T \leq 5$ K) with $a_P = 3.2 \times 10^{-7}$ K^{-2}. Also in the ferromagnetic phase, β/T attains a constant value with $a_{FM} = -2.4 \times 10^{-7}$ K^{-2}. The relative volume change due to the ferromagnetic ordering and superconductivity is obtained by integrating $\beta(T)$ versus T and is shown in the inset of Fig. 4.6. $\Delta V/V$ grows quadratically below the Curie point and decreases below 0.6 K due to superconductivity with $\Delta V/V = -2.8 \times 10^{-7}$ for $T \to 0$. The latter value gives the spontaneous magnetostriction of the superconducting state and agrees well with the value previously obtained on UCoGe [130] and other heavy-fermions superconductors such as URu_2Si_2 [134] and UPt_3 [135].

The effective Grüneisen parameter Γ is determined as $\Gamma(T) = \frac{V_m}{\kappa_T}\frac{\beta(T)}{c(T)}$, where κ_T is the isothermal compressibility and $\beta(T)$ the volume expansion. For UCoGe κ_T

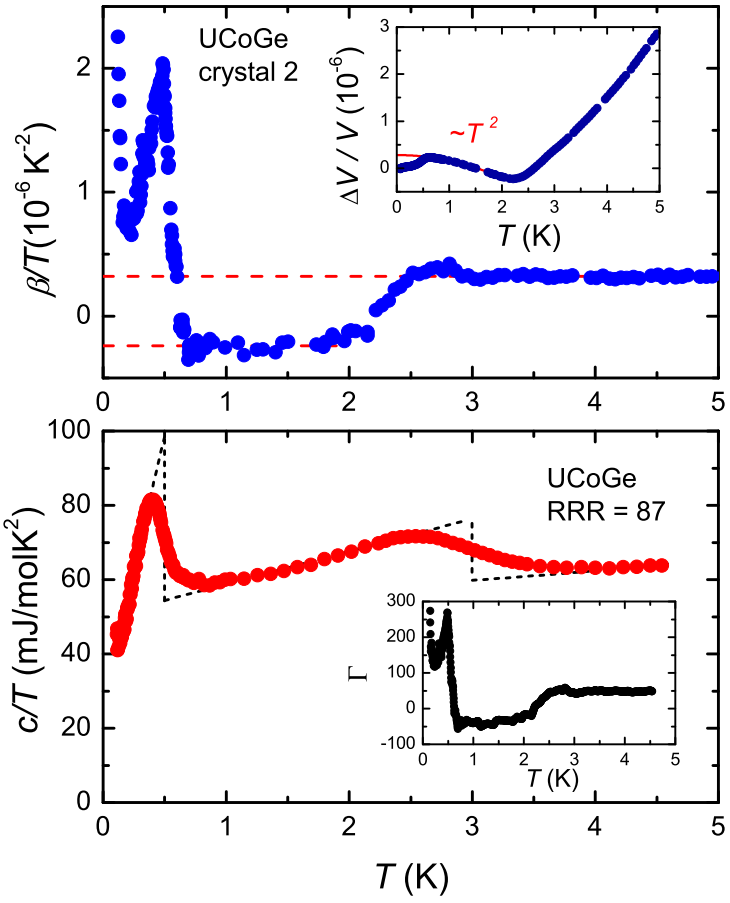

Figure 4.6: Top panel: Coefficient of the volumetric thermal expansion divided by temperature, β/T, as a function of temperature of UCoGe (crystal 2). Inset: Temperature variation of the relative volume change $\Delta V/V$ of the same sample. Bottom panel: Specific heat divided by temperature, c/T, as a function of temperature of UCoGe (data taken from Ref. [129]). Inset: Temperature variation of the Grüneisen parameter, Γ.

= 0.324 Mbar^{-1}, which was determined from the sum of the measured linear compressibilities along the *a*-, *b*- and *c*-axes [136, 137]. The resulting temperature dependence of the Grüneisen parameter is shown in the inset to the bottom panel of Fig. 4.6. Above the Curie point, $\Gamma = 50$. Upon cooling Γ drops to a value of about -50 due to the ferromagnetic ordering and then dramatically increases to a value of about 300 due to the SC. In general, it is observed that Grüneisen parameter increases rapidly with decreasing temperature as the heavy-fermion state stabilizes [138, 134].

4.4.3 Phase diagram

In Fig. 4.7 we present the superconducting and ferromagnetic phase diagram of UCoGe determined from the dilatometry data presented here. The $T_{sc}(B)$ and $T_C(B)$ data points are taken from the transverse and longitudinal thermal expansion experiments, respectively. In the case of B_{c2} for $B \parallel b$, we trace the transition points determined from the minima in $\alpha_b(T)$ (see Fig. 4.5). For $B \parallel c$, the Curie temperature could not be identified in field, as the magnetic transition smears out rapidly. In addition, the superconducting transition is suppressed near 0.5 T for $B \parallel c$. For $B \parallel a$, the Curie temperature is constant within the error bar at least up to 12 T, while T_{sc} is gradually suppressed, shifting out of the measurement window in fields exceeding 4 T. Lastly for $B \parallel b$, T_C shifts towards lower temperatures with increasing field. The field dependence of B_{c2} along the *b*-axis exhibits a remarkable *S*-shape, with superconductivity being enhanced above 6 T. The data in Fig. 4.7 therefore provide the first truly bulk sensitive evidence for the enhancement of superconductivity in fields oriented $B \parallel b$.

Returning to the magnetism, the field tuning of the Curie point can be fitted using a quadratic function proposed by Mineev [139, 89]: $T_C(B) = T_C(0)\left[1 - \left(\frac{B}{B_c}\right)^2\right]$. Extrapolation of the fit to this expression to $T \rightarrow 0$ indicates the critical field B_c could amount to as much as 19.6 T (see Fig. 4.7). This value is higher than $B_c = 16$ T deduced from the transport data [87]. On the other hand, T_C for $B \parallel b$ is determined from the longitudinal thermal expansion experiment for which precise field-angle tuning was not possible. As it is likely that $T_C(B)$, just like $T_{sc}(B)$, depends strongly on the field-angle, a small misorientation could therefore result in a larger value for B_c for the data presented and analysed here. Relevant to this discussion is the fact that B_{c2} for $B \parallel b$ extracted from the longitudinal thermal expansion (see the inset of Fig. 4.3) does not show the characteristic *S*-shape seen in Fig. 4.7, which can be

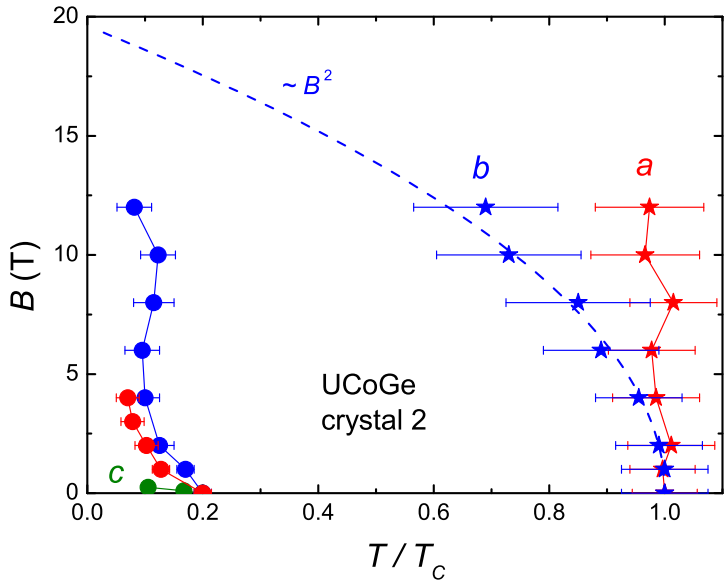

Figure 4.7: Superconducting (solid circles) and ferromagnetic (stars) $B-T$ phase diagram of UCoGe (crystal 2) plotted as a function of the reduced temperature T/T_C, where T_C is the Curie temperature. T_{sc} and T_C for $B \parallel a, b$ and c are given by red, blue and green symbols. The blue dashed line represents the function $f(B) = 1 - \left(\frac{B}{B_c}\right)^2$, where B_c = 19.6 T.

explained by a small misorientation of the b-axis with respect to magnetic field in the longitudinal data.

Finally, the low-temperature upturn in the $\alpha_b(T)$-data for crystal 2 for $T < 0.15$ K remains puzzling. A similar upturn is not seen in $\alpha_a(T)$ and $\alpha_c(T)$. Therefore we can safely exclude it is due to an artefact of the experiment, such as an undesired cell-effect (*i.e.* the expansion of the dilatometer itself), or another purely measurement-related technical problem. Additionally, this upturn was not observed in the $\alpha_b(T)$-data taken on a different crystal [130]. The possibility that the upturn is a high-temperature tail of a Schottky anomaly due to nuclear magnetic moments can be excluded since the upturn is insensitive to magnetic fields applied along the b-axis (see Fig. 4.3). Moreover, an analogously anomalous contribution to the specific heat below 0.15 K is not observed (see Fig. 4.6). We conclude the origin of the upturn in α_b is not understood and further experimental work is needed. The low temperature specific heat data point to a finite γ-value of 30 mJ/molK^2 when c/T as a function of T is linearly extrapolated to $T \to 0$ [129]. This value is about half of the normal state γ-value, which could indicate that only one of the spin-split bands takes part

in the superconducting condensate [27, 26].

4.5 Conclusions

Using a purpose-built, high resolution dilatometer coupled to a precision rotation stage, we have measured the thermal expansion of a single crystal of UCoGe around the ferromagnetic and superconducting transitions in magnetic fields up to 12 T applied along the orthorhombic axes. In order to enable fine-tuning of the magnetic field angle our home-built compact dilatometer was mounted on a piezo-electric rotator. Pronounced steps in the thermal expansion coefficient α were detected at T_C and T_{sc} and their field variation was used to establish the ferromagnetic and superconducting phase diagram. For small fields $B \parallel c$, the ferromagnetic transition becomes a cross-over and superconductivity is rapidly suppressed (B_{c2} is only 0.5 T for $T \to 0$). For $B \parallel a, b$, the Curie point and superconductivity are seen to persist to very high fields, well in excess of the Pauli limit. The dilatometry data also present a robust and importantly a bulk sensitive conformation of the S-shape of the upper-critical field, B_{c2}, for $B \parallel b$ and the enhancement of superconductivity above 6 T. The Curie point is seen to shift towards lower temperatures in the same field regime. These data lend further support to theoretical proposals of spin-fluctuation mediated enhancement of superconductivity in UCoGe for $B \parallel b$.

Chapter 5

Magnetotransport, magnetostriction and torque magnetometry study of UCoGe

In this chapter we investigate the electronic properties of the superconducting ferromagnet UCoGe by means of magnetoresistance, magnetostriction and torque magnetometry measurements. The experiments are carried out on single-crystalline samples for a field applied along the orthorhombic c-axis. We confirm a pronounced anomaly at a characteristic field B^* = 9 T in the magnetoresistance. In the magnetostriction and the magnetic torque data the anomaly is less prominent. This indicates the anomaly is not due to a magnetic transition, but rather to a Lifshitz transition, in line with the recent literature [Bastien *et al.*, PRL 117, 206401 (2016)]. Magnetoresistance measurements under high pressures of up to 1.5 GPa show B^* increases quadratically with pressure. Furthermore, Shubnikov-de Haas oscillations are detected in the magnetoresistance for $B \parallel c$ with frequencies f_α = 250 $\pm$ 20 T and f_β = 300 $\pm$ 30 T and heavy quasiparticle masses of $14m_e$ and $18m_e$ (m_e is the free electron mass) respectively are extracted. The presence of the orbits α and β for $B \parallel c$ indicates the existence of a pair of small Fermi surface pockets of comparable cross-section that occupy only a tiny portion of the Brillouin zone.

5.1 Introduction

In this chapter we focus on the electronic properties of UCoGe in applied magnetic field, particularly for a field applied along the c-axis ($B \parallel c$). UCoGe is an uniaxial ferromagnet with a spontaneous magnetic moment m_0 of 0.07 μ_B per U-atom, which points along the c-axis [125]. The superconducting and ferromagnetic properties are highly anisotropic, as was discussed in the previous chapter. The upper-critical field for a field along the c-axis is small, B_{c2} = 0.5 T for $T \rightarrow 0$ K. In an applied field, the FM transition becomes a cross-over and a clear Curie point is no longer observed. In UCoGe the *5f*-electrons are responsible for both the magnetism and the superconductivity. In order to understand the nature of the superconducting and ferromagnetic ground state, a detailed study of the electronic and magnetic structure is needed. In the last five years many research groups have dived onto this topic. High-field magnetisation measurements carried out at T = 1.5 K have shown [140] the magnetization $M(B \parallel c)$ grows significantly to a value of 0.7 μ_B at 53 T. The increase of $M(B \parallel c)$ is gradual, no structure in the magnetization curve is observed, except a weak decrease of the slope dM/dB around 23 T. $M(B \parallel a)$ is linear up to 53 T, while $M(B \parallel b)$ shows significant enhancement of the slope near 46 T. In the early polarized neutron diffraction (PND) work [141] on UCoGe it was demonstrated that by increasing $B \parallel c$ (up to 12 T) the U moment grows and induces a substantial moment on the Co atom directed antiparallel to the U moment. Surprisingly, in the latest PND measurements [142] on UCoGe doped with Ru on the Co site (with doping levels of 3 at.% and 12 at.%), a parallel orientation of the U and Co moments in field has been established. Similar controversial results appeared in the X-ray magnetic circular dichroism (XMCD) experiments. The first XMCD study [143] of UCoGe shows that the Co *3d* moments are parallel to the U *5f* moments. The second work [144] rules out the parallel coupling of the U and Co moments. The contradiction in the interpretation of the experimental results calls for a further detailed investigation of the magnetic properties of UCoGe in magnetic fields applied parallel to the c-axis.

Here we report magnetoresistance, magnetostriction and magnetic torque measurements on UCoGe. We confirm the presence of a characteristic field B^* = 9 T for $B \parallel c$, previously observed by magnetotransport [145], using all three techniques. High-pressure magnetoresistance measurements show B^* to increase with pressure. B^* also increases when the direction of B is tilted away from the c-axis. Shubnikov –

de Haas (SdH) oscillations with two characteristic frequencies were observed in the magnetoresistance at very low temperatures. The resolvable Fermi surface pockets are small and the extracted effective masses of $14m_e$ and $18m_e$ (m_e is the free electron mass) are relatively heavy. These results are discussed in terms of a Lifshitz transition, in which an applied magnetic field drives a change in Fermi surface topology.

5.2 Experimental

Single crystals of UCoGe were prepared in a tri-arc furnace by the Czochralski technique. All results presented in this chapter were obtained on three single crystals: sc1 with RRR = 30, sc4 with RRR = 8 and sc2013 with RRR = 6 - 8. Samples were cut from the crystals by means of spark erosion into a bar shape or parallelepiped. Additional information about the crystal synthesis and the characterisation can be found in Ref. [128] and in Chapter 3.

The coefficient of magnetostriction, $\lambda' = L^{-1}(dL/dB)$, with L the sample length, was measured using a three-terminal parallel-plate capacitance method. The design of the home-built sensitive dilatometer was based on the one reported in Ref. [117] and is presented in detail in Chapter 3. The sensitivity of the thermal expansion cell is 0.03 Å. The dilatometer was used in the longitudinal configuration in which the dilatation axis, ΔL, and the direction of the magnetic field are parallel, $\Delta L \parallel B$, and in the transverse configuration when $\Delta L \perp B$. For the magnetostriction measurements two crystals were used: sc1 with dimensions $a \times b \times c = 1.0 \times 5.0 \times 1.1$ mm^3 and sc2013 with dimensions $a \times b \times c = 2.3 \times 4.4 \times 3.5$ mm^3.

The ac-resistivity data were acquired using a low-frequency (f = 16 Hz) resistance bridge or a phase sensitive detection technique using a lock-in amplifier with a low excitation current (I = 100 μA). In order to observe quantum oscillations in the resistance of UCoGe, low-noise measurements of the magnetoresistance are needed. A pre-amplification of the magnetoresistance signal was achieved by placing a cryogenic low-impedance transformer into the field-compensated region of the dilution refrigerator. For the magnetoresistance measurements, the bar-shaped crystals sc2013 and sc1 were used.

High-pressure magnetotransport measurements were carried out with help of a hybrid clamp cell made of NiCrAl and CuBe alloys. The crystal was mounted on a plug that was placed in a Teflon cylinder with Daphne oil 7373 as a hydrostatic

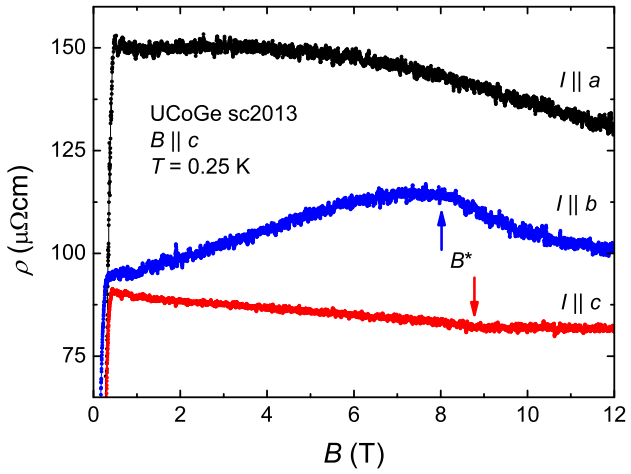

Figure 5.1: Magnetoresistance of UCoGe for $B \parallel c$ recorded for T = 0.25 K. The black ($I \parallel a$) and blue ($I \parallel b$) curves were taken in transverse configuration ($B \perp I$) for a sample sc2013 with RRR = 6 and 8, respectively, while the red curve is taken in the longitudinal configuration ($B \parallel I \parallel c$) for a sample sc2013 with RRR = 7. The arrows indicate B^*.

pressure transmitting medium. For the resistance measurements in a 4-point configuration, thin gold wires were attached to the flat sides of the crystals using silver paste. The bar-shape sample used for this experiment is labeled sc4.

The torque magnetometry technique makes use of a thin cantilever, which was described in Chapter 3. The samples used in these experiments are labeled sc1 with typical dimension $0.5 \times 0.5 \times 0.5$ mm^3 and $0.1 \times 0.1 \times 0.5$ mm^3. They were fixed to the top part of the flexible cantilever plate using GE varnish. The cantilever was mounted on the single-axis piezo-rotator ANRv51/RES (Attocube).

Low temperatures were achieved by attaching the dilatometer, the pressure cell, the transport platform or the cantilever to the cold plate of a ^{3}He refrigerator with $T = 0.24 - 10$ K and magnetic fields up to 14 T (Heliox, Oxford Instruments), or to the cold plate of the dilution refrigerator for $T = 0.03 - 1$ K and B up to 17 T (Kelvinox, Oxford Instruments). In addition, torque magnetometry experiments were carried out at the High Field Magnet Laboratory in Nijmegen in a ^{3}He refrigerator and fields up to 30 T.

5.3 Results

5.3.1 Magnetoresistance for $B \parallel c$

Fig. 5.1 shows the resistivity as a function of magnetic field, $\rho(B)$, at temperature T = 0.25 K for three samples with comparable RRR. The electrical current, I, was applied along the a-, b- or c-axis while B was always aligned along the c-axis. The black ($I \parallel a$) and blue ($I \parallel b$) curves were taken in the transverse configuration ($B \perp I$), while the red ($I \parallel c$) curve is taken in the longitudinal configuration ($B \parallel I$). The steep increase of $\rho(B)$ at small fields is due to the suppression of superconductivity with $B_{c2} \simeq 0.2$ T at T = 0.25 K. Here we focus on the normal state magnetoresistance.

It is clear that there is a dependence of $\rho(B)$ on the current direction. The resistivity value in the transverse configuration is higher that in the longitudinal one. The presence of the additional resistance when $B \perp I$ is normally attributed to the Lorentz force. In the case of $I \parallel b$ $\rho(B)$ steadily increases and passes through a pronounced maximum at B^* = 8.0 $\pm$ 0.5 T, while for $I \parallel a$ $\rho(B)$ steadily decreases. The longitudinal magnetoresistance shows a kink near 9 T. This observation of the kink for $B \parallel c \parallel I$ is consistent with the data reported earlier [145] on a UCoGe crystal with RRR = 5. On the other hand, high quality samples with RRR greater than 30 show a somewhat different behaviour in the magnetoresistance [146, 147], but with a clear anomaly around 9 T.

5.3.2 Magnetoresistance for $B \parallel c \parallel I$ under hydrostatic pressure

The pressure variation of B^* was investigated for the sample sc4 (RRR = 8) for $B \parallel c \parallel I$ for pressures up to 1.29 GPa in the ^{3}He refrigerator and for $p \geq 1.29$ GPa in the dilution refrigerator. The measurements taken at T = 0.25 K are shown in Fig. 5.2. After the initial steep rise, again due to the suppression of superconductivity, $\rho(B)$ steadily decreases and shows a kink at B^* = 9 T, like $\rho(B)$ of the crystal sc2013 in Fig. 5.1. Under pressure, B^* shifts to higher fields in a quadratic fashion at the rate of 3.0 T/GPa^2 (as shown in the inset to Fig. 5.2 showing $B^*(p)$ at T = 0.25 K and 1 K). In this temperature range B^* and dB^*/dp are temperature independent.

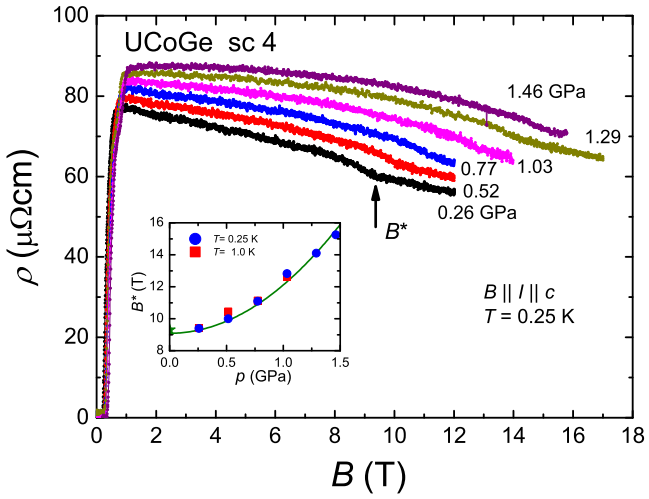

Figure 5.2: Magnetoresistance of UCoGe (sc4) for $B \parallel c \parallel I$ at pressures of 0.26, 0.52, 0.77, 1.03, 1.29 and 1.46 GPa, as indicated, at T = 0.25 K. The inset shows B^* as a function of pressure at T = 0.25 K (blue circles) and T = 1 K (red squares). The value of $B^*(0)$ = 9 T at ambient pressure (green star) is taken from sample sc2013. The green solid line is a fit to the data at T = 0.25 K with $B^* = B^*(0) + bp^2$, where b = 3.0 T/GPa^2.

5.3.3 Magnetostriction for $B \parallel c$

The relative length change of UCoGe, $\Delta L/L(B)$, was measured on two samples (sc1 and sc2013) for $B \parallel c$. The data with ΔL along the a-, b- and c-axes are reported in Fig. 5.3. With the magnetic field applied along the c-axis, the sample shrinks along the a- and c-axes, while it expands along the b-axis. The magnitude of the relative length change in the latter case is the largest and reaches the value of $\Delta L/L = 12 \times 10^{-5}$ at B = 12 T. The temperature dependence of the magnetostriction, measured for T up to 10 K, is weak at low field, but becomes significant in fields above 8 T. In the raw data for $\Delta L \parallel c \parallel B$ one can see a saturation in the magnetostriction signal at B^* = 9 T. The derivative of the relative length change, *i.e.* the linear magnetostriction coefficient λ', at T = 0.3 K, is reported for each configuration in the insets in Fig. 5.3. λ' first grows (for $\Delta L \parallel a, c$) or drops (for $\Delta L \parallel b$) with increasing field due to the SC phase transition. Around B^* = 9 T, the linear magnetostriction coefficient has an anomaly. The anomaly is best seen as a kink for $\Delta L \parallel c$ and a maximum for $\Delta L \parallel b$ in the data. In case of $\Delta L \parallel a$ λ' does not changes significantly near B^*.

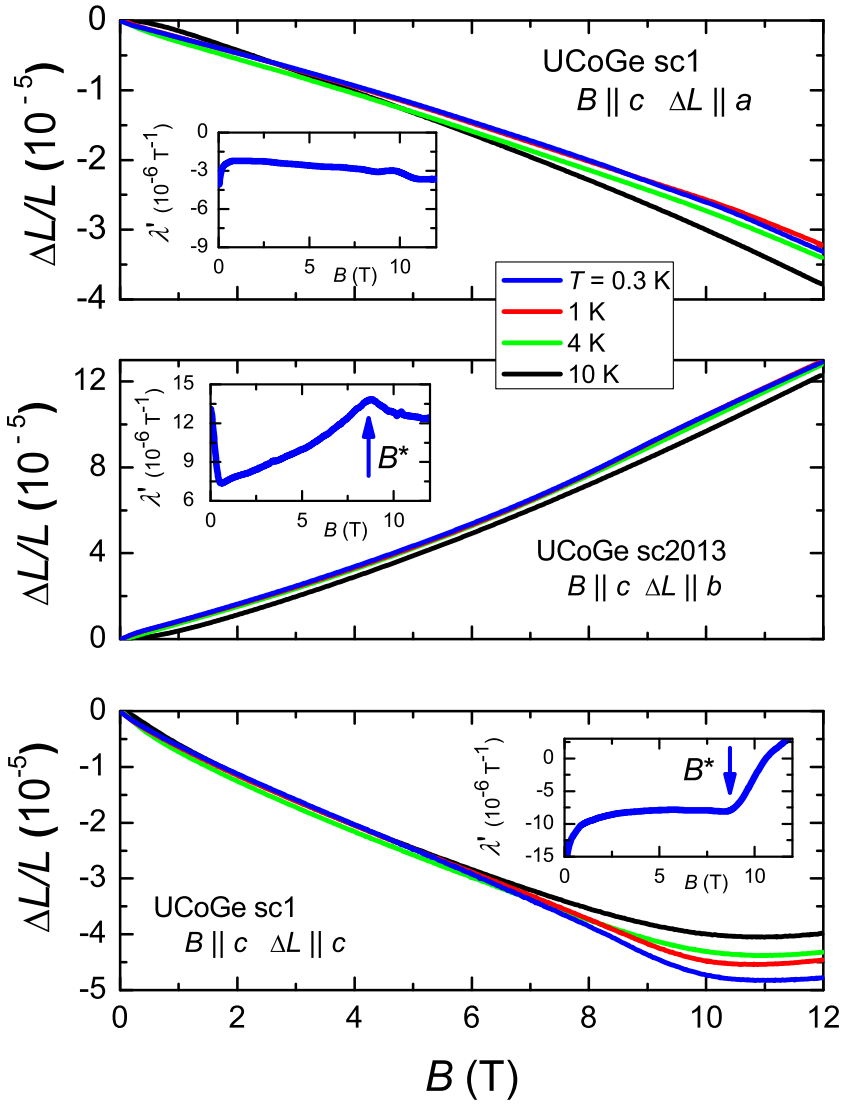

Figure 5.3: The relative length change of UCoGe, $\Delta L/L$, as a function of applied magnetic field along the c-axis and the dilatation direction, ΔL, measured along the a-axis (sc1, top panel), along the b-axis (sc2013, middle panel) and along the c-axis (sc1, bottom panel). Temperatures are T = 0.3 K, 1 K, 4 K and 10 K, as indicated. The insets show the linear magnetostriction coefficient, λ', at T = 0.3 K.

5.3.4 Magnetic torque

The magnetic torque is expressed as $\tau = \mathbf{M} \times \mathbf{B}$, where $\mathbf{M}$ is the magnetisation vector. In UCoGe the ordered magnetic moment aligns along the easy axis below the Curie point, thus $\mathbf{M} \parallel c$. In our experiments we used a capacitive cantilever to measure the torque $\tau \propto \Delta C$. The sample was mounted on the flexible plate in the way that the c-axis of the UCoGe crystal was perpendicular to the plate. The schematic drawings of the cantilever were presented in Chapter 3. By using a rotator, we were able to change the angle, θ, between the c-axis of the crystal and the applied magnetic field. When $\theta > 0$ the gap between the capacitance plates, d, increases when B increases which results in the torque appearing as a decreasing signal. When $\theta < 0$, τ increases with increasing the field. The resulting curves are shown in Fig. 5.4. The magnetic torque was measured on sample sc1, which was cut into a cube (size $0.5 \times 0.5 \times 0.5\,\mathrm{mm}^3$). The magnetic torque of the cube-shaped sample was measured at T = 0.30 K in fields up to 12 T (Fig. 5.4(a)) and at T = 0.05 K in fields up to 15 T (Fig. 5.4(b)). τ gradually increases ($\theta < 0$) or decreases ($\theta > 0$) with increasing B. In order to detect the B^* anomaly, we plot the derivative $d(\Delta C)/dB$ in Fig. 5.4(c) and (d). The anomaly is hard to see on the derivative of the torque yet still detectable. B^* shifts towards higher field with increasing angle, θ. We tracked the anomaly in $d(\Delta C)/dB$ for both temperatures as a function of θ and the resulting data points are shown in Fig. 5.4(f) together with the data obtained from the magnetoresistance at T = 0.15 K [148]. One can see a clear match of the $B^*(\theta)$ detected in the torque measurements at T = 0.05 K with $B^*(\theta)$ from the maximum of $\rho(B)$. $B^*(\theta)$ at T = 0.3 K deviates from the $\rho(B)$ data, but qualitatively follows the same trend. The magnetic torque was also measured in high magnetic fields up to 30 T at T = 0.32 K (see Fig. 5.4(e)). These experiments were carried out on a tiny bar-shaped crystal (size $0.1 \times 0.1 \times 0.5\,\mathrm{mm}^3$). The data show the torque signal has a relatively smooth field variation up to 30 T, in agreement with the magnetization data [140].

5.3.5 Quantum oscillations

The oscillations in the resistivity that occur at low temperatures in the presence of a strong magnetic field, the Shubnikov–de Haas effect, carry information about the Fermi surface of the material. In order to detect the SdH signal we have pre-amplified *in situ* the magnetoresistance signal $\rho(B)$ using a cryogenic transformer [114].

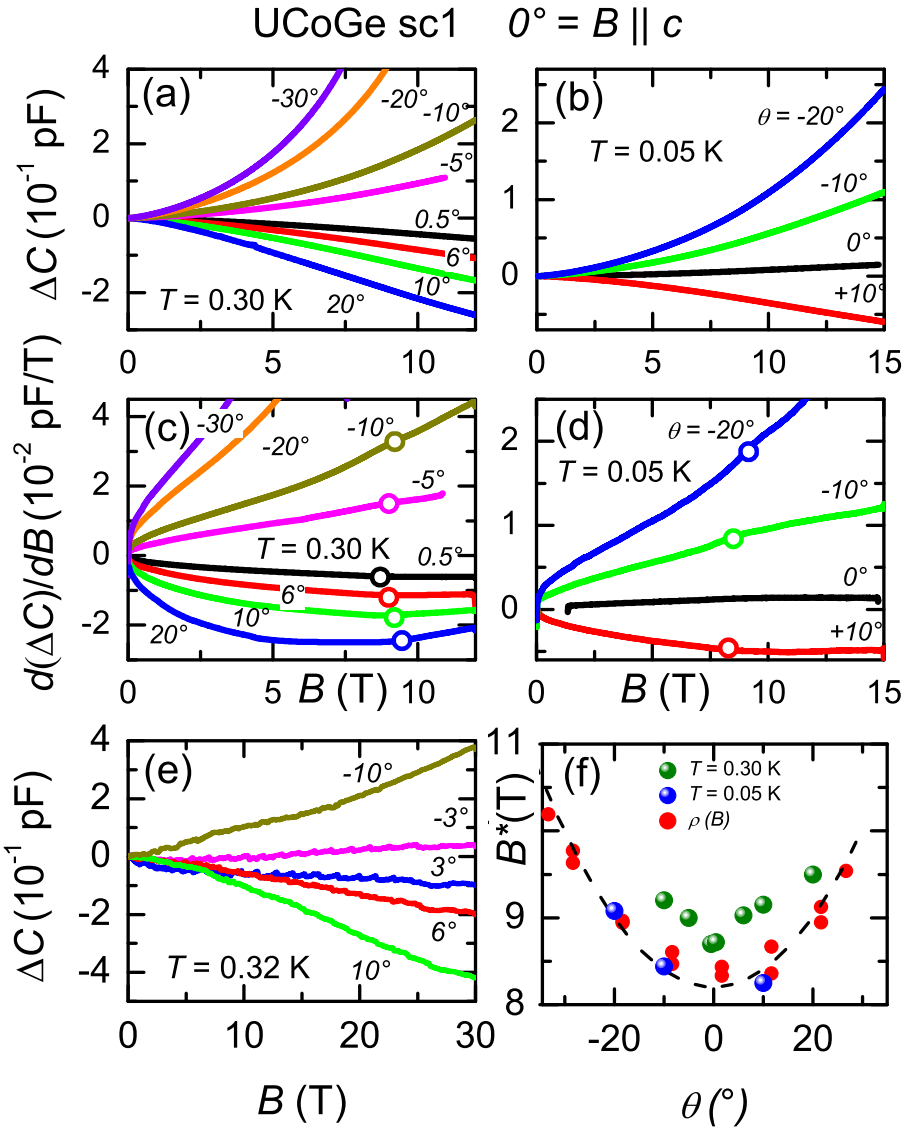

Figure 5.4: The magnetic torque, ΔC, of UCoGe sample sc1 (cube) as a function of the applied field at T = 0.30 K (a) and T = 0.05 K (b) at different angles, θ, as indicated. θ is the angle between the c-axis of the crystal and the magnetic field. Panels (c) and (d): $d(\Delta C)/dB$ as a function of B at T = 0.30 K and T = 0.05 K respectively at different θ as indicated. Open circles indicate B^*. Panel (e): The magnetic torque, ΔC, of UCoGe sample sc1 (bar) as a function of the applied field (up to 30 T) at T = 0.32 K. Panel (f): B^* as a function of θ, where θ = 0 corresponds to $B \parallel c$. Green points are determined by tracking the "kink" field in the $d(\Delta C)/dB$ curve at T = 0.30 K (c) and blue points at T = 0.05 K (d). Red points are $B^*(\theta)$ determined by the magnetoresistance data on sc1 at T = 0.15 K (from Ref. [148]). The dashed line represents $B^* = B^*(0)/cos(\theta)$.

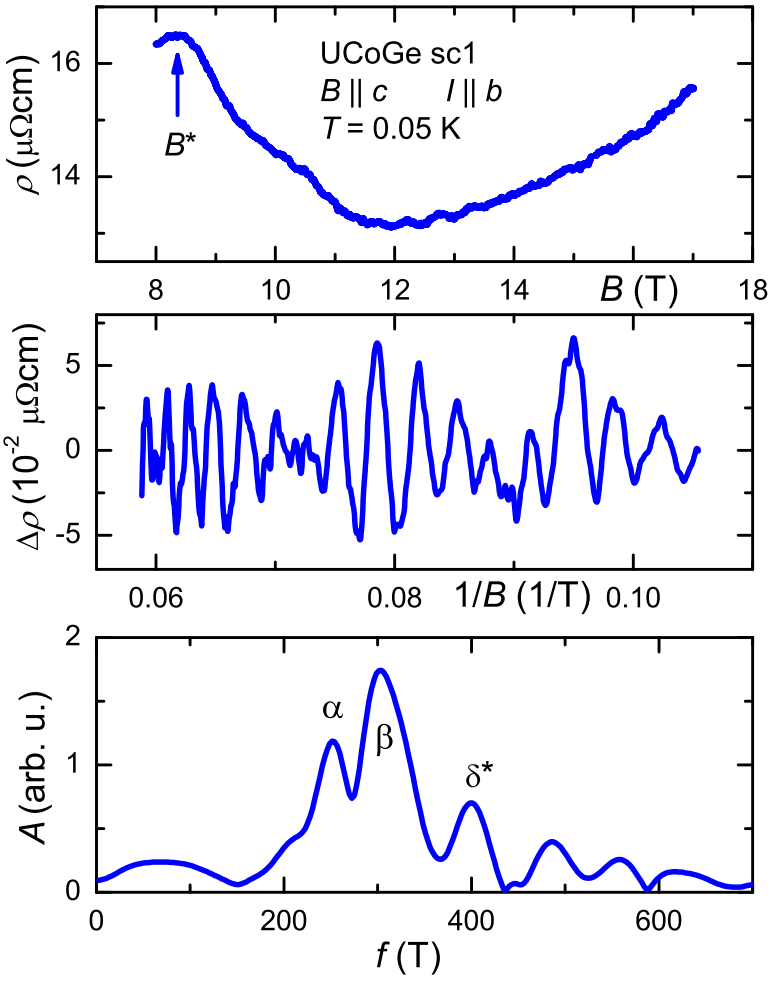

Figure 5.5: Top panel: The magnetoresistance of UCoGe sc1 for $B \parallel c$ and $I \parallel b$ at $T = 0.05$ K. Middle panel: Shubnikov–de Haas oscillations, $\Delta\rho$, as a function of inverse field, $1/B$. Bottom panel: The amplitude of the Fast Fourier Transform, A, as a function of frequency, f. Two main frequencies are detected, labeled α and β, with values $f_\alpha = 250 \pm 20$ T and $f_\beta = 300 \pm 30$ T. Figures are adapted from Ref. [114].

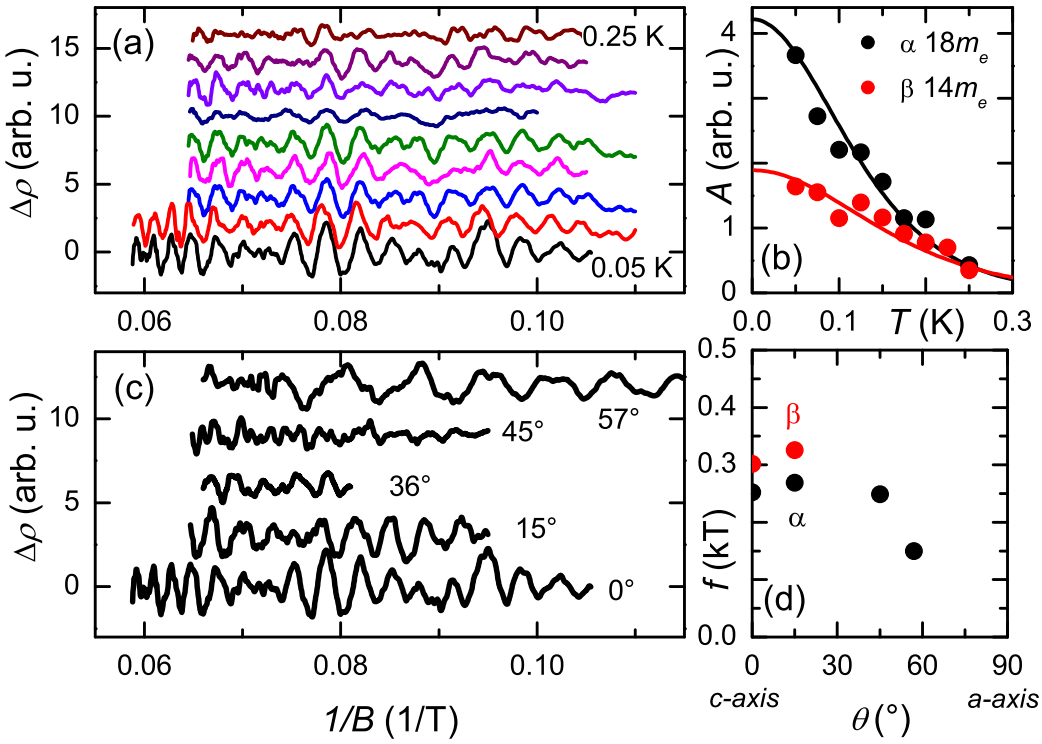

Figure 5.6: Panel (a) and (c): Shubnikov–de Haas oscillations, $\Delta\rho$, of UCoGe sc1 as a function of the inverse field, $1/B$, at different temperatures from T = 50 mK up to 250 mK with steps of 25 mK (a) and at T = 50 mK and at different angles as indicated (c). Panel (b): The temperature variation of the amplitude of the Fast Fourier Transfom (FFT), A, for different frequencies: α – black points and β – red points. The solid lines represent the Lifshitz-Kozevich function with m_α* = 18 m_e (black solid line) and m_β* = 14 m_e (red solid line). Panel (d): The angular variation of the frequencies obtained by FFT for f_α – black points and f_β – red points. θ = 0 corresponds to $B \parallel c$. Figures are adapted from Ref. [114].

The magnetoresistance of UCoGe (sc1) for $B \parallel c$ and $I \parallel b$ in the range 8 - 17 T at T = 0.05 K is shown in the top panel of Fig. 5.5. The SdH oscillations in the $\rho(B)$ signal become visible with the naked eye above 10 T. In the middle panel of Fig. 5.5 we present the SdH signal as a function of the inverse magnetic field, $1/B$, after careful subtraction of the non-monotonic background of the magnetoresistance. The characteristic beating pattern points to the mixing of two closely-spaced frequencies. A Fourier analysis of the quantum oscillations (bottom panel of Fig. 5.5) shows two main frequencies f_α = 250 $\pm$ 20 T and f_β = 300 $\pm$ 30 T with a presence of harmonics in the higher frequency region. Another relatively weak frequency $f_{\delta*}$ = 400 $\pm$ 20 T is present as well. In the following analysis, we will not focus on the latter frequency due to being close in amplitude to the noise.

The temperature variation of the SdH oscillations has been measured in order to determine the effective mass of the quasiparticles. $\Delta\rho$ as a function of $1/B$ in the temperature range 50 mK – 250 mK is presented in Fig. 5.6(a). The Fourier transforms were computed at all measured temperatures. The FFT amplitudes, A, of the α and β signal were obtained and analyzed using the standard Lifshitz-Kozevich relation: $LK(T) = Cm^*T/B_0/[sinh(Cm^*T/B_0)]$, where B_0 is the inverse of the average inverse magnetic field, C contains universal constants and is equal to 14.7 T/K, m^* is the quasiparticle mass. The results of the LK analysis are shown in Fig. 5.6(b) for the two main frequencies f_α and f_β. The values of the cyclotron effective masses are $m_\alpha{}^*$ = 18 m_e and $m_\beta{}^*$ = 14 m_e, where m_e is the electron mass.

A measurement of the field angle dependence of the SdH signal allows one, in principle, to determine the shape of the Fermi surface. In Fig. 5.6(c) we show the SdH oscillations as a function of $1/B$ at T = 50 mK for different angles, θ. Here the sample was rotated from $B \parallel c$ to $B \parallel a$ with increasing θ. The angular dependence of the oscillation frequencies is presented in Fig. 5.6(d). The β orbit can no longer be detected for $\theta > 15^\circ$. The α orbit remains present for $\theta < 60^\circ$ while its frequency decreases. The δ^* orbit was not observed in the FFT spectra for $\theta > 0$.

5.4 Analysis and discussion

The major result from the magnetoresistance, magnetostriction and the magnetic torque measurements is the identification of a pronounced structure in the field variation at B^* = 9 T. The characteristic field B^* is a robust property of our samples, but

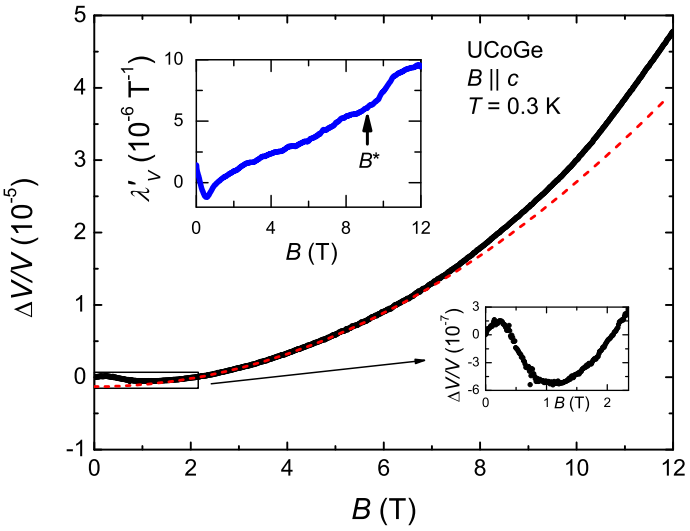

Figure 5.7: The relative volume change, $\Delta V/V$, of UCoGe as a function of applied magnetic field along the c-axis at T = 0.3 K. The red dashed line represents a quadratic function $f(B) = (0.28 \times B^2 - 1.30) \times 10^{-6}$. The upper inset shows the volumetric magnetostriction coefficient, λ'_V, at T = 0.3 K. The arrow indicates B*. The lower inset shows a zoom of $\Delta V/V(B)$ for low fields.

the shape of the structure in the magnetoresistance depends on the direction of the electrical current (see Fig. 5.1) and the quality of the samples [146].

The magnetostriction of UCoGe shows that the anomaly around B* is the strongest for the longitudinal configuration $B \parallel c \parallel \Delta L$. In this case $\Delta L(B)$ saturates for $B >$ 9 T. In other words, the sample shrinks in a field applied along the c-axis up to B* and then keeps a constant length up to 12 T for temperatures T = 0.3 - 10 K. The dilatation along the a-axis follows a negative trend with increasing field with a small change above B*. On the other hand, for $B \parallel c$ and $\Delta L \parallel b$ we observe $\Delta L(B)$ increasing with a weak change of slope $d(\Delta L)/dB$ near 9 T. These magnetostriction data show that the b-axis of UCoGe is the "softest" axis (largest change in ΔL) of the crystal in terms of elastic properties for $B \parallel c$. A similar conclusion was reached from the thermal expansion measurements presented in Chapter 4. The relative volume change, $\Delta V/V$, is presented as a function of $B \parallel c$ in Fig. 5.7. $\Delta V/V$ is calculated as a sum of the relative length change for each direction. It shows that the volume of the unit cell of UCoGe in applied magnetic field along the c-axis first expands for $B < 0.2$ T due to suppression of the superconductivity (see the lower insert of Fig. 5.7), then shrinks until 1.2 T, which we attribute to the smearing of the ferromagnetic contri-

bution, and expands with further increase of the magnetic field up to 12 T. $\Delta V/V(B)$ grows quasi-quadratically in the field region 1.2 - 7.5 T and then its behaviour deviates from the quadratic function (dashed line in Fig. 5.7). The volumetric magnetostriction coefficient, λ'_V, is presented in the upper inset of Fig. 5.7, with the arrow pointing to the position of B^*. λ'_V is related to the hydrostatic pressure dependence of the magnetization M by one of the Maxwell relations: $\left(\frac{\partial M}{\partial p}\right)_{B,T} = -\left(\frac{\partial V}{\partial B}\right)_{p,T}$. For a quadratic field dependence of the volume magnetostriction, $\Delta V(B)$, a linear field dependence of the magnetization M is necessary. Indeed, the literature data of $M(B)$ show that the magnetization measured for a field along the three crystallographic axes is quasi-linear in the field region 1 - 23 T [125, 140]. The contribution of the c-axis component to $\Delta V/V$ and λ'_V is rather small, consequently the anomaly at B^* hardly shows up in the volumetric magnetostriction.

An appealing scenario that has been put forward to explain the change in magnetoresistance at B^* is a ferro-to-ferrimagnetic transition [145]. This proposal is largely based on the first PND experiments on UCoGe (RRR = 30) carried out for $B \parallel c$ [141]. In low magnetic field (3 T) the small ordered moment m_0 is predominantly located at the U atom. In a large field of 12 T the moment grows but at the same time a substantial moment, antiparallel to the U moment, is induced on the Co site. This unusual polarizability of the Co 3d orbitals may give rise to a field-induced ferri-magnetic-like spin arrangement. Support for this scenario was obtained from field-dependent as-susceptibility data [145] on a crystal with RRR = 5 at T = 40 mK which exhibit a maximum near B^*. However, ac-susceptibility measurements performed on a sample with a similar RRR value did not confirm this result [115]. The dc-magnetisation $M(B)$ was measured on a crystal with RRR = 45 at T = 1.5 K in pulsed magnetic fields up to 53 T [140]. For $B \parallel c$ the data do not show a clear sign of a metamagnetic transition. A weak structure does appear in the derivative dM/dB near 23 T.

The magnetic torque of UCoGe shows that angular dependence of B^* follows the same trend as extracted from the magnetoresistance data. The main observation is that B^* shifts towards higher fields on rotating the magnetic field direction away from the c-axis. The effect we see in the torque magnetometry is rather weak. Therefore, it is difficult to interpret these data as a metamagnetic transition.

An alternative method to probe whether B^* is due to the magnetic transition is X-ray magnetic circular dichroism. In Ref. [144] a XMCD study in combination

with magnetic Compton scattering is reported which enables the separation of the contribution from spin and orbital moments. These experiments, carried out on UCoGe samples (RRR = 4) for $B \parallel c$ at T = 1.5 K and B = 6 T, show that the U and Co spin moments are antiparallel. The authors of this paper conclude that the total spin moment is smaller and is aligned antiparallel to the total orbital moment of UCoGe. However, XMCD experiments at the U $M_{4,5}$ and Co/Ge K edges demonstrate that the U and Co spin moments are parallel. The measurements have been done on high-quality samples of UCoGe with RRR = 30 for $B \parallel c$ at T = 2.1 K and B = 1 and 17 T [143]. The contradiction between the two latter result and the earlier work points to a high level of complexity of the magnetic state in UCoGe. Therefore, an additional PND study of Ru substituted UCoGe has been carried out [142]. This work also concludes the parallel orientation of U and Co moments in $URu_xCo_{1-x}Ge$ (with x = 0.03 and 0.12) for $B \parallel c$ at T = 0.3 K and B = 7 and 9 T. To conclude, the magnetisation, the torque magnetometry and XMCD experiments rule out the possibility that the B* structure is related to a reorientation of the spins or other related magnetic transition.

Recently, high-field magnetoresistance and thermopower measurements on high-quality crystals (RRR $\geq$ 36) showed [147] that at least five anomalies can be identified for $B \parallel c$, at B = 4, 9, 12, 16 and 21 T. The feature at B* = 9 T is observed by us in all crystals. The anomaly at 12 T can be identified in our results as the local minimum in the magnetoresistance seen in Fig. 5.5. These five anomalies are associated with Lifshitz transitions, field-induced topological changes of the Fermi surface. Experimental evidence for this was obtained by the detection of field-dependent quantum oscillations in the magnetoresistance and the thermopower. In Ref. [147] also the γ (α in our work) and the β orbit in the field region 9 - 16 T were reported, as well as their angular dependence. Furthermore, a large high frequency (1 kT) spherical Fermi pocket was observed for $B > 22$ T.

Our results show the characteristic beating pattern (see Fig. 5.5) emerging from two closely-spaced frequencies f_α = 250 T and f_β = 300 T. The orbits have heavy effective masses m_α* = 18 m_e and m_β* = 14 m_e. Assuming a circular extremal cross section and with help of the Onsager relation $A_k(E_F) = 2\pi ef/\hbar$, we calculate a Fermi cross section for the two orbits $A_\alpha = 2.3$ nm^{-2} and $A_\beta = 2.9$ nm^{-2}. The presence of these comparably-sized orbits, α and β, for $B \parallel c$ indicates the existence of a pair of small Fermi surface pockets that occupy only a tiny portion of the volume of the Brillouin zone. The angular dependence of the orbital cross-sections shows

that the β orbit gradually vanishes upon rotation of 15° or more towards the a-axis, while the frequency of the α orbit steadily decreases until a tilt of 57°. For this, we can state that the Fermi surface of UCoGe is expected to include a cigar-shaped (β) and an ellipsoidal Fermi pocket (α) in partial agreement with the LDA band structure calculations [149] and angle resolved photo-emission spectroscopy experiments [150]. Quantum oscillations were not detected by us for $B \parallel a$ on a crystal with RRR = 30.

To summarize, the observation of tiny Fermi surface pockets in transport both in this work and in Ref. [147] and thermopower measurements [147], together with the detection of a series of anomalies by several magneto-sensitive probes, provides convincing evidence for field-induced topological changes of the Fermi surface – or Lifshitz transition – for magnetic fields $B \parallel c$ in UCoGe.

5.5 Conclusions

We have presented an extensive magnetoresistance study of single crystals of UCoGe for magnetic fields directed along the c-axis. We confirm a pronounced structure in the magnetoresistance, which appears when the component of the field parallel to the c-axis reaches a value B^* = 9 T. Measurements of B^* as a function of pressure up to p = 1.5 GPa show a quadratic increase $B^*(p) = B^*(0) + bp^2$, where b = 3.0 T/GPa^2. The characteristic field B^* = 9 T is also observed in magnetostriction and magnetic torque measurements, albeit less prominently. The Fermi surface of UCoGe has been studied by means of quantum oscillations in the magnetoresistance. Two small Fermi surface pockets with heavy effective mass were detected. Our results are in good agreement with recent magnetoresistance and thermopower measurements [147] that revealed the presence of multiple anomalies as a function of the applied magnetic field $B \parallel c$, which demonstrate a field-induced dynamic reconstruction of the Fermi surface connected to several Lifshitz transitions.

Chapter 6

High-pressure study of the basal-plane anisotropy of the upper-critical field of the topological superconductor $Sr_xBi_2Se_3$

We report a high-pressure transport study of the upper-critical field, $B_{c2}(T)$, of the topological superconductor $Sr_{0.15}Bi_2Se_3$ ($T_c = 3.0$ K). $B_{c2}(T)$ was measured for magnetic fields directed along two orthogonal directions, a and a^*, in the trigonal basal plane. While superconductivity is rapidly suppressed at the critical pressure $p_c \sim 3.5$ GPa, the pronounced two-fold basal-plane anisotropy $B^a_{c2}/B^{a^*}_{c2} = 3.2$ at $T = 0.3$ K, recently reported at ambient pressure [Pan *et al.*, Sci. Rep. 6, 28632 (2016)], is reinforced and attains a value of ~ 5 at the highest pressure (2.2 GPa). The data reveal that the unconventional superconducting state with broken rotational symmetry is robust under pressure.

This chapter has been published as Nikitin *et al.*, Phys. Rev. B **94**, 144516 (2016)

6.1 Introduction

The tetradymite Bi_2Se_3 is one of the prototypical materials that played an instrumental role in developing the field of three-dimensional topological insulators [42, 151, 152]. Electronic structure calculations [101] predicted Bi_2Se_3 has a nontrivial topology of the electron bands due to large spin-orbit coupling. The bulk of the crystal is insulating and at the surface gapless states exist that are protected by symmetry. The topological surface states are characterized by a helical Dirac-type energy dispersion with the spin locked to the momentum. The topological properties have experimentally been confirmed by angle resolved photo emission spectroscopy (ARPES) [103, 153]. Most interestingly, the topological insulator Bi_2Se_3 can relatively easily be transformed into a superconductor with $T_c \sim 3$ K by doping with Cu [39], Sr [107], Nb [108] or Tl [109]. Making use of the direct analogy of the Bogoliubov-de Gennes Hamiltonian for the quasiparticles of a superconductor and the Bloch Hamiltonian for the insulator it is predicted that these doped systems are topological superconductors [151, 152]. Taking into account the Fermi surface topology in the normal state this can give rise to an odd-parity Cooper pairing symmetry and a fully gapped superconducting state [154, 155]. Among the Bi_2Se_3-based superconductors, $Cu_xBi_2Se_3$ has been studied most intensively [39, 156, 157, 158]. A topological superconducting state was concluded based on a two-orbital model for centrosymmetric superconductors exhibiting strong spin-orbit coupling. The possible superconducting order parameters were evaluated by symmetry-group classification (D_{3d} point group, $R\bar{3}m$ space group) and an interorbital spin-triplet state (Δ_2-pairing) was put forward as order parameter [155, 157]. On the other hand, scanning tunneling microscopy (STM) measurements [159] argue against unconventional superconductivity. Moreover, $Cu_xBi_2Se_3$ crystals are prone to sample inhomogeneities [159, 160] and a maximum superconducting volume fraction of only $\sim 50\%$ has been achieved [156, 160].

An exciting development in the field of Bi_2Se_3-based superconductors is the experimental observation of rotational symmetry breaking: a magnetic field applied in the trigonal basal-plane spontaneously lowers the symmetry to two-fold [41, 42]. In $Cu_xBi_2Se_3$ this was demonstrated for the spin-system by the angular variation of the Knight shift measured by nuclear magnetic resonance (NMR) [41], while specific heat measurements show it is a thermodynamic bulk feature [111]. In $Sr_xBi_2Se_3$ rotational symmetry breaking was detected by the angular variation of the upper-critical

field, $B_{c2}(\theta)$, probed by magnetotransport [42], and in $Nb_xBi_2Se_3$ by torque magnetometry that senses the magnetization of the vortex lattice [161]. The rotational symmetry breaking appears to be ubiquitous in Bi_2Se_3-based superconductors and provides additional evidence for topological superconductivity. Especially, it puts important constraints on the possible order parameters. According to recent models [113, 112, 105] it restricts the order parameter to an odd-parity two-dimensional representation, E_u, with Δ_4-pairing, which involves a nematic director that breaks the rotational symmetry when pinned to the crystal lattice. This unconventional superconducting state is referred to as nematic superconductivity.

Here we report a high-pressure magnetotransport study on single-crystalline $Sr_{0.15}Bi_2Se_3$, conducted to investigate the robustness of the rotational symmetry breaking to hydrostatic pressure. The upper-critical field, $B_{c2}(T)$, was measured for magnetic fields directed along two orthogonal directions, a and a^*, in the trigonal basal plane. While superconductivity is rapidly depressed with pressure, the pronounced two-fold basal-plane anisotropy $B^a_{c2}/B^{a^*}_{c2} = 3.2$ observed at $T = 0.3$ K at ambient pressure [42], is reinforced and attains a value of ~ 5 at the highest pressure (2.2 GPa). The rapid depression of T_c points to a critical pressure for the suppression of superconductivity $p_c \sim 3.5$ GPa. Recently, a similar rapid decrease of T_c has been reported in a systematic study of the electronic and structural properties of single crystals of $Sr_{0.065}Bi_2Se_3$ [162]. In the pressure range covering p_c the $R\bar{3}m$ space group is preserved. By increasing the pressure further two structural phase transitions are observed, namely at 6 GPa to the $C2/m$ phase and at 25 GPa to the I4/mmm phase. We remark that at pressures above 6 GPa superconductivity reemerges with a maximum $T_c \sim 8.3$ K [162]. This is analogous to the emergence of superconductivity under pressure in undoped Bi_2Se_3 [163].

6.2 Experimental

For the preparation of $Sr_xBi_2Se_3$ single crystals with a nominal value $x = 0.15$, high-purity elements were melted at 850 °C in sealed evacuated quartz tubes. Crystals were formed by slowly cooling to 650 °C at a rate of 3 °C/hour. Powder X-ray diffraction confirmed the R$\bar{3}$m space group. The single-crystalline nature of the crystals was checked by Laue back-reflection. Flat samples with typical dimensions $0.3 \times 2.5 \times 3$ mm^3 were cut from the bulk crystal with a scalpel blade. The plane of

the samples contains the a- and a^*-axis. The a-direction was taken along the long direction of the sample. The characterization of the single-crystalline batch with $x = 0.15$ by means of X-ray diffraction, transport and ac-susceptibility measurements is presented in the Supplementary Information of Ref. [42]. The characterization presented in Ref. [42] is representative for the crystals studied here, among others a superconducting shielding fraction of 80 %.

High-pressure magnetotransport measurements were carried out with help of a hybrid clamp cell made of NiCrAl and CuBe alloys. Two crystals were mounted on a plug that was placed in a Teflon cylinder with Daphne oil 7373 as a hydrostatic pressure transmitting medium. For resistance measurements in a four-point configuration thin gold wires were attached to the flat sides of the crystals by silver paste. The magnetic field was applied in the aa^*-plane of the sample with configurations $B \parallel a \parallel I$ (crystal 1) and $B \parallel a^* \perp I$ (crystal 2). In these geometries B_{c2} attains its maximum and minimum value, respectively [42]. The pressure cell was attached to the cold plate of a ^{3}He refrigerator (Heliox, Oxford Instruments) equipped with a superconducting solenoid ($B_{max} = 14$ T). The effective pressure was determined in previous experiments [40, 46] and the maximum pressure reached is 2.2 GPa. Low temperature, $T = 0.24 - 10$ K, resistance measurements were performed using a low-frequency lock-in technique with low excitation currents ($I \leq 100\ \mu$A).

6.3 Results

Before mounting the crystals in the pressure cell the temperature variation of the resistivity was measured at ambient pressure. The resistivity shows a metallic behavior and levels off below $\sim$ 10 K [42]. For both crystals $T_c = 3.05 \pm 0.10$ K as identified by the midpoints of the transitions in $R(T)$ (see black solid circles in Fig. 6.1). Under pressure the resistivity remains metallic and the resistance ratio $R(300\text{K})/R(4\text{K})$ increases by $\sim$ 100 % for crystal 1 and $\sim$ 30 % for crystal 2, as shown in the inset of Fig. 6.2. The larger increase for crystal 1 is mainly due to the decrease of $R(4\text{K})$, while $R(4\text{K})$ is close to constant for crystal 2. $R(T)$ around the superconducting transition under pressure is shown in Fig. 6.1 (solid lines). Superconductivity progressively shifts to lower temperatures. In Fig. 6.2 we trace $T_c(p)$ of both crystals. T_c is smoothly depressed to a value of 0.90 K at 2.15 GPa. The dashed line in Fig. 6.2 represents a linear extrapolation of $T_c(p)$ and indicates the critical

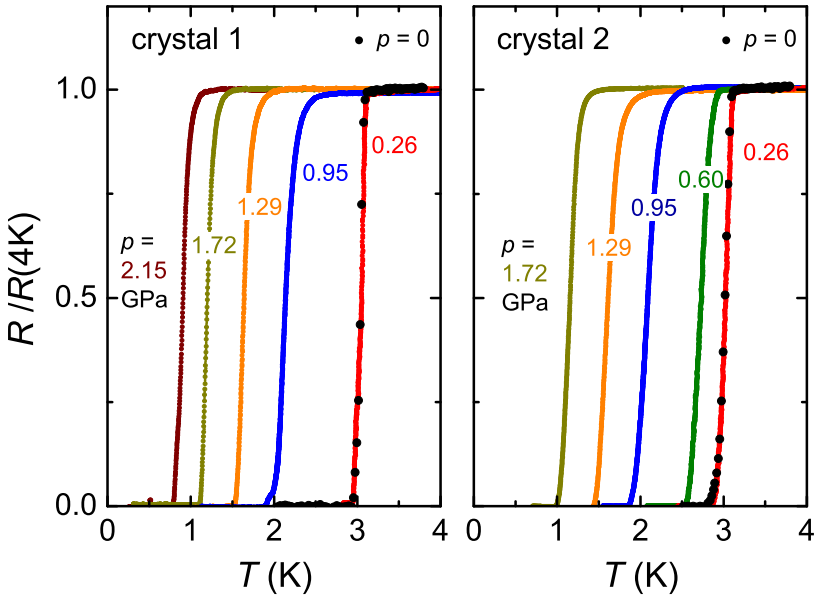

Figure 6.1: Resistance of $Sr_{0.15}Bi_2Se_3$ as a function of temperature around T_c for crystal 1 (left panel) and crystal 2 (right panel) at pressures up to 2.15 GPa as indicated. The resistance is normalized to $R(4\text{K})$ at ambient pressure. The black solid circles represent $R(T)$ at ambient pressure.

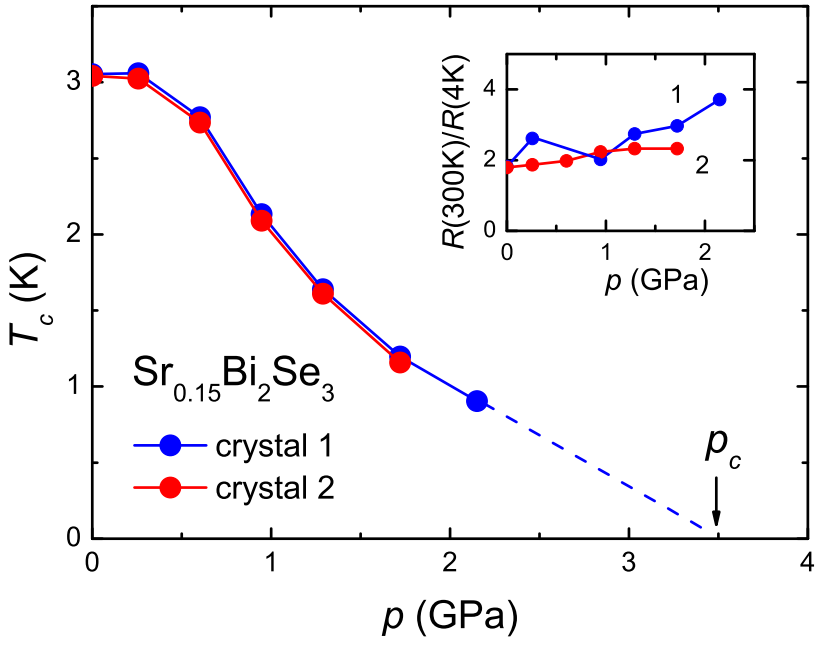

Figure 6.2: Superconducting transition temperature T_c as a function of pressure for crystal 1 (blue symbols) and crystal 2 (red symbols). The dashed line represents a linear extrapolation of $T_c(p)$ with $p_c \sim 3.5$ GPa. Inset: Normalized resistance $R(300\text{K})/R(4\text{K})$ as a function of pressure for both crystals.

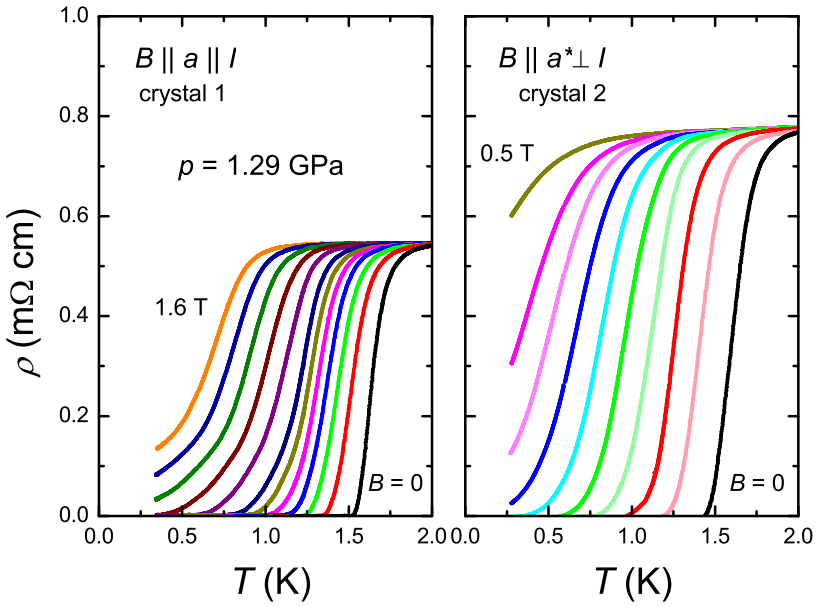

Figure 6.3: Left panel: Resistivity of $Sr_{0.15}Bi_2Se_3$ as a function of temperature at $p = 1.29$ GPa for $B \parallel a \parallel I$ (crystal 1) measured in fixed magnetic fields. Curves from right to left: from 0 T to 0.6 T with 0.1 T steps and from 0.8 T to 1.6 T with 0.2 T steps. Right panel: Data for $B \parallel a^* \perp I$ (crystal 2) measured in fixed magnetic fields. Curves from right to left: from 0 T to 0.4 T with 0.05 T steps and in 0.5 T.

pressure p_c for the suppression of superconductivity is ~ 3.5 GPa. We remark that the value $p_c = 1.1$ GPa reported in Ref. [162] most likely underestimates p_c as it is based on the extrapolation of $T_c(p)$ from temperatures above 2 K only. In the case of $Cu_xBi_2Se_3$ the critical pressure is estimated to be a factor 2 larger than in the Sr doped case, $p_c \sim 6.3$ GPa [40].

The resistance as a function of temperature in fixed magnetic fields applied along the a- and a^*-axis was measured to determine the upper-critical field, B_{c2}. Typical data at $p = 1.29$ GPa are presented in Fig. 6.3. The superconducting transition becomes broader in magnetic field. In order to systematically determine $T_c(B)$ (or $B_{c2}(T)$) we collected the midpoints of the superconducting transitions in $R(T)$. We remark that other definitions of T_c, such as a 10% or 90% drop of the resistance with respect to the normal state value, will affect the absolute value of B_{c2}, but not our central conclusion that the anisotropy of B_{c2} is robust under pressure.

The main results are presented in Fig. 6.4, where we have plotted $B_{c2}(T)$ at different pressures for $B \parallel a$ (crystal 1) and $B \parallel a^*$ (crystal 2). Note the difference of a factor 2 in the units along the vertical axis between the left and right panel. The

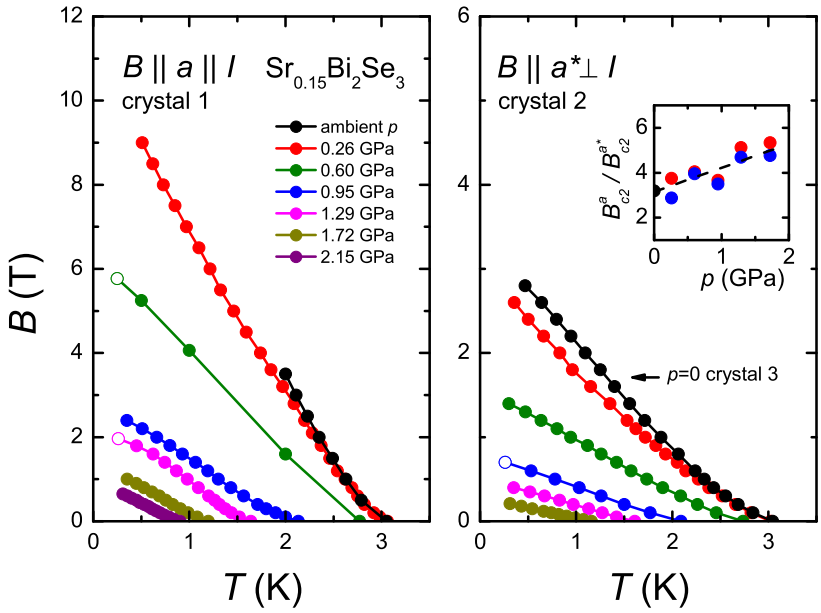

Figure 6.4: Temperature variation of the upper-critical field, B_{c2}, of $Sr_{0.15}Bi_2Se_3$ with configuration $B \parallel a \parallel I$ (left panel) and $B \parallel a^* \perp I$ (right panel) at pressures (from top to bottom) of 0, 0.26, 0.60, 0.95, 1.29, 1.72 and 2.15 GPa. Open circles yield B_{c2} taken from field sweeps at fixed temperature. The data at $p = 0$ (crystal 3) in the right panel are taken from Ref. [42]. Inset: Pressure variation of the basal-plane anisotropy $B^a_{c2}/B^{a^*}_{c2}$ at $T = 0.5$ K (solid red symbols) and at $T/T_c = 0.28$ (solid blue symbols). The ambient pressure point is taken from Ref. [42]. The dashed line is a guide to the eye.

most striking feature is the strong depression of $B^a_{c2}(T)$ and $B^{a^*}_{c2}(T)$ with pressure. A second remarkable feature is that the strong anisotropy $B^a_{c2}(T) \gg B^{a^*}_{c2}(T)$ persists under pressure.

6.4 Analysis and discussion

The robustness of the large basal-plane anisotropy can be quantified by tracing the ratio $B^a_{c2}/B^{a^*}_{c2}$ at the low temperature of 0.5 K as a function of pressure (see inset in Fig. 6.4). This shows the anisotropy ratio is reinforced under pressure and increases by a factor close to 2 at the highest pressure (2.2 GPa). Since $B_{c2}(T)$ does not level off when $T \to 0$, we have also traced the anisotropy ratio at the reduced temperature $T/T_c = 0.28$ in the inset. The increase is the same. The configurations $B \parallel a \parallel I$ (crystal 1) and $B \parallel a^* \perp I$ (crystal 2) were selected because at these field angles the

maximum and minimum B_{c2} values are measured. The large anisotropy $B^a_{c2}/B^{a^*}_{c2}$ tells us the rotational symmetry breaking is preserved. Since we cannot rotate the pressure cell in the magnetic field *in-situ*, the development of additional anisotropy terms cannot be ruled out. This is however highly unlikely given the smooth variation of $B^a_{c2}(p)$ and $B^{a^*}_{c2}(p)$.

As discussed in Pan *et al*. [42] the large two-fold basal-plane anisotropy cannot be explained by the Ginzburg-Landau anisotropic effective mass model or by the effect of flux flow on B_{c2} due to the Lorentz force for $B \perp I$. Instead it provides solid evidence for unconventional superconductivity. This was put on firm footing by calculations of the upper-critical field in the framework of the Ginzburg-Landau theory for superconductors with D_{3d} crystal symmetry [164, 105]. While for one-dimensional representations B_{c2} is isotropic in the basal plane, two-dimensional representations, like E_u, can give rise to a six-fold anisotropy. The further reduction of B_{c2} to two-fold as observed in experiments [41, 111, 42, 161] is then naturally explained by the lifting of the degeneracy of the two components. The origin of the lifting of the degeneracy has not been established yet, and is the subject of future research. Possibly, uniaxial strain or a preferred ordering of the dopant atoms in the Van der Waals gaps between the quintuple layers of the Bi_2Se_3 crystal, lowers the symmetry.

The increase of the ratio $B^a_{c2}/B^{a^*}_{c2}$ with pressure is somewhat unexpected, since hydrostatic pressure has a tendency to broaden phenomena. According to the basic Ginzburg-Landau relations, $B^a_{c2} = \Phi_0/(2\pi\xi_{a^*}\xi_c)$ and $B^{a^*}_{c2} = \Phi_0/(2\pi\xi_a\xi_c)$, where ξ is the superconducting coherence length and Φ_0 the flux quantum, it implies ξ_a/ξ_{a^*} increases with pressure. Interpreting ξ as the Cooper-pair size this tells us the pairing interaction along a^* increases (ξ_{a^*} smaller) with respect to that along a and in a simple model that the superconducting gap becomes more anisotropic. Here we use the BCS relation $\xi = \hbar v_F/\pi\Delta$, where Δ is the superconducting gap and v_F the Fermi velocity. This in turn implies that in the Ginzburg-Landau theory of B_{c2} in the D_{3d} crystal point group the coupling constant g of the symmetry breaking term and (or) the ratio J_4/J_1 of the gradient coefficients increase(s) [105].

We remark that both B^a_{c2} and $B^{a^*}_{c2}$ show an unusual temperature variation, notably at low pressures a pronounced upward curvature below T_c is followed by a quasilinear behavior. In an attempt to model $B_{c2}(T)$ we present the data in Fig. 6.5 in a reduced plot $b^*(t)$, with $b^* = -(B_{c2}(T)/T_c)/(dB_{c2}/dT)|_{T_c}$ and $t = T/T_c$ the reduced temperature. In calculating the slope $(dB_{c2}/dT)|_{T_c}$ we have neglected the

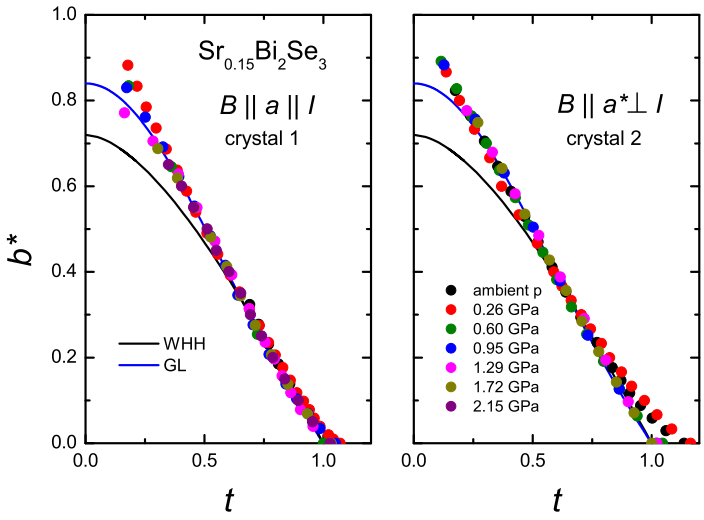

Figure 6.5: Reduced plot $b^*(t)$ of the upper-critical field, with $b^* = -(B_{c2}(T)/T_c)/(dB_{c2}/dT)|_{T_c}$ and $t = T/T_c$ at pressures of 0, 0.26, 0.60, 0.95, 1.29, 1.72 and 2.15 GPa for $B \parallel a^* \perp I$ (left panel) and $B \parallel a^* \perp I$ (right panel). The black solid line represents a comparison with the WHH model for a weak-coupling spin-singlet superconductor and the blue solid line represents the generalized Ginzburg-Landau model (see text). In the determination of the slope $(dB_{c2}/dT)|_{T_c}$ and T_c the low-field curvature of B_{c2} is neglected.

low-field curvature which resulted in a lower T_c. Therefore the reduced data show a tail that extends to $t > 1$. Apart from the low-field curvature that weakens under pressure, the data overall collapse onto a single function $b^*(t)$, as reported, for instance, for $Cu_xBi_2Se_3$ [40] and the half-Heusler superconductor YPtBi [46]. This shows the functional dependence does not change under pressure. For comparison we have plotted in Fig. 6.5 the B_{c2}-curve for a standard weak-coupling BCS spin-singlet superconductor with orbital limit $B_{c2}^{orb}(0) = -0.72 \times T_c(dB_{c2}/dT)|_{T_c}$, i.e. the Werthamer-Helfand-Hohenberg (WHH) model curve [77]. Clearly, the data deviate strongly from the model curve. This calls for detailed theoretical work to model $B_{c2}(T)$ in the case of Δ_4-pairing in the E_u representation. Finally, we remark that the phenomenological Ginzburg-Landau model curve, $B_{c2}(T) = B_{c2}(0)[(1-t^2)/(1+t^2)]$, that was used in Ref. [165] to provide an estimate of $B_{c2}(0)$, yields a description of the collapsed data over fairly large temperature range as shown in Fig. 6.5, where we used $b^*(0) = 0.84$.

6.5 Conclusions

We have carried out a high-pressure study of the unconventional superconductor $Sr_{0.15}Bi_2Se_3$ in order to investigate the unusual basal-plane anisotropy of the upper-critical field, recently detected at ambient pressure [42]. The superconducting transition temperature is rapidly depressed with a critical pressure of $\sim$ 3.5 GPa. $B_{c2}(T)$ has been determined for the B-field applied along two orthogonal directions, a and a^*, in the basal plane. The pronounced two-fold basal-plane anisotropy $B^a_{c2}/B^{a^*}_{c2} = 3.2$ at $T = 0.3$ K is robust under pressure and attains a value of $\sim$ 5 at the highest pressure (2.2 GPa). The two-fold anisotropy of $B_{c2}(T)$ provides solid evidence for rotational symmetry breaking in the D_{3d} crystal structure. This puts stringent conditions on the superconducting order parameter, namely it should belong to a two-dimensional representation (E_u). Rotational symmetry breaking seems to be ubiquitous in the family of doped Bi_2Se_3-based superconductors. This offers an exciting opportunity to study unconventional superconductivity with a two-component order parameter.

Chapter 7

Magnetic and superconducting phase diagram of the half-Heusler topological semimetal HoPdBi

We report a study of the magnetic and electronic properties of the non-centrosymmetric half-Heusler antiferromagnet HoPdBi ($T_N = 2.0$ K). Magnetotransport measurements show HoPdBi has a semimetallic behaviour with a carrier concentration $n = 3.7 \times 10^{18}$ cm^{-3} extracted from the Shubnikov-de Haas effect. The magnetic phase diagram in the field-temperature plane has been determined by transport, magnetization and thermal expansion measurements: magnetic order is suppressed at $B_M \sim 3.6$ T for $T \to 0$. Superconductivity with $T_c \sim 1.9$ K is found in the antiferromagnetic phase. Ac-susceptibility measurements provide solid evidence for bulk superconductivity below $T_c = 0.75$ K with a screening signal close to a volume fraction of 100 %. The upper-critical field shows an unusual linear temperature variation with $B_{c2}(T \to 0) = 1.1$ T. We also report electronic structure calculations that classify HoPdBi as a new topological semimetal, with a non-trivial band inversion of 0.25 eV.

This chapter has been published as Nikitin *et al.*, J. Phys.: Condens. Matter **27**, 275701 (2015)

7.1 Introduction

The compound HoPdBi is member of the large family of half-Heuslers that crystallize in the non-centrosymmetric space group $F\bar{4}3m$ [166]. Ternary Heuslers with composition 2:1:1 and half Heuslers with composition 1:1:1 attract ample attention because of their flexible electronic structure, which gives rise to applications as multifunctional materials in, for example, the fields of spintronics and thermoelectricity [167]. Recently, a new incentive to investigate half-Heusler compounds was provided by first principles calculations [97, 96, 168]. By employing the hybridization strength and the magnitude of the spin-orbit coupling it was established that “heavy-element" half-Heusler compounds may show a non-trivial band inversion, similar to the prototypical topological insulator HgTe [169, 151, 152]. Topological half-Heuslers are zero-gap semiconductors, where the topological surface states can be created by applying strain that opens the gap. The emergence of magnetic order and superconductivity at low temperatures in half-Heuslers provides a new research direction to study the interplay of topological states, superconductivity and magnetic order [48].

Recently, much research has been devoted to the band-inverted half-Heusler platinum and palladium bismuthides, notably because some of these superconduct at low temperatures [170]: LaPtBi ($T_c = 0.9$ K [44]), YPtBi ($T_c = 0.77$ K [45, 46]), LuPtBi ($T_c = 1.0$ K [47]) and LuPdBi ($T_c = 1.7$ K [49, 52]). The s-p inverted band order ($\Gamma_8 > \Gamma_6$) makes these compounds candidates for topological superconductivity [171, 172]. Topological superconductors are predicted to be unconventional superconductors, with an admixture of even- and odd-parity Cooper pair states in the bulk, and protected Majorana states at the surface [151, 152]. Since the crystal structure lacks inversion symmetry these superconductors might also be classified as non-centrosymmetric. Here theory predicts a mixed even- and odd-parity Cooper pair state [173] as well.

Recently, we reported the observation of superconductivity ($T_c = 1.22$ K) and antiferromagnetic order ($T_N = 1.06$ K) in the half-Heusler ErPdBi [48]. In addition, electronic structure calculations predicted a sizeable band inversion, which makes ErPdBi a first candidate for the investigation of the interplay of topological states, superconductivity and magnetic order. Another candidate proposed is CePdBi ($T_c = 1.3$ K, $T_N = 2.0$ K), however, here superconductivity develops in small part of the sample and is associated with a disordered phase [174]. The coexistence

of superconductivity and magnetic order in ErPdBi provided a strong motivation to search for similar phenomena in other REPdBi compounds (RE = Rare Earth), such as HoPdBi [166, 175]. HoPdBi was reported to be an antiferromagnet with a Néel temperature $T_N = 2.2$ K [175]. Its magnetic susceptibility follows a Curie-Weiss law with an effective moment $\mu_{\text{eff}} = 10.6\ \mu_B$, in good agreement with the theoretical value for free RE^{3+} ions with Russell-Saunders coupling ($J = 8$). The weak antiferromagnetic coupling is furthermore inferred from the low value of the Curie-Weiss constant $\Theta_P = -6.4$ K. Here we report results of transport, magnetic and thermal measurements on single crystalline HoPdBi. Our flux-grown crystals show antiferromagnetic order at $T_N = 2.0$ K and superconductivity at $T_c \sim 1.9$ K. However, the transition to bulk superconductivity, inferred from the full diamagnetic screening signal (100 % volume fraction), sets in near $T_c^{bulk} \sim 0.75$ K. We report the magnetic and superconducting phase diagram in the field-temperature plane, as well as electronic structure calculations that reveal a non-trivial band inversion of 0.25 eV at the Γ-point. In the course of our investigations, Nakajima *et al*. [51] reported that superconductivity occurs in almost the entire antiferromagnetic REPdBi series, with $T_c \sim 1$ K for HoPdBi.

7.2 Methods

Several single crystalline batches of HoPdBi were prepared using Bi flux. The high purity elements Ho, Pd and Bi (purity 3N5, 4N and 5N, respectively) served as starting material. First an ingot of HoPdBi was prepared by arc-melting and placed in an alumina crucible with excess Bi flux. The crucible was sealed in a quartz tube under a high-purity argon atmosphere (0.3 bar). Next the tube with the crucible was heated in a furnace to 1150 °C and kept at this temperature for 36 h. Then the tube was slowly cooled to 500 °C at a rate of 3 °C per hour to form the crystals. The single-crystalline nature of the crystals was checked by Laue backscattering. After cutting the crystals in suitable shapes for the various experiments, the surfaces were cleaned by polishing. Powder X-ray diffraction confirmed the $F\bar{4}3m$ space group and the extracted lattice parameter, $a = 6.605$ Å, is in good agreement with the literature [166]. Several tiny extra diffraction lines point to the presence of a small amount of an impurity phase (< 5 %). These lines could not be matched to potential inclusions or impurity phases, such as Bi, PdBi, α-Bi_2Pd and β-Bi_2Pd. The results

presented here are taken on samples that all come from the same single-crystalline batch. The measured samples are labeled #2-#4, and show very similar magnetic and superconducting properties.

Magnetic and transport measurements were carried out in a Physical Property Measurements System (PPMS, Quantum Design) in the temperature range 1.8-300 K. The magnetization and susceptibility were measured utilizing a Vibrating Sample Magnetometer, while the resistance and Hall effect were measured using a standard four-point low-frequency ac-technique with an excitation current of 1 mA. The specific heat was measured down to 2.0 K on a crystal with a mass of 10 mg in the PPMS as well. Low temperature, $T = 0.24 - 10$ K, resistance and ac-susceptibility measurements were made in a ^{3}He refrigerator (Heliox, Oxford Instruments) using a low-frequency lock-in technique with low excitation currents ($I \leq 200\ \mu$A). The coefficient of linear thermal expansion, $\alpha = \mathrm{L}^{-1}(\mathrm{dL/dT})$, with L the sample length, was measured using a three-terminal parallel-plate capacitance method using a home-built sensitive dilatometer based on the design reported in Ref. [117]. Magnetoresistance data were taken in a dilution refrigerator (Kelvinox, Oxford Instruments) for $T = 0.03 - 1$ K and high magnetic fields up to 17 T. Additional low-temperature dc-magnetization and ac-susceptibility measurements were made using a SQUID magnetometer, equipped with a miniature dilution refrigerator, developed at the Néel Institute.

7.3 Results and analysis

7.3.1 Superconductivity

In Fig. 7.1 we show the resistivity $\rho(T)$ of a single crystal of HoPdBi (sample #2). The resistivity values are rather large and $\rho(T)$ has a broad maximum around 80 K. The charge carrier concentration n_h extracted from the low field ($B < 2$ T) Hall effect measurements is traced in the inset of Fig. 7.1. The carriers are holes and at the lowest temperature ($T = 2.0$ K) $n_h = 1.3 \times 10^{19}$ cm^{-3}. These transport parameters reveal semimetallic-like behaviour. At low temperatures, the resistivity drops to zero, which signals the superconducting transition.

The superconducting transition measured by resistivity in zero and applied magnetic fields is reported in detail in Fig. 7.2. The superconducting transition at $B = 0$ is fairly broad, with an onset temperature of 2.3 K and zero resistance at 1.6 K. By

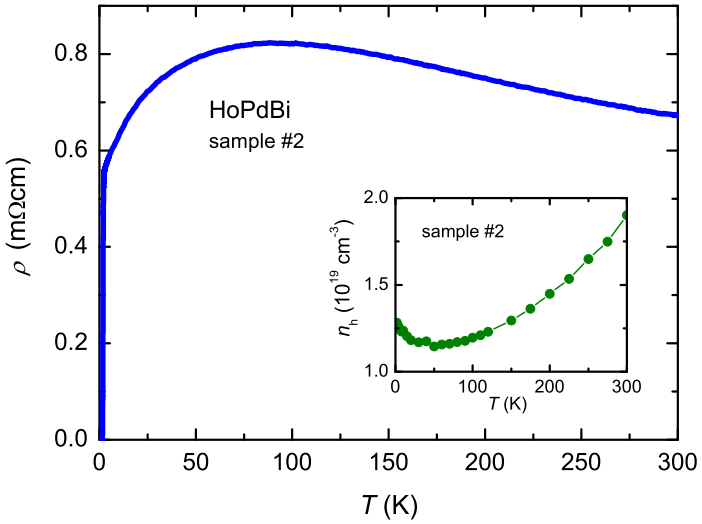

Figure 7.1: Resistivity and carrier concentration (inset) as a function of temperature of HoPdBi sample #2.

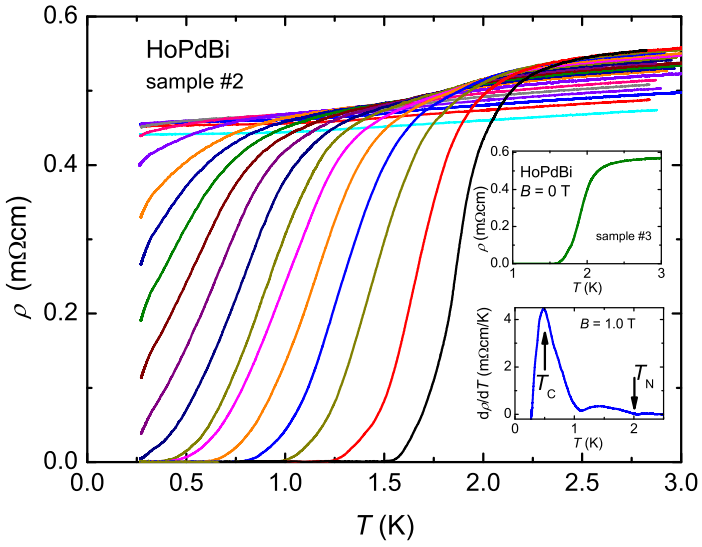

Figure 7.2: Resistivity as a function of temperature for HoPdBi sample #2 measured in fixed magnetic fields: from right to left 0 T to 1.1 T in steps of 0.1 T, 1.2 T to 2 T in steps of 0.2 T, and 2.25 T, 2.5 T and 3 T. Lower inset: Derivative $\mathrm{d}\rho/\mathrm{d}T$ *versus* T for $B = 1.0$ T; arrows indicate T_c and T_N. Upper inset: $\rho(T)$ *versus* T in zero field for sample #3.

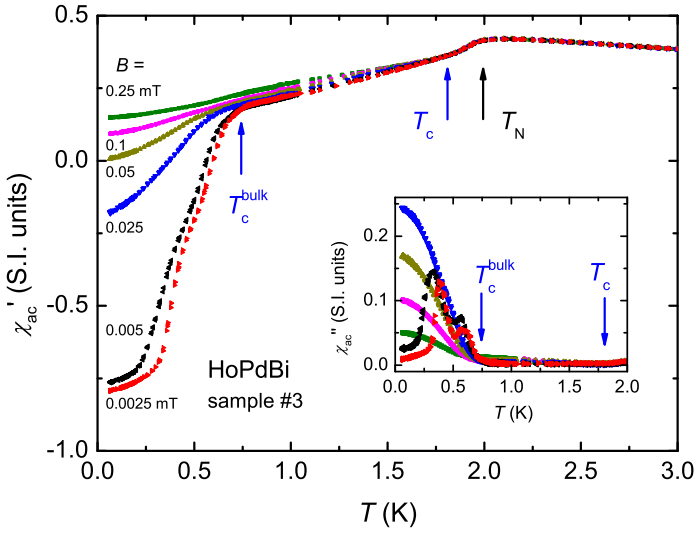

Figure 7.3: Real part of the ac-susceptibility of HoPdBi sample #3 for driving fields of 0.0025, 0.005, 0.025, 0.05, 0.10 and 0.25 mT, from bottom to top. Arrows indicate T_N, T_c and T_c^{bulk}. The inset shows the corresponding imaginary part of χ_{ac}.

tracing the maximum in the derivative $\mathrm{d}\rho/\mathrm{d}T$ we obtain T_c = 1.86 K. The broad transition is most likely related to the simultaneous development of antiferromagnetic order with $T_N = 2.0$ K (see below). A similar rounded $\rho(T)$ near the onset for superconductivity was observed for ErPdBi, where $T_c \simeq T_N$ as well [48]. We have determined the upper-critical field B_{c2} by taking $T_c(B)$ as the maximum in $\mathrm{d}\rho/\mathrm{d}T$ obtained in constant magnetic fields. See the lower inset of Fig. 7.2 for the data at $B = 1.0$ T. Here the structure at 2.0 K signals the antiferromagnetic transition. The temperature variation $B_{c2}(T)$ is reported in the phase diagram, Fig. 7.7. In the upper inset of Fig. 7.2 we show the zero-field data for sample #3. The resistivity data for this sample (data in field are not shown) are in good agreement with the results obtained for sample #2.

In Fig. 7.3 we show ac-susceptibility (χ_{ac}) data taken on sample #3 for different driving fields B_{ac} ranging from 0.0025 to 0.25 mT. Upon cooling $\chi_{ac}(T)$ first increases and has a pronounced maximum at 2.0 K, which locates the antiferromagnetic phase transition temperature. Upon further cooling a large superconducting signal appears below 0.75 K. For the smallest driving fields $B_{ac} \leq 0.05$ mT the screening fraction associated with this diamagnetic signal is ~ 90 %, which provides strong support for bulk superconductivity. Upon increasing the driving field to 0.25 mT

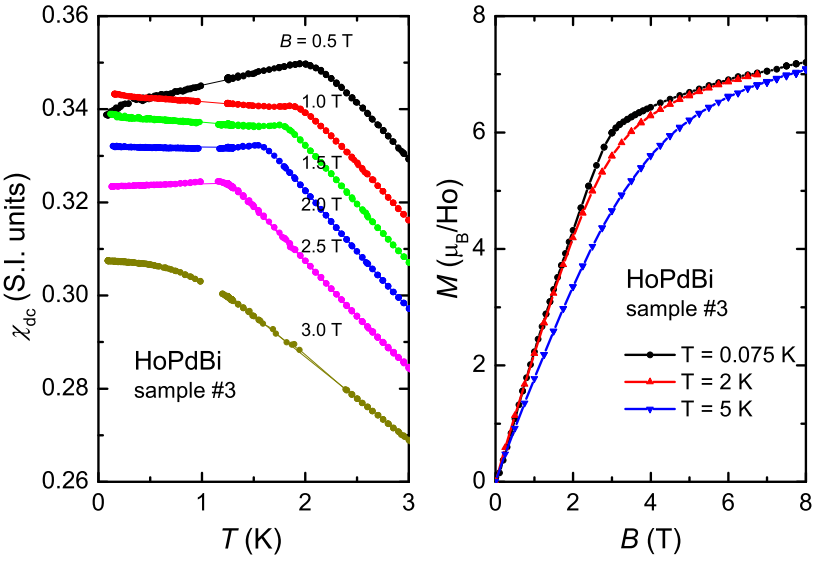

Figure 7.4: Left panel: Magnetic susceptibility of the HoPdBi sample #3 as a function of temperature measured in magnetic fields up to 3 T as indicated. Right panel: Magnetization in fields up to 8 T at temperatures of 0.075, 2.0 and 5.0 K.

the magnitude of the diamagnetic signal is rapidly depressed, which indicates the lower-critical field B_{c1} is very small. However, a close inspection of the data shows that a weaker diamagnetic signal develops near 1.8 K, which is close to midpoint of the superconducting transition at 1.9 K of sample #3 (see upper inset Fig. 7.2). The amplitude of the diamagnetic signal varies with B_{ac}. This clearly indicates a smaller volume fraction ($\sim$ 20 %) of the sample becomes superconducting at 1.8 K. Here we have neglected the demagnetization factor that we estimate to be $N = 0.07 \pm 0.02$ for our needle-shaped sample #3. We remark that after correcting for demagnetization effects the total superconducting volume fraction is close to $\sim$ 100 %. These observations are corroborated by the imaginary part of $\chi_{ac}(T)$ shown in the inset of Fig. 7.3. The transition to the bulk superconducting state reveals the presence of a remaining sample inhomogeneity, as indicated by the double peak structure in χ''_{ac} for small values $B_{ac} \leq 0.005$ mT.

7.3.2 Antiferromagnetic order

Magnetic susceptibility measurements carried out in a field of 0.1 T confirm local moment behaviour of the Ho moments. For $T > 50$ K Curie-Weiss behaviour is

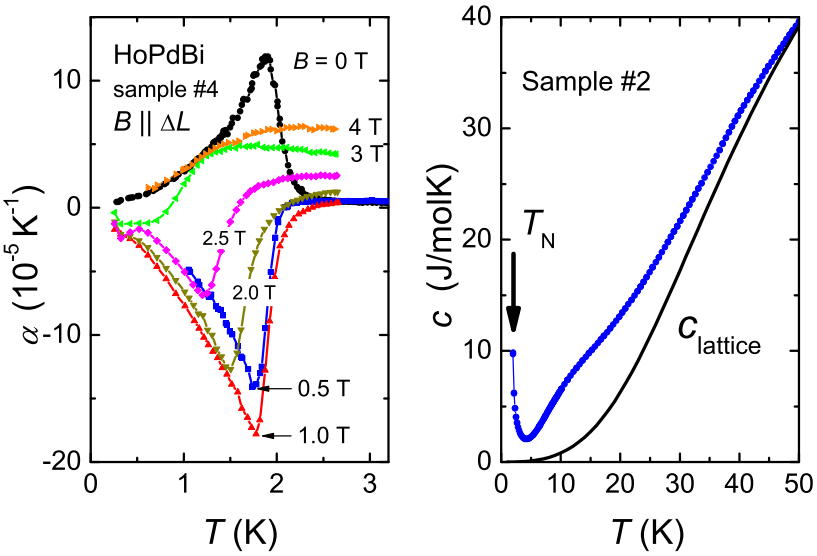

Figure 7.5: Left panel: Coefficient of linear thermal expansion as a function of temperature of HoPdBi (sample #4) measured in zero and applied fields as indicated. Right panel: Specific heat (sample #2) in a plot of c versus T up to 50 K. The solid line indicates the lattice contribution given by the Debye function with $\theta_D = 193$ K.

observed with an effective moment $\mu_{eff} = 10.3\ \mu_B$ and a negative Curie-Weiss constant $\Theta_P = -5.7$ K indicating the presence of antiferromagnetic interactions. These values are close to the ones reported in Ref. [175]. In Fig. 7.4 we show the dc-susceptibility around the antiferromagnetic transition measured in fields up to 3 T down to very low temperatures (0.1 K). The Néel temperature is progressively shifted with field and can no longer be discerned at the largest field. The variation $T_N(B)$ is traced in the phase diagram (Fig. 7.7). In the right panel we show the magnetization measured at $T = 0.075$ K, deep in the antiferromagnetic phase, and at 2 K and 5 K, measured along the (100) axis. At the lowest temperature the magnetization increases rapidly until it reaches a value of $\sim 6\ \mu_B$ at 3 T after which the increase is more gradual. In a field of 8 T the magnetization attains a value of 7.2 μ_B which is still considerably below the saturation value $m_s = gJ = 10\ \mu_B$ (here $g = 5/4$ is the Landé factor). An explanation for this is offered by the sizeable magnetic anisotropy associated with the Ho ions (see section 7.4). The presence of magnetocrystalline anisotropy can also be inferred from the very weak signature of a metamagnetic-like transition observed in $M(B)$ below T_N.

In Fig. 7.5 we show the coefficient of linear thermal expansion $\alpha(T)$ around the

antiferromagnetic transition. Upon cooling a large positive step $\Delta\alpha$ is observed, where the midpoint nicely agrees with T_N determined by the magnetic susceptibility. The superconducting transition is not observed in the thermal expansion because of the relatively small entropy involved (see the discussion section). In the right panel we show the specific heat measured in the temperature range 2 - 50 K. The increase at low temperatures upon approaching 2 K is due to the antiferromagnetic transition. When we compare $c(T)$ with the lattice specific heat, estimated by a Debye function with a Debye temperature $\theta_D = 193$ K, a broad magnetic contribution centered around 15 K becomes noticeable. This magnetic contribution with an entropy of $\sim 1.7 \times R$, where $R = 8.31$ J/molK is the gas constant, is most likely a Schottky contribution to the specific heat, associated with the partly lifting of the crystalline electric field ground state. In the cubic symmetry, the holmium $J = 8$ multiplet, with $2J + 1 = 17$ levels, may split into 1 singlet, 2 doublets and 4 triplets [176]. We remark that the magnetic susceptibility starts to deviate from the Curie-Weiss behaviour below 50 K as well. By combining the thermal expansion and specific heat data we can make an estimate of the pressure variation of T_N using the Ehrenfest relation $\mathrm{d}T_N/\,\mathrm{d}p = V_m\Delta\beta/(\Delta c/T_N)$. Here the coefficient of volume expansion $\beta = 3\alpha$ and $V_m = 4.3 \times 10^{-5}$ m^3/mol is the molar volume. Using the experimental values $\Delta\alpha = 1.2 \times 10^{-4}$ K^{-1} and $\Delta c/T_N \sim 5$ J/molK^2 we obtain $\mathrm{d}T_N/\,\mathrm{d}p \sim 0.3$ K/kbar. In an applied field, the longitudinal thermal expansion measured along the direction of the magnetic field, $\alpha_\parallel$, develops a pronounced minimum. The negative $\alpha_\parallel$ indicates a large magnetocrystalline anisotropy, with an expansion along the field and a contraction perpendicular to the field, upon cooling below T_N. Notice, in magnetic field $\beta = \alpha_\parallel + 2\alpha_\perp$. The variation $T_N(B)$ extracted from the thermal expansion is traced in the phase diagram Fig. 7.7.

7.3.3 Quantum oscillations

The magnetoresistance was measured in magnetic fields up to 17 T at low temperatures in the dilution refrigerator. A typical trace taken at $T = 0.05$ K is shown in Fig. 7.6. After the suppression of superconductivity, the kink at $B_M = 3.6$ T locates the antiferromagnetic phase boundary. In fields exceeding 8 T we observed Shubnikov-de Haas oscillations. Since the oscillatory component is rather small ($\Delta\rho/\rho \sim 0.1\%$) and superimposed on a non-monotonic background, it is difficult to extract the precise magnitude as a function of $1/B$. In the lower inset of Fig. 7.6 we

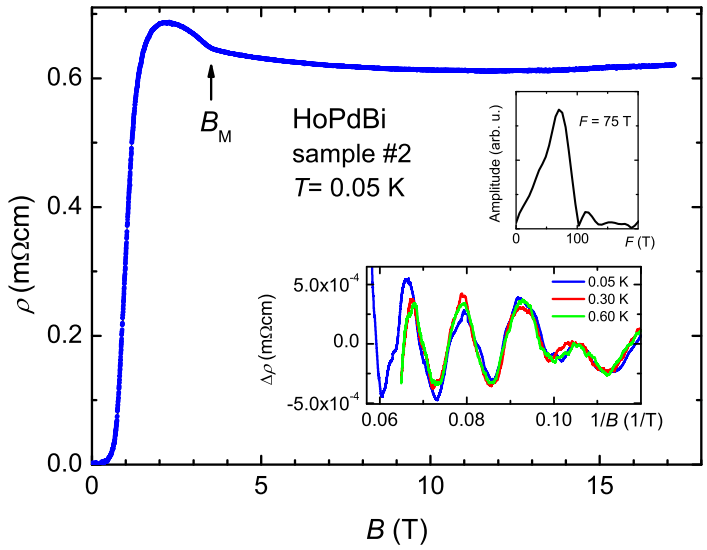

Figure 7.6: Resistance of the HoPdBi sample #2 as a function of the magnetic field at $T = 0.05$ K. The arrow indicates the antiferromagnetic phase boundary at B_M. Lower inset: $\Delta\rho$ as a function of $1/B$ showing the Shubnikov - de Haas effect at 0.05, 0.3 and 0.6 K. Upper inset: fast Fourier transform of the data with frequency $F = 75 \pm 5$ T.

trace the resulting oscillations in $\Delta\rho$ as a function of $1/B$. A fast Fourier transform (upper inset) shows the frequency is 75 ± 5 T. For a circular extremal cross section $A_k(E_F) = \pi k_F^2$ we calculate with help of the Onsager relation a Fermi wave vector $k_F = 4.8 \times 10^8$ m^{-1}. Assuming a spherical Fermi surface pocket, the corresponding 3D carrier density $n = k_F^3/3\pi^2 = 3.7 \times 10^{18}$ m^3 which is a factor ~ 3.5 smaller than the value deduced from the Hall effect measurements. Additional measurements at $T = 0.3$ and 0.6 K show the thermal damping is very weak, which points to an effective mass much smaller than the free electron mass, $m_{eff} < 0.5 m_e$, as reported for other topological semimetals [45, 44].

7.3.4 Phase diagram

In Fig. 7.7 we present the magnetic and superconducting phase diagram of HoPdBi. The upper-critical field B_{c2} shows a smooth variation with temperature and extrapolates to the value of 1.1 T at $T = 0$. This tells us $B_{c2}(T)$ is associated with the superconducting transition observed at 1.9 K in zero field. When we compare the B_{c2}-data to the Werthamer-Helfand-Hohenberg (WHH) curve for a weak-coupling

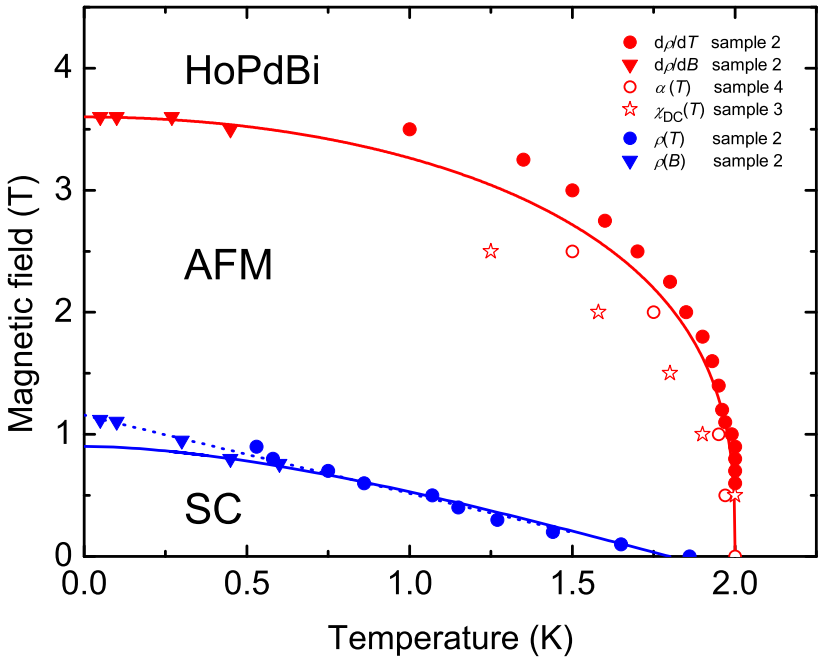

Figure 7.7: Magnetic and superconducting phase diagram of HoPdBi. Data points for the superconducting (SC) transition are taken on sample #2 where $T_c(B)$ is defined by the temperature of the maximum in $\mathrm{d}\rho/\mathrm{d}T$ at fixed fields (blue circles) or the maximum in $\mathrm{d}\rho/\mathrm{d}B$ at fixed temperatures (blue triangles). The blue solid line is a comparison of the $B_{c2}(T)$ data with the WHH model (see text). The blue dashed line represents a linear fit to the data. Data points for the antiferromagnetic (AFM) transition are taken from the resistivity (sample #2: red circles and triangles from $\mathrm{d}\rho/\mathrm{d}T$ and $\mathrm{d}\rho/\mathrm{d}B$, respectively), the magnetization (sample #3: open stars) and thermal expansion (sample #4: open circles). The red solid line represents a phenomenological order parameter fit with $T_N = 2.0$ K and $B_M = 3.6$ T at $T = 0$ (see text)

.

spin-singlet orbital-limited superconductor, some departure appears below ~ 0.7 K. We remark this is close to the temperature below which the diamagnetic screening signal shows the sudden increase towards bulk superconductivity (see Fig. 7.2). In the WHH model the clean-limit zero-temperature orbital critical field can be calculated from the relation $B_{c2}^{orb}(0) = 0.72 \times T_c |\mathrm{d}B_{c2}/\mathrm{d}T|_{T_c}$ and attains a value of 0.9 T (in the dirty limit the coefficient 0.72 is replaced by 0.69). From the experimental value $B_{c2}(0) = 1.1$ T we calculate, utilizing the relation $B_{c2} = \Phi_0/2\pi\xi^2$, where Φ_0 is the flux quantum, a superconducting coherence length $\xi = 17$ nm. A departure from the WHH model has also been observed for ErPdBi [48] and notably for YPtBi [45, 46], where is was taken as a strong indication of an odd-parity component in the superconducting order parameter. We remark, the superconducting phase is completely embedded in the antiferromagnetic phase.

The antiferromagnetic phase boundary has been determined by resistivity, magnetization and thermal expansion measurements, see Fig. 7.7. After an initial ($B <$ 1 T) steep increase with field, T_N smoothly decreases, and the antiferromagnetic phase transition is suppressed at $B_M(0) = 3.6$ T. Values for T_N extracted from the magnetization and thermal expansion are somewhat lower than the values obtained by transport, but all three experiments track the same phase boundary. These differences might be partly attributed to different orientations of the crystals in the magnetic field in connection to the large magnetic anisotropy. For the magnetization experiments the magnetic field was applied along (100), while for the other experiments the field was applied along an arbitrary crystal direction. In the figure we compare the phase boundary with the phenomenological order parameter function $B_M(T) = B_M(0)(1 - (T/T_N)^\alpha)^\beta$ with $T_N = 2.0$ K, $B_M(0) = 3.6$ T, $\alpha = 2$ and $\beta = 0.34$. The latter value is close to the theoretical value $\beta = 0.38$ expected for a 3D Heisenberg antiferromagnet [177].

7.3.5 Electronic structure

To understand the electronic properties, we have performed *ab initio* band structure calculations [178] based on the density-functional theory. The core electrons are represented by the projector-augmented-wave potential. We keep only three valence electrons of Ho (equivalent to La) and freeze all other f electrons as core electrons, to simplify the understanding of the topology. The calculated bulk band structure of HoPdBi exhibits a zero-gap, and is quite similar to that of ErPdBi [48] and other half-

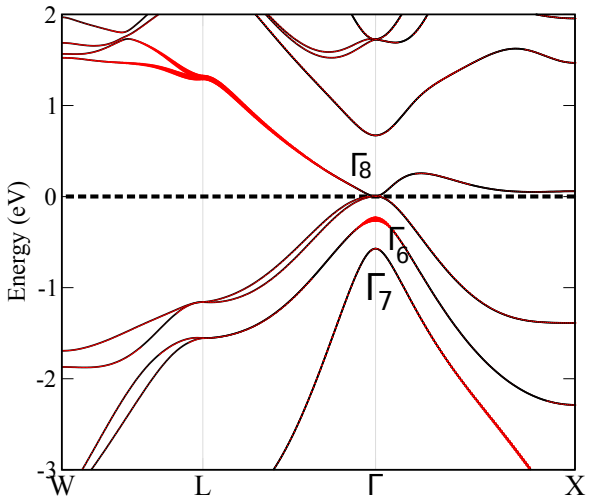

Figure 7.8: Calculated bulk band structure of the half-Heusler HoPdBi. The projection of the Pd-s states is highlighted by the thickness of the solid red lines. Bands $\Gamma_{6,7,8}$ are labeled according to the symmetry of their wave functions. The Fermi energy, E_F, is shifted to zero (horizontal dashed line). The measured sample is slightly p-doped, which will cause E_F to lie marginally below zero.

Heusler topological semimetals [97, 96]. The Γ_6 band (contributed by Pd-s states) is below the Γ_8 bands, showing the hall mark of band inversion. Therefore, we can clearly conclude that HoPdBi is also a topological semimetal. The effect of magnetization of Ho-f states is expected to possibly split the spin degeneracy slightly, but to preserve the inverted band order because the band inversion strength (the energy difference between Γ_8 and Γ_6 bands) is as large as 0.25 eV. The measured sample is slightly p-doped, which will cause E_F to lie marginally below zero.

7.4 Discussion

Our systematic transport, magnetic and thermal properties study demonstrates that HoPdBi combines local moment magnetism and superconductivity and thus behaves very similar to the related half-Heusler compound ErPdBi [48]. Superconductivity occurs at $T_c = 1.9$ K as determined by the resistive transition and the onset in χ_{ac}, however, the transition to a full diamagnetic screening fraction sets in

at a lower temperature, near 0.75 K. These results are in line with the recent work by Nakajima *et al*. [51], but nevertheless there are some noticeable differences: the midpoint of the resistive transition is at $\sim$ 1.0 K, and the onset of the diamagnetic signal is at $\sim$ 0.9 K [51]. Moreover, the transition measured by χ_{ac} [51] is very broad and extends to the lowest temperature measured ($\sim$ 0.1 K). A comparison of both studies suggests the superconducting phase transition found below $\sim$ 0.9 K by Nakajima *et al*. [51] is to be associated with the transition to the bulk superconducting state at 0.75 K as reported in fig. 2. The presence of a small volume fraction of our sample that superconducts at 1.9 K remains a puzzling aspect. A possible explanation is the presence of an impurity phase. Among the binary Bi-Pd alloys α-Bi_2Pd is reported to superconduct at 1.7 K [179]. However, the few extra tiny lines in the diffraction pattern could not be matched to the structure of α-Bi_2Pd. Moreover, $B_{c2}(0)$ of α-Bi_2Pd is small [51], which is at variance with the measured value $B_{c2}(0) = 1.1$ T.

A second, appealing explanation for superconductivity at 1.9 K is the occurrence of surface superconductivity associated with the topological surface states. Surface superconductivity at temperatures higher than the bulk T_c was recently proposed by Kapitulnik *et al.* [180, 181] for the topological half-Heuslers YPtBi and LuPtBi. Experimental evidence for this was provided by (surface sensitive) Scanning Tunneling Spectroscopy measurements. Surface superconductivity may also offer an explanation for the "unknown impurity phase" with $T_c = 1.7$ K, *i.e*. above the bulk T_c of 1.2 K, reported for ErPdBi [48]. Interestingly, Nakajima *et al*. [51] claim that surface superconductivity with $T_c = 1.6$ K can be induced by heat treatments at 200 °C for all REPdBi. These results may open a new, fascinating research direction in the field of topological superconductivity. Future experiments have to be directed to disentangle surface and bulk superconductivity in order to put these ideas on a firmer footing.

Local-moment antiferromagnetic order has been detected for most members of the REPdBi series [182, 175, 48, 51], with T_N following the De Gennes scaling: $T_N \propto (g_J - 1)^2 J(J+1)$ with g_J the Landé factor (see *e.g.* [183]). The Neél temperature $T_N = 2.0$ K of our crystals is in between the values 2.2 K and 1.9 K reported in Refs. [175] and [51], respectively. The phase diagram (Fig. 7.7) shows that antiferromagnetic order entirely encloses the superconducting phase. Superconductivity is attributed to the Γ_8 hole states (see Fig. 7.8). Normally, conventional BCS spin-singlet superconductivity is suppressed by local-moment magnetism. However, in

HoPdBi the energy scales are comparable, since $T_c \cong T_N$. The large superconducting volume fraction inferred from the low temperature χ_{ac} and dc-magnetization measurements indicates that superconductivity and antiferromagnetic order coexist. Magnetic local-probe techniques, such as muon spin rotation/relaxation (μSR) and/or nuclear magnetic resonance (NMR) would be very helpful to verify the coexistence of both ordering phenomena on the microscopic scale. From recent neutron diffraction experiments [51] it was concluded that HoPdBi has a type-II antiferromagnetic structure: ferromagnetic planes couple antiferromagnetically with a propagation vector along the cube diagonal, $Q = (0.5, 0.5, 0.5)$. The magnetization curves (Fig. 7.4) and the thermal expansion in field (Fig. 7.5) reveal the magnetocrystalline anisotropy is rather strong. This offers the following scenario for the magnetization curves. When the field is increased along the (100) axis the spins progressively reorient towards the field, while still pointing along the (111) direction. Near the antiferromagnetic phase boundary the component of the spin along the (100) direction is $m_s/\sqrt{3}$ = 5.8 μ_B which is close to the experimental value. For fields above 3 T the spins are being pulled against the anisotropy field, which explains the reduced value with respect to $m_s = 10\ \mu_B$. Interestingly, theoretical work based on symmetry classifications predicts the type II antiferromagnetic structure in these half-Heuslers produces a new ground state: an antiferromagnetic topological insulator [184]. Recently, it was proposed that a first realization of this novel electronic state is found in the half-Heusler antiferromagnet GdPtBi ($T_N = 9$ K) [185].

The large contribution of antiferromagnetic order to the thermal properties (Fig. 7.5) hampers the detection of superconductivity in the thermal expansion and specific heat. An estimate for the step-size Δc in the specific heat at T_c can be calculated from the standard BCS relation $(\Delta c/T_c)/\gamma = 1.43$, where γ is the Sommerfeld coefficient. It appears that γ cannot reliably be deduced from the experimental data (see Fig. 7.5) because of the presence of the large magnetic contribution centered around 15 K. However, an estimate for γ can be obtained from the Shubnikov - de Haas data using the relation $\gamma = \pi^2 k_B^2 g(E_F)/3$, where $g(E_F) = m^* k_F/\hbar^2\pi^2$ is the density of states. With the parameters calculated in section 3.3 we obtain $\gamma < 0.1$ mJ/molK^2 and $\Delta c < 0.1$ mJ/K at T_c, which is very small indeed. An estimate for the step size in the thermal expansion coefficient, $\Delta\alpha$, at T_c can be obtained from the Ehrenfest relation $\mathrm{d}T_c/\mathrm{d}p = V_m 3\alpha/(\Delta c/T_c)$. Assuming a typical value for $\mathrm{d}T_c/\ \mathrm{d}p$ = 0.044 K/GPa [46] we calculate $\Delta\alpha$ at T_c is smaller than 4.5×10^{-11} K^{-1}, which is beyond the resolution of the dilatometer.

The occurrence of superconductivity in a Ho-based compound is uncommon. Rare examples are found among the Chevrel phases [186] and the heavy-rare earth cuprates [187] and pnictides [188]. Coexistence of superconductivity and antiferromagnetic order is found in the borocarbide $HoNi_2B_2C$ [189], but here $T_c = 10.5$ K and exceeds $T_N = 6.0$ K. An important new aspect in the REPdBi series is the non-centrosymmetric crystal structure and the topological nature of the electronic structure. This provides a new opportunity to investigate unconventional superconductivity, due to mixed even and odd parity Cooper pair states, and its interplay with long-range magnetic order.

7.5 Summary

We have investigated the transport, magnetic and thermal properties of the half-Heusler antiferromagnet HoPdBi. Electrical resistivity and ac-susceptibility data taken on flux-grown single crystals show superconductivity occurs below 1.9 K. We demonstrate HoPdBi is a bulk superconductor. However, the transition to bulk superconductivity, as indicated by a diamagnetic screening fraction close to 100 %, sets in at a lower temperature of 0.75 K. The Néel temperature T_N is 2.0 K as determined by thermal expansion and dc-magnetization measurements. The superconducting and magnetic phase diagram in the $B - T$ plane has been determined: superconductivity is confined to the antiferromagnetic phase. Electronic structure calculations show HoPdBi is a topological semimetal with a band inversion of 0.25 eV at the Γ-point. This is in-line with the semimetallic behaviour observed in the electrical resistivity and the low carrier concentration $n_h = 3.7 \times 10^{18}$ cm^{-3} extracted from the Shubnikov-de Haas effect. We conclude, HoPdBi belongs to the half-Heusler REPdBi series with a topological band structure and presents a new laboratory tool to study the interplay of antiferromagnetic order, superconductivity and topological quantum states [48, 51].

7.6 Further development

After the work above was published [50], another paper on HoPdBi appeared in the literature [104]. Pavlosiuk *et al.* [104] carried out magnetic, electrical and specific heat measurements that confirmed the coexistence of superconductivity at T_c =

0.7 K and antiferromagnetic order at T_N = 1.9 K. The specific heat shows a λ-shaped anomaly at T_N = 1.9 K that was attributed to the antiferromagnetic phase transition, but no contribution of the superconducting transition at T_c = 0.7 K was observed. The Crystal Electric Field scheme was derived by comparing the specific heat of HoPdBi to one of the non-magnetic isostructural compound LuPdBi [52]. For the ground state multiplet $^5I_8$ the Ho^{3+} ion splits into four magnetic triplets, two magnetic doublets and one non-magnetic singlet. The electronic ground-state was found to be the triplet $\Gamma_5^{(1)}$ with a first excited doublet-state $\Gamma_3^{(1)}$ located at Δ_1 = 22 K.

Neutron diffraction experiments confirmed the antiferromagnetic order (type II) with a (0.5, 0.5, 0.5) propagation vector. Shubnikov-de Haas oscillations were observed in the magnetoresistance measured at T = 2.5 K. The Fast Fourier Transform shows two frequencies: $F_1 = 78.5$ T and a shoulder near $F_2 = 144$ T. The frequency $F_1 = 78.5$ T is close to the value $F = 75$ T we reported above. This possibly indicates that the Fermi surface is more complex than can be concluded based on Fig. 7.8. The authors also claim the oscillations have a non-trivial Berry phase, which is in line with the topological nature of the material.

Bibliography

[1] H. Kamerlingh Ones, Leiden comm. **120b, 122b, 124c** (1911)

[2] V.L. Ginzburg, L.D. Landau, Zh. Eksp. Teor. Fiz. **20**, 1064 (1950)

[3] J. Bardeen, L.N. Cooper, J.R. Schrieffer, Phys. Rev. **108**, 1175 (1957)

[4] D.D. Osheroff, R.C. Richardson, D.M. Lee, Phys. Rev. Lett. **28**, 885 (1972)

[5] A.J. Leggett, Rev. Mod. Phys. **47**, 331 (1975)

[6] F. Steglich, J. Aarts, C.D. Bredl, W. Lieke, D. Meschede, W. Franz, H. Schafer, Phys. Rev. Lett. **43**, 1892 (1979)

[7] A. de Visser, J.J.M. Franse, A. Menovsky, T.T.M. Palstra, J. Phys. F: Met. Phys. **14**, L191 (1984)

[8] W. Schlabitz, J. Baumann, B. Pollit, U. Rauchschwalbe, H.M. Mayer, U. Ahlheim, C.D. Bredl, Z. Phys. B **62**, 171 (1986)

[9] R. Movshovich, T. Graf, D. Mandrus, J.D. Thompson, J.L. Smith, Z. Fisk, Phys. Rev. B **53**, 8241 (1996)

[10] N.D. Mathur, F.M. Grosche, S.R. Julian, I.R. Walker, D.M. Freye, R.K.W. Haselwimmer, G.G. Lonzarich, Nature **394**, 39 (1998)

[11] S.S. Saxena, P. Agarwal, K. Ahilan, F.M. Grosche, R.K.W. Haselwimmer, M.J. Steiner, E. Pugh, I.R. Walker, S.R. Julian, P. Monthoux, G.G. Lonzarich, A. Huxley, I. Sheikin, D. Braithwaite, J. Flouquet, Nature **406**, 587 (2000)

[12] D. Aoki, A. Huxley, E. Ressouche, D. Braithwaite, J. Flouquet, J.P. Brison, E. Lhotel, C. Paulsen, Nature **413**, 613 (2001)

[13] J. Thompson, R. Movshovich, Z. Fisk, F. Bouquet, N. Curro, R. Fisher, P. Hammel, H. Hegger, M. Hundley, M. Jaime, P. Pagliuso, C. Petrovic, N. Phillips, J. Sarrao, J. Magn. Magn. Mater. **226**, 5 (2001)

[14] E. Bauer, G. Hilscher, H. Michor, C. Paul, E.W. Scheidt, A. Gribanov, Y. Seropegin, H. Noël, M. Sigrist, P. Rogl, Phys. Rev. Lett. **92**, 027003 (2004)

[15] J.G. Bednorz, K.A. Müller, Z. Phys. B **64**, 189 (1986)

[16] H. Kamimura, H. Ushio, S. Matsuno, T. Hamada, *Theory of Copper Oxide Superconductors* (Springer-Verlag, Berlin, 2005)

[17] Y. Kamihara, H. Hiramatsu, M. Hirano, R. Kawamura, H. Yanagi, T. Kamiya, H. Hosono, J. Am. Chem. Soc. **128**, 10012 (2006)

[18] Y. Kamihara, T. Watanabe, M. Hirano, H. Hosono, J. Am. Chem. Soc. **130**, 3296 (2008)

[19] H. Takahashi, K. Igawa, K. Arii, Y. Kamihara, M. Hirano, H. Hosono, Nature **453**, 376 (2008)

[20] J.A. Wilson, J. Phys.: Condens. Matter **22**(20), 203201 (2010)

[21] A.P. Drozdov, M.I. Eremets, I.A. Troyan, V. Ksenofontov, S.I. Shylin, Nature **525**, 73 (2015)

[22] N.T. Huy, A. Gasparini, D.E. de Nijs, Y. Huang, J.C.P. Klaasse, T. Gortenmulder, A. de Visser, A. Hamann, T. Görlach, H. von Löhneysen, Phys. Rev. Lett. **99**, 067006 (2007)

[23] A. de Visser, *Encyclopedia of Materials: Science and Technology (pp 1-6)* (Elsevier, Oxford, 2010)

[24] J. Fay, D. Appel, Phys. Rev. B **22**, 3173 (1980)

[25] T.R. Kirkpatrick, D. Belitz, Phys. Rev. B **67**, 024515 (2003)

[26] D. Belitz, T.R. Kirkpatrick, Phys. Rev. B **69**, 184502 (2004)

[27] V.P. Mineev, T. Champel, Phys. Rev. B **69**, 144521 (2004)

[28] J.M. Kosterlitz, D.J. Thouless, J. Phys. C **5**, L124 (1972)

[29] J.M. Kosterlitz, D.J. Thouless, J. Phys. C **6**, 1181 (1973)

[30] Nobel prize in Physics, The Royal Swedish Academy of Sciences (2016)

[31] J.E. Moore, Nature **464**, 194 (2010)

[32] M.Z. Hasan, C.L. Kane, Rev. Mod. Phys. **82**, 3045 (2010)

[33] A. Kitaev, AIP Conference Proceedings **1134**(1) (2009)

[34] A.P. Schnyder, S. Ryu, A. Furusaki, A.W.W. Ludwig, AIP Conference Proceedings **1134** (2009)

[35] A. Stern, N.H. Lindner, Science **339**, 1179 (2013)

[36] P.W. Anderson, P. Morel, Phys. Rev. **123**, 1911 (1961)

[37] R. Balian, N.R. Werthamer, Phys. Rev. **131**, 1553 (1963)

[38] S.Q. Shen, *Topological Insulators-Dirac Equation in Condensed Matters* (Springer, Berlin, 2012)

[39] Y.S. Hor, A.J. Williams, J.G. Checkelsky, P. Roushan, J. Seo, Q. Xu, H.W. Zandbergen, A. Yazdani, N.P. Ong, R.J. Cava, Phys. Rev. Lett. **104**, 057001 (2010)

[40] T.V. Bay, T. Naka, Y.K. Huang, H. Luigjes, M.S. Golden, A. de Visser, Phys. Rev. Lett. **108**, 057001 (2012)

[41] K. Matano, M. Kriener, K. Segawa, Y. Ando, G.Q. Zheng, Nature Phys. **12**, 852 (2016)

[42] Y. Pan, A.M. Nikitin, G.K. Araizi, Y.K. Huang, Y. Matsushita, T. Naka, A. de Visser, Sci. Rep. **6**, 28632 (2016)

[43] S. Sasaki, Z. Ren, A.A. Taskin, K. Segawa, L. Fu, Y. Ando, Phys. Rev. Lett. **109**, 217004 (2012)

[44] G. Goll, M. Marz, A. Hamann, T. Tomanic, K. Grube, T. Yoshino, T. Takabatake, Physica B: Condens. Matter **403**, 1065 (2008)

[45] N.P. Butch, P. Syers, K. Kirshenbaum, A.P. Hope, J. Paglione, Phys. Rev. B **84**, 220504 (2011)

[46] T.V. Bay, T. Naka, Y.K. Huang, A. de Visser, Phys. Rev. B **86**, 064515 (2012)

[47] F.F. Tafti, T. Fujii, A. Juneau-Fecteau, S. René de Cotret, N. Doiron-Leyraud, A. Asamitsu, L. Taillefer, Phys. Rev. B **87**, 184504 (2013)

[48] Y. Pan, A.M. Nikitin, T.V. Bay, Y.K. Huang, C. Paulsen, B.H. Yan, A. de Visser, Europhys. Lett. **104**, 27001 (2013)

[49] G. Xu, W. Wang, X. Zhang, Y. Du, E. Liu, S. Wang, G. Wu, Z. Liu, X.X. Zhang, Sci. Rep. **4**, 5709 (2014)

[50] A.M. Nikitin, Y. Pan, X. Mao, R. Jehee, G.K. Araizi, Y.K. Huang, C. Paulsen, S.C. Wu, B.H. Yan, A. de Visser, J. Phys.: Condens. Matter **27**, 275701 (2015)

[51] Y. Nakajima, R. Hu, K. Kirshenbaum, A. Hughes, P. Syers, X. Wang, K. Wang, R. Wang, S.R. Saha, D. Pratt, J.W. Lynn, J. Paglione, Sci. Adv. **1**, e1500242 (2015)

[52] O. Pavlosiuk, D. Kaczorowski, P. Wiśniewski, Sci. Rep. **5**, 9158 (2015)

[53] G.R. Stewart, Rev. Mod. Phys. **56**, 755 (1984)

[54] J. Magn. Magn. Mater. **47**, 545 (1985)

[55] P.W. Anderson, Phys. Rev. **124**, 41 (1961)

[56] H. v. Löhneysen, A. Rosch, M. Vojta, P. Wölfle, Rev. Mod. Phys. **79**, 1015 (2007)

[57] M.A. Ruderman, C. Kittel, Phys. Rev. **96**, 99 (1954)

[58] J. Kondo, Prog. Theor. Phys. **32**, 37 (1964)

[59] H.v. Löhneysen, T. Pietrus, G. Portisch, H.G. Schlager, A. Schröder, M. Sieck, T. Trappmann, Phys. Rev. Lett. **72**, 3262 (1994)

[60] P. Gegenwart, F. Kromer, M. Lang, G. Sparn, C. Geibel, F. Steglich, Phys. Rev. Lett. **82**, 1293 (1999)

[61] O. Trovarelli, C. Geibel, S. Mederle, C. Langhammer, F.M. Grosche, P. Gegenwart, M. Lang, G. Sparn, F. Steglich, Phys. Rev. Lett. **85**, 626 (2000)

[62] J. Custers, P. Gegenwart, H. Wilhelm, K. Neumaier, Y. Tokiwa, O. Trovarelli, C. Geibel, F. Steglich, C. Pepin, P. Coleman, Nature **424**, 524 (2003)

[63] S.A. Grigera, R.S. Perry, A.J. Schofield, M. Chiao, S.R. Julian, G.G. Lonzarich, S.I. Ikeda, Y. Maeno, A.J. Millis, A.P. Mackenzie, Science **294**, 329 (2001)

[64] C. Pfleiderer, G.J. McMullan, S.R. Julian, G.G. Lonzarich, Phys. Rev. B **55**, 8330 (1997)

[65] M. Uhlarz, C. Pfleiderer, S.M. Hayden, Phys. Rev. Lett. **93**, 256404 (2004)

[66] P.G. Niklowitz, F. Beckers, G.G. Lonzarich, G. Knebel, B. Salce, J. Thomasson, N. Bernhoeft, D. Braithwaite, J. Flouquet, Phys. Rev. B **72**, 024424 (2005)

[67] S. Drotziger, C. Pfleiderer, M. Uhlarz, H.v. Löhneysen, D. Souptel, W. Löser, G. Behr, Phys. Rev. B **73**, 214413 (2006)

[68] H.v. Löhneysen, A. Schröder, T. Trappmann, M. Welsch, J. Magn. Magn. Mater. **108**, 45 (1992)

[69] M. Nicklas, M. Brando, G. Knebel, F. Mayr, W. Trinkl, A. Loidl, Phys. Rev. Lett. **82**, 4268 (1999)

[70] A. de Visser, M.J. Graf, P. Estrela, A. Amato, C. Baines, D. Andreica, F.N. Gygax, A. Schenck, Phys. Rev. Lett. **85**, 3005 (2000)

[71] D.A. Sokolov, M.C. Aronson, W. Gannon, Z. Fisk, Phys. Rev. Lett. **96**, 116404 (2006)

[72] R. Küchler, P. Gegenwart, J. Custers, O. Stockert, N. Caroca-Canales, C. Geibel, J.G. Sereni, F. Steglich, Phys. Rev. Lett. **96**, 256403 (2006)

[73] J.G. Sereni, T. Westerkamp, R. Küchler, N. Caroca-Canales, P. Gegenwart, C. Geibel, Phys. Rev. B **75**, 024432 (2007)

[74] T.P. Orlando, E.J. McNiff, S. Foner, M.R. Beasley, Phys. Rev. B **19**, 4545 (1979)

[75] U. Rauchschwalbe, Physica B+C **147**, 1 (1987)

[76] A. de Visser, PhD thesis, University of Amsterdam (1986)

[77] N.R. Werthamer, E. Helfand, P.C. Hohenberg, Phys. Rev. **147**, 295 (1966)

[78] R.A. Klemm, K. Scharnberg, Physica B+C **135**(1), 53 (1985)

[79] A.M. Clogston, Phys. Rev. Lett. **9**, 266 (1962)

[80] P.W. Anderson, W.F. Brinkman, Phys. Rev. Lett. **30**, 1108 (1973)

[81] K. Scharnberg, R.A. Klemm, Phys. Rev. B **22**, 5233 (1980)

[82] V.L. Ginzburg, Sov. Phys. JETP **4**, 153 (1957)

[83] R. Roussev, A.J. Millis, Phys. Rev. B **63**, 140504 (2001)

[84] A. de Visser, N.T. Huy, A. Gasparini, D.E. de Nijs, D. Andreica, C. Baines, A. Amato, Phys. Rev. Lett. **102**, 167003 (2009)

[85] T. Ohta, T. Hattori, K. Ishida, Y. Nakai, E. Osaki, K. Deguchi, N.K. Sato, I. Satoh, J. Phys. Soc. Jpn. **79**, 023707 (2010)

[86] T. Hattori, Y. Ihara, Y. Nakai, K. Ishida, Y. Tada, S. Fujimoto, N. Kawakami, E. Osaki, K. Deguchi, N.K. Sato, I. Satoh, Phys. Rev. Lett. **108**, 066403 (2012)

[87] D. Aoki, T.D. Matsuda, V. Taufour, E. Hassinger, G. Knebel, J. Flouquet, J. Phys. Soc. Jpn. **78**, 113709 (2009)

[88] Y. Tada, S. Takayoshi, S. Fijimoto, Phys. Rev. B **93**, 174512 (2016)

[89] V.P. Mineev, Phys. Rev. B **81**, 180504 (2010)

[90] V.P. Mineev, Phys. Rev. B **90**, 064506 (2014)

[91] E. Grüneisen, Ann. Phys. **39**, 257 (1912)

[92] P. Brommer, Physica B+C **112**(3), 343 (1982)

[93] N.H. van Dijk, *Dilatometry of heavy-fermion superconductors*. PhD thesis, University of Amsterdam (1994)

[94] A. Gasparini, *Quantum criticality in correlated metals, a Grüneisen parameter study*. PhD thesis, University of Amsterdam (2010)

[95] T. Barron, J. Collins, G. White, Advances in Physics **29**, 609 (1980)

[96] S. Chadov, X.L. Qi, J. Kübler, G.H. Fecher, C. Felser, S.C. Zhang, Nature Mat. **9**, 541 (2010)

[97] H. Lin, L.A. Wray, Y. Xia, S. Xu, S. Jia, R.J. Cava, A. Bansil, M.Z. Hasan, Nature Mat. **9**, 546 (2010)

[98] L. Fu, C.L. Kane, Phys. Rev. B **76**, 045302 (2007)

[99] J.E. Moore, L. Balents, Phys. Rev. B **75**, 121306 (2007)

[100] R. Roy, Phys. Rev. B **79**, 195322 (2009)

[101] H. Zhang, C.X. Liu, X.L. Qi, X. Dai, Z. Fang, S.C. Zhang,

[102] D. Hsieh, D. Qian, L. Wray, Y. Xia, Y.S. Hor, R.J. Cava, M.Z. Hasan, Nature **452**, 970 (2008)

[103] Y. Xia, D. Qian, D. Hsieh, L.Wray, A. Pal, H. Lin, A. Bansi, D. Grauer, Y.S. Hor, R.J. Cava, M.Z. Hasan, Nature Phys. **5**, 398 (2009)

[104] O. Pavlosiuk, D. Kaczorowski, X. Fabreges, A. Gukasov, P. Wiśniewski, Sci. Rep. **6**, 18797 (2016)

[105] J.W.F. Venderbos, V. Kozii, L. Fu, Phys. Rev. B **94**, 094522 (2016)

[106] L. Fu, Nature Phys. **12**, 822 (2016)

[107] Z. Liu, X. Yao, J. Shao, M. Zuo, L. Pi, S. Tan, C. Zhang, Y. Zhang, J. Am. Chem. Soc. **137**, 10512 (2015)

[108] Y. Qiu, K.N. Sanders, J. Dai, J.E. Medvedeva, W. Wu, P. Ghaemi, T. Vojta, Y.S. Hor, e-print: arXiv:1512.03519v1 (2015)

[109] Z. Wang, A.A. Taskin, T. Frölich, M. Braden, Y. Ando, Chem. Mater. **28**, 779 (2016)

[110] L.A. Wray, S.Y. Xu, Y. Xia, Y.S. Hor, D. Qian, A.V. Fedorov, H. Lin, A. Bansil, R.J. Cava, M.Z. Hasan, Nature Phys. **6**, 855 (2010)

[111] S. Yonezawa, K. Tajiri, S. Nakata, Y. Nagai, Z. Wang, K. Segawa, Y. Ando, Y. Maeno, Nature Phys. **10.1038/nphys3907** (2016)

[112] L. Fu, Phys. Rev. B **90**, 100509 (2014)

[113] Y. Nagai, H. Nakamura, M. Machida, Phys. Rev. B **86**, 094507 (2012)

[114] G.K. Araizi, *Fermi surface of the superconducting ferromagnet UCoGe*. MSc thesis, University of Amsterdam (2016)

[115] T.V. Bay, *Experimental investigation of potential topological and p-wave superconductors*. PhD thesis, University of Amsterdam, http://hdl.handle.net/11245/1.430490 (2014)

[116] K. van den Hoven, *Rotational symmetry breaking in the candidate topological superconductor $Sr_xBi_2Se_3$ probed by torque magnetometry*. BSc thesis, University of Amsterdam (2016)

[117] G.M. Schmiedeshoff, A.W. Lounsbury, D.J. Luna, S.J. Tracy, A.J. Schramm, S.W. Tozer, V.F. Correa, S.T. Hannahs, T.P. Murphy, E.C. Palm, A.H. Lacerda, S.L. Bud'ko, P.C. Canfield, J.L. Smith, J.C. Lashley, J.C. Cooley, Rev. Sci. Instrum. **77**, 123907 (2006)

[118] G.K. White, Cryogenics **1**, 151 (1961)

[119] R. Pott, R. Schefzyk, J. Phys. E: Sci. Instrum. **16**, 444 (1983)

[120] F.R. Kroeger, C.A. Swenson, J. Appl. Phys. **48**, 853 (1977)

[121] Attocube, *User manual*. http://www.attocube.com/attomotion/introduction/ (2011)

[122] D. Aoki, J. Flouquet, J. Phys. Soc. Jpn. **83**, 061011 (2014)

[123] A.D. Huxley, Physica C **514**, 368 (2015)

[124] F. Canepa, P. Manfrinetti, M. Pani, A. Palenzona, J. Alloy. Compd. **234**, 225 (1996)

[125] N.T. Huy, D.E. de Nijs, Y.K. Huang, A. de Visser, Phys. Rev. Lett. **100**, 077002 (2008)

[126] Y. Ihara, T. Hattori, K. Ishida, Y. Nakai, E. Osaki, K. Deguchi, N.K. Sato, I. Satoh, Phys. Rev. Lett. **105**, 206403 (2010)

[127] C. Stock, D.A. Sokolov, P. Bourges, P.H. Tobash, K. Gorfyk, F. Ronning, E.D. Bauer, K.C. Rule, A.D. Huxley, Phys. Rev. Lett. **107**, 187202 (2011)

[128] N.T. Huy, Y.K. Huang, A. de Visser, J. Magn. Magn. Mat. **321**, 2691 (2009)

[129] D. Aoki, J. Flouquet, J. Phys. Soc. Jpn. **81**, 011003 (2012)

[130] A. Gasparini, Y.K. Huang, J. Hartbaum, H. v. Löhneysen, A. de Visser, Phys. Rev. B **82**, 052502 (2010)

[131] E. Slooten, T. Naka, A. Gasparini, Y.K. Huang, A. de Visser, Phys. Rev. Lett. **103**, 097003 (2009)

[132] E. Hassinger, D. Aoki, G. Knebel, J. Flouquet, J. Phys. Soc. Jpn. **77**, 073703 (2008)

[133] G. Bastien, D. Braithwaite, D. Aoki, G. Knebel, J. Flouquet, Phys. Rev. B **94**, 125110 (2016)

[134] N.H. van Dijk, A. de Visser, J.J.M. Franse, A.A. Menovsky, Phys. Rev. B **51**, 12665 (1995)

[135] N.H. van Dijk, A. de Visser, J.J.M. Franse, L. Taillefer, J. Low Temp. Phys. **93**, 101 (1993)

[136] A.M. Adamska, L. Havela, S. Surble, S. Heathman, J. Pospíšil, S. Daniš, J. Phys.: Condens. Matter **22**, 275603 (2010)

[137] S. Mašková, A.M. Adamska, L. Havela, N.T.H. Kim-Ngan, J. Przewoźnik, S. Daniš, K. Kothapalli, A.V. Kolomiets, S. Heathman, H. Nakotte, H. Bordallo, J. Alloys Compd. **522**, 130 (2012)

[138] A. de Visser, J. Franse, A. Lacerda, P. Haen, J. Flouquet, Physica B **163**(1), 49 (1990)

[139] V.P. Mineev, e-print: arXiv:1002.3510v1 (2010)

[140] W. Knafo, T.D. Matsuda, D. Aoki, F. Hardy, G.W. Scheerer, G. Ballon, M. Nardone, A. Zitouni, C. Meingast, J. Flouquet, Phys. Rev. B **86**, 184416 (2012)

[141] K. Prokeš, A. de Visser, Y.K. Huang, B. Fåk, E. Ressouche, Phys. Rev. B **81**, 180407(R) (2010)

[142] M. Vališka, J. Pospíšil, A. Stunault, Y. Takeda, B. Gillon, Y. Haga, K. Prokeš, M.M. Abd-Elmeguid, G. Nenert, T. Okane, H. Yamagami, L. Chapon, A. Gukasov, A. Cousson, E. Yamamoto, V. Sechovský, J. Phys. Soc. Jpn. **84**, 084707 (2015)

[143] M. Taupin, J.P. Sanchez, J.P. Brison, D. Aoki, G. Lapertot, F. Wilhelm, A. Rogalev, Phys. Rev. B **92**, 035124 (2015)

[144] M.W. Butchers, J.A. Duffy, J.W. Taylor, S.R. Giblin, S.B. Dugdale, C. Stock, P.H. Tobash, E.D. Bauer, C. Paulsen, Phys. Rev. B **92**, 121107(R) (2015)

[145] E. Steven, A. Kiswandhi, D. Krstovska, J.S. Brooks, M. Almeida, A.P. Gonçalves, M.S. Henriques, G.M. Luke, T.J. Williams, Appl. Phys. Lett. **98**, 132507 (2011)

[146] D. Aoki, I. Sheikin, T.D. Matsuda, V. Taufour, G. Knebel, J. Flouquet, J. Phys. Soc. Jpn. **80**, 013705 (2011)

[147] G. Bastien, A. Gourgout, D. Aoki, A. Pourret, I. Sheikin, G. Seyfarth, J. Flouquet, G. Knebel, Phys. Rev. Lett. **117**, 206401 (2016)

[148] T.V. Bay, A.M. Nikitin, T. Naka, A. McCollam, Y.K. Huang, A. de Visser, Phys. Rev. B **89**, 214512 (2014)

[149] M. Samsel-Czekała, S. Elgazzar, P.M. Oppeneer, E. Talik, W. Walerczyk, R. Troć, J. Phys.: Condens. Mater **22**, 015503 (2010)

[150] S. Fujimori, T. Ohkochi, I. Kawasaki, A. Yasui, Y. Takeda, T. Okane, Y. Saitoh, A. Fujimori, H. Yamagami, Y. Haga, E. Yamamoto, Y. Onuki, Phys. Rev. B **91**, 174503 (2015)

[151] M.Z. Hasan, C.L. Kane, Rev. Mod. Phys. **82**, 3045 (2010)

[152] X.L. Qi, S.C. Zhang, Rev. Mod. Phys. **83**, 1057 (2011)

[153] D. Hsieh, Y. Xia, D. Qian, L. Wray, J.H. Dil, F. Meier, J. Osterwalder, L. Patthey, J.G. Checkelsky, N.P. Ong, A.V. Fedorov, H. Lin, A. Bansil, D. Grauer, Y.S. Hor, R.J. Cava, M.Z. Hasan, Nature **460**, 1101 (2009)

[154] M. Sato, Phys. Rev. B **81**, 220604 (2010)

[155] L. Fu, E. Berg, Phys. Rev. Lett. **105**, 097001 (2010)

[156] M. Kriener, K. Segawa, Z. Ren, S. Sasaki, Y. Ando, Phys. Rev. Lett. **106**, 127004 (2011)

[157] S. Sasaki, M. Kriener, K. Segawa, K. Yada, Y. Tanaka, M. Sato, Y. Ando, Phys. Rev. Lett. **107**, 217001 (2011)

[158] S. Sasaki, T. Mizushima, Physica C **514**, 206 (2015)

[159] N. Levy, T. Zhang, J. Ha, F. Sharifi, A.A. Talin, Y. Kuk, J.A. Stroscio, Phys. Rev. Lett. **110**, 117001 (2013)

[160] J.A. Schneeloch, R.D. Zhong, Z.J. Xu, G.D. Gu, J.M. Tranquada, Phys. Rev. B **91**, 144506 (2015)

[161] T. Asaba, B.J. Lawson, C. Tinsman, L. Chen, P. Corbae, G. Li, Y. Qiu, Y.S. Hor, L. Fu, L. Li, e-print: arXiv:1603.04040v1 (2016)

[162] Y. Zhou, X. Chen, R. Zhang, J. Shao, X. Wang, C. An, Y. Zhou, C. Park, W. Tong, L. Pi, Z. Yang, C. Zhang, Y. Zhang, Phys. Rev. B **93**, 144514 (2016)

[163] K. Kirshenbaum, P.S. Syers, A.P. Hope, N.P. Butch, J.R. Jeffries, S.T. Weir, J.J. Hamlin, M.B. Maple, Y.K. Vohra, J. Paglione, Phys. Rev. Lett. **111**, 087001 (2013)

[164] P.L. Krotkov, V.P. Mineev, Phys. Rev. B **65**, 224506 (2002)

[165] Shruti, V.K. Maurya, P. Neha, P. Srivastava, S. Patnaik, Phys. Rev. B **92**, 020506(R) (2015)

[166] M.G. Haase, T. Schmidt, C.G. Richter, H. Block, W. Jeitschko, J. Solid State Chem. **168**, 18 (2002)

[167] T. Graf, C. Felser, S.S.P. Parkin, Progress Sol. State Chem. **39**, 1 (2011)

[168] W. Feng, D. Xiao, Y. Zhang, Y. Yao, Phys. Rev. B **82**, 235121 (2010)

[169] B.A. Bernevig, T.L. Hughes, S.C. Zhang, Science **314**, 1757 (2006)

[170] B. Yan, A. de Visser, MRS Bulletin **39**, 859 (2014)

[171] A. Kitaev, AIP Conf. Proc. **1134**, 22 (2009)

[172] A.P. Schnyder, S. Ryu, A. Furusaki, A.W.W. Ludwig, AIP Conf. Proc. **1134**, 10 (2009)

[173] P.A. Frigeri, D.F. Agterberg, A. Koga, M. Sigrist, Phys. Rev. Lett. **92**, 097001 (2004)

[174] J. Goraus, A. Ślebarski, M. Fijałkowski, J. Phys.: Condens. Matter **25**, 176002 (2013)

[175] K. Gofryk, D. Kaczorowski, T. Plackowski, A. Leithe-Jasper, Y. Grin, Phys. Rev. B **72**, 094409 (2005)

[176] K.R. Lea, M.J.M. Leask, W.P. Wolf, J. Phys. Chem. Solids **23**, 1381 (1962)

[177] C. Domb, *The Critical Point* (Taylor and Francis, London, 1996)

[178] G. Kresse, J. Furthmüller, Phys. Rev. B **54**, 11169 (1996)

[179] B.R. Matthias, T.H. Geballe, V.B. Compton, Rev. Mod. Phys. **35**, 1 (1963)

[180] A. Kapitulnik, E-MRS Fall meeting, 15-19 Sept. 2014, Warsaw, presentation in Symposium F (2014)

[181] A. Kapitulnik, APS March Meeting, 2-6 March 2015, San Antonio, meetings.aps.org/link/BAPS.2015.MAR.T25.5 (2015)

[182] T.M. Riedemann, *Heat capacities, magnetic properties and resistivity of ternary RPdBi alloys where R = La, Nd, Gd, Dy, Er, and Lu*. MSc thesis, Iowa State University (1996)

[183] J. Jensen, A.R. Mackintosh, *Rare Earth Magnetism* (Clarendon Press, Oxford, 1991)

[184] R.S.K. Mong, A.M. Essin, J.E. Moore, Phys. Rev. B **81**, 245209 (2010)

[185] R.A. Müller, N.R. Lee-Hone, L. Lapointe, D.H. Ryan, T. Pereg-Barnea, A.D. Bianchi, Y. Mozharivskyj, R. Flacau, Phys. Rev. B **90**, 041109(R) (2014)

[186] R.N. Shelton, J. Less Comm. Metals **94**, 69 (1983)

[187] P.H. Hor, R.L. Meng, Y.Q. Wang, L. Gao, Z.J. Huang, J. Bechtold, K. Forster, C.W. Chu, Phys. Rev. Lett. **58**, 1891 (1987)

[188] J. Yang, X.L. Shen, W. Lu, W. Yi, Z. Li, Z.A. Ren, G.C. Che, X.L. Dong, L.L. Sun, F. Zhou, Z.X. Zhao, New. J. Phys. **11**, 025005 (2009)

[189] R.J. Cava, H. Takagi, H.W. Zandbergen, J.J. Krajewski, W.F.P. Jr., T. Siegrist, B. Batlogg, R.B. van Dover, R.J. Felder, K. Mizuhashi, J.O. Lee, H. Eisaki, S. Uchida, Nature **367**, 252 (1994)

Summary

Superconductivity is a fascinating phenomenon. Over the last hundred years, researchers from all over the world have been working on superconducting materials. New superconductors are discovered on a daily basis, and superconductivity has found many applications. Nevertheless, we are still far away from understanding the mechanisms which drive superconductivity in several important classes of superconductors, like cuprates, pnictides and heavy-fermion compounds. In this thesis, we concentrate on three different unconventional superconductors.

UCoGe belongs to the family of superconducting ferromagnets. The physics of such systems is extremely rich. First of all, the coexistence of superconductivity and ferromagnetism within a single phase is quite unique. Only a few materials exhibit such a coexistence: UGe_2, URhGe and UCoGe. Secondly, these materials are strongly correlated electron systems with a heavy-fermion nature based on the uranium $5f$-electrons, which are responsible for both superconductivity and ferromagnetism. The combination of all mentioned properties makes UCoGe a unique laboratory tool to study ferromagnetic quantum criticality and the related effects, such as strong spin fluctuations and superconductivity in the vicinity of the quantum critical point.

Recently, a new class of unconventional superconductors received ample attention, topological superconductors, partly because it was theoretically predicted that they can host Majorana zero modes at the surface. Currently, two approaches to search for topological superconductors have been quite successful. First, doping of topological insulators may transform the material into a superconductor. Examples of such systems are $Sr_xBi_2Se_3$ and $Cu_xBi_2Se_3$. Recently, a surprising discovery was reported: the in-plane upper-critical field in these materials is strongly anisotropic. This finds an explanation in terms of nematic superconductivity, where the order parameter is a vector and can depend strongly on the direction of magnetic field. The second approach is based on the idea to search for topological superconductors

among materials which contain heavy elements. The presence of heavy elements, such as rare earth atoms, within the crystal, can create a band inversion in the electronic structure due to the strong spin-orbit coupling. Electronic structure calculations predicted a large number of compounds in which non-trivial topology may be realized. An example of such a system discussed in this thesis is HoPdBi, which is a member of the half-Heusler family with non-trivial topology.

An important part of this thesis project was devoted to the design and construction of a dilatometer with very high sensitivity that could be rotated in the magnetic field. Moreover, the dilatometer needed to be operated under extreme conditions, notably at milli-Kelvin temperatures and high magnetic fields. The design of the thermal expansion cell was chosen to satisfy the following criteria: a small size, a low cell effect, non-magnetic, and high resolution. For this a parallel-plate capacitance dilatometer was constructed. The resolution of the thermal expansion cell at low temperature is 0.03 Å. In order to conduct field-angle dependent measurements, a rotation mechanism was implemented. A piezo-electric rotator mounted onto a gear system was installed. The angular resolution of the device is 0.05°. A detailed description of the dilatometer, the rotation mechanism, the calibration of the system and other technical issues are presented in Chapter 3. In addition, the cryogenic equipment, other experimental techniques and the sample characterization are discussed in Chapter 3.

In the following two chapters, we focus on the superconducting and ferromagnetic properties of UCoGe. The phase diagram of this superconducting ferromagnet has been determined by dilatometry, a bulk sensitive probe. Measurements of the thermal expansion coefficient on a high-quality single crystal of UCoGe around the Curie point and the superconducting transition temperature in magnetic fields up to 12 T applied along the orthorhombic axes have been carried out. A precise orientation of the magnetic field with respect to the crystal axes was obtained by *in situ* rotation of the cell using the piezo-electric motor. The field variation of the superconducting and ferromagnetic transition temperatures was established. For small fields $B \parallel c$ the ferromagnetic transition becomes a cross-over and superconductivity is rapidly suppressed ($B_{c2} = 0.5$ T when $T \to 0$). For $B \parallel a, b$ the Curie point and superconductivity persist. With our bulk technique, we confirm the unusual S-shape of the upper-critical field for $B \parallel b$ and the enhancement of superconductivity above 6 T. At the same time, the Curie point shifts towards lower temperatures. This lends further support to theoretical proposals of spin-fluctuation mediated re-

inforcement of superconductivity for $B \parallel b$.

Next, an extensive magnetoresistance study on single crystals of UCoGe for a magnetic field directed along the c-axis is presented. We confirm a pronounced structure in the magnetoresistance, which takes place when the component of the field parallel to the c-axis reaches a value B^* = 9 T. Measurements of B^* as a function of pressure up to p = 1.5 GPa show a quadratic increase $B^*(p) = B^*(0) + bp^2$, where b = 3.0 T/GPa^2. The characteristic field B^* = 9 T is also observed in magnetostriction and magnetic torque measurements, albeit less prominent. The Fermi surface of UCoGe has been studied by quantum oscillations in the magnetoresistance. A pair of small Fermi surface pockets with a heavy effective mass was detected. Our results are in good agreement with recent magnetoresistance and thermopower measurements that revealed the presence of multiple Lifshitz transitions as a function of the applied magnetic field $B \parallel c$. This demonstrates the Fermi surface of UCoGe undergoes a dynamic reconstruction under large magnetic fields.

An important part of this thesis is dedicated to topological superconductors. The recent discovery of nematic superconductivity in $Sr_xBi_2Se_3$ provided the motivation to investigate this phenomenon under high pressures up to 2.2 GPa. Therefore, Chapter 6 focuses on a high-pressure study of $Sr_{0.15}Bi_2Se_3$ in order to investigate the unusual basal-plane anisotropy of the upper-critical field. The superconducting transition temperature is found to be rapidly depressed with a critical pressure of $\sim$ 3.5 GPa. $B_{c2}(T)$ has been determined for the B-field applied along two orthogonal crystal directions, a and a^*, in the basal plane. The pronounced two-fold basal-plane anisotropy $B_{c2}^{a}/B_{c2}^{a^*} = 3.2$ at $T = 0.3$ K is robust under pressure and attains a value of ~ 5 at the highest pressure (2.2 GPa). The two-fold anisotropy of $B_{c2}(T)$ provides solid evidence for rotational symmetry breaking in the D_{3d} crystal structure. This puts stringent conditions on the superconducting order parameter, namely it should belong to a two-dimensional representation (E_u). Rotational symmetry breaking seems to be ubiquitous in the family of doped Bi_2Se_3-based superconductors. This offers an exciting opportunity to study nematic superconductivity with a two-component order parameter.

In Chapter 7, the transport, magnetic and thermal properties of the half-Heusler antiferromagnet HoPdBi are discussed. We discovered superconductivity at 1.9 K as evidenced by electrical resistivity and ac-susceptibility data. However, the transition to bulk superconductivity sets in at a lower temperature of 0.75 K. The Néel temperature T_N is 2.0 K as determined by thermal expansion and dc-magnetization

measurements. The superconducting and magnetic phase diagram in the $B - T$ plane has been determined: superconductivity is confined to the antiferromagnetic phase. Electronic structure calculations show HoPdBi is a topological semimetal with a band inversion at the Γ-point. This is in-line with the semimetallic behaviour observed in the electrical resistivity and the low carrier concentration extracted from the Shubnikov-de Haas effect. HoPdBi belongs to the half-Heusler REPdBi series with a topological band structure and presents a new laboratory tool to study the interplay of antiferromagnetic order, superconductivity, and topological quantum states.

Samenvatting

Supergeleiding is een fascinerende eigenschap. In de afgelopen honderd jaar hebben talloze wetenschappers uit de hele wereld onderzoek gedaan aan supergeleidende materialen. Nieuwe supergeleiders worden nog bijna dagelijks ontdekt. Daarnaast zijn er veel belangrijke toepassingen voor supergeleiding. Desalniettemin is het mechanisme dat supergeleiding veroorzaakt in diverse belangrijke groepen van supergeleiders, zoals de hoge-T_c koperoxiden, de pnictiden en zware-fermion verbindingen, verre van begrepen. In dit proefschrift worden drie verschillende onconventionele supergeleiders onderzocht.

UCoGe behoort tot de groep van supergeleidende ferromagneten. Deze materialen vertonen een rijke natuurkunde. Ten eerste, de unieke coëxistentie van supergeleiding en ferromagnetisme in één en dezelfde fase. Een dergelijke coëxistentie is gevonden in slechts drie materialen: UGe_2, URhGe en UCoGe. Ten tweede, deze materialen zijn alle sterk gecorreleerde elektron systemen, waarbij de zware-fermion toestand veroorzaakt wordt door de $5f$-elektronen die tevens verantwoordelijk zijn voor zowel supergeleiding als ferromagnetisme. De combinatie van al deze eigenschappen maakt UCoGe een uniek laboratoriumgereedschap om de ferromagnetische quantum kritische toestand te onderzoeken, en de daaraan gerelateerde effecten, zoals sterke spinfluctuaties en supergeleiding bij het quantum kritisch punt.

In de afgelopen jaren heeft een nieuwe groep van onconventionele supergeleiders veel belangstelling getrokken, de topologische supergeleiders. Dit vooral omdat theorie voorspelt dat aan het oppervlak van deze supergeleiders zogeheten Majorana *zero modes* kunnen bestaan. Twee methoden om topologische supergeleiders te maken zijn succesvol gebleken. Ten eerste, het intercaleren van een topologische isolator kan het materiaal veranderen in een supergeleider. Voorbeelden hiervan zijn $Sr_xBi_2Se_3$ en $Cu_xBi_2Se_3$. Onlangs is in deze geïntercaleerde materialen een verrassende ontdekking gedaan: het bovenste kritische veld, gemeten voor een mag-

neetveld aangelegd in het basis vlak, is sterk anisotroop. Dit kan verklaard worden door nematische supergeleiding, waarbij de orde-parameter zich als een vector gedraagt waarvan de richting gerelateerd is aan de richting van het magneetveld. De tweede methode om topologische supergeleiders te maken is om verbindingen met zware elementen te onderzoeken. De aanwezigheid van zware elementen, zoals zeldzame aard atomen, in de kristalstructuur, kan een sterke spin-baan koppeling tot gevolg hebben, hetgeen aanleiding kan geven tot inversie van de elektronenbanden. Theoretische berekeningen van de elektronenbandenstructuur voorspellen dat in een groot aantal verbindingen zo'n niet triviale topologie kan bestaan. Een voorbeeld van een dergelijk systeem met bandinversie én supergeleiding dat behandeld wordt in dit proefschrift is de halve-Heusler verbinding HoPdBi.

Een belangrijk onderdeel van het promotieonderzoek was gewijd aan het ontwerpen en construeren van een gevoelige meetcel voor thermische uitzetting, die tevens gedraaid kon worden in een uitwendig magneetveld. Bovendien, moest de meetcel gebruikt kunnen worden onder extreme condities: bij milliKelvin temperaturen en in zeer sterke magneetvelden. Het ontwerp van de meetcel werd mede bepaald door de volgende randvoorwaarden: kleine afmeting, een gering cel effect, niet-magnetisch materiaal en een hoge resolutie. Er is gekozen voor een capacitieve meetcel gebaseerd op een vlakke-plaat condensator. De resolutie van de meetcel bij lage temperatuur is 0.03 Å. Om ook de hoekafhankelijkheid van het magneetveld te kunnen meting werd de meetcel gemonteerd op een draai mechanisme. Hiervoor werd een piëzo-elektrische rotator geïnstalleerd. De hoek resolutie bedraagt 0.05°. Een gedetailleerde beschrijving van de meetcel, het rotatiemechanisme, de ijking van de meetcel en rotator, en andere technische aspecten worden gepresenteerd in Hoofdstuk 3. Ook worden daar de cryogene apparatuur, de andere gebruikte experimentele meetmethoden en de karakterisatie van de gemeten preparaten behandeld.

In de volgende twee hoofdstukken focuseren we op de supergeleidende en ferromagnetische eigenschappen van UCoGe. Het fasediagram van deze supergeleidende ferromagneet is bepaald door thermische uitzetting, een techniek die de bulk van het preparaat meet. De thermische uitzettingscoëfficiënt is gemeten aan een eenkristal van UCoGe van hoge kwaliteit. Er is gemeten rond de Curie temperatuur en de supergeleidende overgang in magneetvelden tot 12 T aangelegd langs de orthorhombische kristalassen. Voor de precieze oriëntatie van het magneetveld langs de kristalassen is gebruik gemaakt van *in situ* rotatie van de meetcel met de piëzo-elektrische motor. Het effect van het magneetveld op de supergeleidende en

ferromagnetische overgangstemperaturen is bepaald. Voor kleine magneetvelden $B \parallel c$ wordt de ferromagnetische overgang een *cross-over* en supergeleiding snel onderdrukt ($B_{c2} = 0.5$ T voor $T \to 0$). For $B \parallel a, b$ blijven het Curie punt en de supergeleiding meetbaar tot hoge velden. Met onze bulk techniek bevestigen we de ongebruikelijke *S*-vorm van het bovenste kritische veld voor $B \parallel b$ en de versterking van supergeleiding boven 6 T. Tegelijkertijd schuift het Curie punt naar lagere temperaturen. Dit ondersteunt theoretische modellen waarin supergeleiding versterkt wordt door spin-fluctuaties voor $B \parallel b$.

Vervolgens wordt een uitgebreide studie aan eenkristallen van UCoGe voor het magneetveld langs de *c*-as gepresenteerd. We bevestigen een uitgesproken structuur in de magnetoweerstandscurve, die optreedt wanneer de component van het magneetveld, B^*, langs de *c*-as een waarde van 9 T bereikt. Metingen van B^* als een functie van de aangelegde druk tot p = 1.5 GPa laten een kwadratische toename zien: $B^*(p) = B^*(0) + bp^2$, met b = 3.0 T/GPa^2. Het karakteristieke veld B^* is ook waargenomen in magnetostrictie en magnetische torsie metingen, maar is daar beduidend minder goed zichtbaar. Het Fermi oppervlak van UCoGe is bestudeerd met behulp van quantumoscillaties in de magnetoweerstand. Een tweetal kleine *pockets* met een hoge effectieve massa zijn gedetecteerd. Onze resultaten zijn in goede overeenstemming met recente metingen van de magnetoweerstand en thermospanning die een reeks van Lifshitz overgangen laten zien als functie van het magneetveld $B \parallel c$. Dit toont aan dat het Fermi oppervlak van UCoGe een dynamische reconstructie ondergaat als functie van het magneetveld.

Een belangrijk onderdeel van dit proefschrift is gewijd aan topologische supergeleiders. De recente ontdekking van nematische supergeleiding in $Sr_xBi_2Se_3$ leverde de motivatie om dit verschijnsel te onderzoeken onder hoge druk tot 2.2 GPa. In Hoofdstuk 6 is de focus derhalve op een hoge-druk studie van $Sr_{0.15}Bi_2Se_3$ teneinde de ongebruikelijke anisotropie van het bovenste kritische veld voor een magneetveld in het basis vlak te onderzoeken. De supergeleidende overgangstemperatuur neemt snel af als functie van de druk en wordt nul bij de kritische druk $\sim$ 3.5 GPa. $B_{c2}(T)$ is bepaald met het magneetveld gericht langs twee orthogonale richtingen, *a* en *a**, in het basis vlak. De uitgesproken tweevoudige anisotropie $B^a_{c2}/B^{a^*}_{c2} = 3.2$ bij $T = 0.3$ K persisteert onder druk en bereikt een waarde van $\sim$ 5 bij de hoogste druk (2.2 GPa). De tweevoudige anisotropie van $B_{c2}(T)$ levert overtuigend bewijs voor een gebroken rotatiesymmetrie in de D_{3d} kristalstructuur. Dit leidt tot strenge voorwaarden wat betreft de supergeleidende orde-parameter, deze dient namelijk

een twee-dimensionale representatie (E_u) te hebben. Gebroken rotatiesymmetrie is ook gevonden in andere leden van de familie van gelegeerde Bi_2Se_3 supergeleiders. Dit biedt een fascinerende mogelijkheid om nematische supergeleiding met ordeparameter met twee-componenten te bestuderen.

In Hoofdstuk 7 worden de transport, magnetische en thermische eigenschappen van de halve-Heusler antiferromagneet HoPdBi bediscussieerd. We hebben supergeleiding ontdekt bij een temperatuur van 1.9 K door middel van metingen van de elektrische weerstand en ac-susceptibiliteit. Bulk supergeleiding treedt echter pas op bij een lagere temperatuur, beneden 0.75 K. De Néel temperatuur T_N is 2.0 K en werd bepaald door thermische uitzettings- en dc-magnetizatiemetingen. Het supergeleidende en magnetische fasediagram in het $B - T$ vlak is bepaald: supergeleiding is begrensd door de antiferromagnetische fase. Berekeningen van de elektronstructuur laten zien dat HoPdBi een topologisch semi-metaal is met een bandinversie in het Γ-punt. Dit is in overeenstemming met het semi-metallische gedrag gemeten in de elektrische weerstand en de lage ladingsdragerdichtheid bepaald door het Shubnikov-de Haas effect. HoPdBi behoort tot de halve-Heusler REPdBi reeks met een topologische bandinversie en is een nieuw laboratoriumgereedschap om de wisselwerking tussen antiferromagnetische ordening, supergeleiding en topologische quantumtoestanden te bestuderen.

List of publications

1. A.M. Nikitin, J. Geldhof, Y.K. Huang, D. Aoki and A. de Visser *"Superconducting and ferromagnetic phase diagram of UCoGe probed by thermal expansion"* (2017) accepted for publication in Phys. Rev. B (Chapter 4)

2. A.M. Nikitin, Y. Pan, Y.K. Huang, T. Naka and A. de Visser *"High-pressure study of the basal-plane anisotropy of the upper critical field of the topological superconductor $Sr_xBi_2Se_3$"* (2016) Phys. Rev. B 94, 144516 (Chapter 6)

3. A.M. Nikitin, Y. Pan, X. Mao, R. Jehee, G.K. Araizi, Y.K. Huang, C. Paulsen, S.C. Wu, B.H. Yan and A. de Visser *"Magnetic and superconducting phase diagram of the half-Heusler topological semimetal HoPdBi"* (2015) J. Phys.: Condens. Matter 27, 275701 (Chapter 7)

4. Y. Pan, A.M. Nikitin, G.K. Araizi, Y.K. Huang, Y. Matsushita, T. Naka and A. de Visser *"Rotational symmetry breaking in the topological superconductor $Sr_xBi_2Se_3$"* (2016) Sci. Rep. 6, 28632

5. T. Naka, A.M. Nikitin, Y. Pan, A. de Visser, T. Nakane, F. Ishikawa, Y. Yamada, M. Imai and A. Matsushita *"Composition induced metal-insulator quantum phase transition in the Heusler type Fe_2VAl"* (2016) J. Phys.: Condens. Matter 28, 285601

6. Y. Pan, A.M. Nikitin, D. Wu, Y.K. Huang, A. Puri, S. Wiedmann, U. Zeitler, E. Frantzeskakis, E. van Heumen, M.S. Golden and A. de Visser *"Quantum oscillations of the topological surface states in low carrier concentration crystals of*

$Bi_{2-x}Sb_xTe_{3-y}Se_y$" (2016) Solid State Comm. 227, 13-18

7. T.V. Bay, A.M. Nikitin, T. Naka, A. McCollam, Y.K. Huang and A. de Visser *"Angular variation of the magnetoresistance of the superconducting ferromagnet UCoGe"* (2014) Phys. Rev. B 89, 214512

8. Y. Pan, A.M. Nikitin, T.V. Bay, Y.K. Huang, C. Paulsen, B.H. Yan and A. de Visser *"Superconductivity and magnetic order in the noncentrosymmetric half-Heusler compound ErPdBi"* (2013) Europhys. Letters 104, 27001

9. A.M. Nikitin, M.M. Borisov, E.Kh. Mukhamedzhanov, M.V. Kovalchuk, S. Sajti, F. Tancziko, L. Deak, L. Bottyan, Yu.N. Khaydukov, V.L. Aksenov *"Precision structural diagnostics of layered superconductor/ferromagnet nanosystems V/Fe by reflectometry and diffuse scattering of synchrotron radiation"* (2011) Crystallography Reports 56, 5, 858

Acknowledgements

Many people contribute directly and indirectly to this thesis. I would like to thank my supervisors, colleagues, collaborators, friends and family.

Anne de Visser, thank you very much for supervising me on daily basis. All my knowledge about low-temperature experiments and heavy-fermion physics is coming from you. Your patience and professionalism made my PhD successful. I learn from you what a good scientist means. You have been more than just a supervisor to me. Thanks for a friendly atmosphere in the lab, your time, guidance, wisdom and support, conferences, publications and this thesis. Dank U wel!

Mark Golden, thank you for being my promotor. Your advice and comments on my presentations taught me a lot. I have learned from you how to negotiate with funding agencies and how to lead the group. Thanks for your calm and support, especially with regards to prolongation of my contract with FOM. Besides science, I really enjoyed BBQ's and dinners at your place!

One of the important aspects of the experimental research is high-quality crystals. Thanks to Yingkai Huang for teaching me how to grow polycrystalline samples, providing with high-quality single crystals, helping with X-ray diffraction and Laue backscattering measurements, annealing procedure. I would like to thank Nguyen Thanh Huy and Dai Aoki (Tohoku University, Japan) for synthesising high-quality single crystals of UCoGe.

The core of my PhD project was the technical part. George Schmiedeshoff (Occidental College, USA), thank you for letting me use your design of the dilatometer, providing the drawings and helpful discussions on the early stage of the project. I highly appreciate professionalism and support of the people from Technology Centre of the University of Amsterdam. Ron Manuputy, thank you for designing the rotation mechanism of the dilatometer, all the additional drawings and manufacturing of some parts of it. Harry Beukers, you have made first parts of the dilatometer, thank you for this. Johan Mozes, thank you for manufacturing the dilatometer and

many other miniature parts. I appreciate your high performance and always being treating my project with priority. Gert Jan Bon, Fred van Anrooij, Tijs van Roon, Johan Soede and Alix Wattjes, without your help it would have been impossible to finalise the project. Special thanks go to software guru Gerrit Hardeman. Gerrit, with help of your Labview skills the measurements became fully automated, which saved me a lot of time! Huib Luigjes and Hugo Schlatter, thank you for your help with operating the spark-cutting machine, polishing samples, replacing and repairing pumps.

I have been lucky to complement the research using external facilities. I owe gratitude to Alix McCollam (High Field Magnet Laboratory, Nijmegen) for a possibility to work with extremely high magnetic fields. Alix, thank you for your passion in searching quantum oscillations and providing the torque cantilever. Lucas Tang (High Field Magnet Laboratory, Nijmegen), it was nice to do experiments together even very late at night and early in the morning. Many thanks go to Carley Paulsen (Néel Institute, France) for measuring our samples and helpful discussions. Thanks to Binhai Yang (Max Plank Institute for Chemical Physics of Solids, Germany) for calculating the electronic structure of HoPdBi. During my time in Amsterdam, I gained a lot of skills. I was very lucky to meet Takashi Naka (National Institute for Materials Science, Japan), who has taught me how to work with a pressure cell. Takashi, it was always pleasant to work with you.

I would like to acknowledge FOM for financial support and Annette Bor and Maria Teuwissen for constant and quick help. Thanks to secretaries of the Van der Waals – Zeeman Institute, Rita Vinig, Anne-Marieke Crommentuijn and Natalie Wells, for the administration assistance.

Most of the time during PhD project I have spent in the lab working with amazing people. Many of these people have become my close friends. Tran Van Bay, thank you for teaching me how to use the cryogenic equipment. It was very pleasant to work and to have fun with you both in Amsterdam and at the conferences. Yu Pan, I respect your productivity and hardworking ability. After four year of working together shoulder to shoulder, you became to me like a sister, thank you for that. Nick de Jong, thank you for showing the Dutch view on many aspects of life. I really enjoyed our parties and fun activities. Alona Tytarenko, thank you for your energy and smile. Since you joined the group, the lab environment became more positive and pleasant. Shyama Ramankutty, thanks for helping with filling helium. George Araizi Kanoutas, it was interesting to work with you and thank you for being my

paranymph. Dona Cherian, thank you for your help with Latex. Bo Shi, Emmanouil Frantzeskakis, Erik Sloten, thank you for having nice lunches together. I would like to thank all the bachelor and master student who have worked in our lab: Wouter, Kris, Mengqi, Roos, Marc, Joost, Koen, Gijsbert, Stef, Jans. I would like to express my gratitude to my friends: Tomislav Suhina, Tatu Kumpulainen, Eliala Salvadori, Stefanos Tserkezis. Eliala, thanks for being my paranymph.

Виктор Лазаревич Аксёнов (МГУ, ОИЯИ) и Дмитрий Ремович Хохлов (МГУ), благодарю вас за рекомендации и советы. Энвер Хамзяевич Мухамеджанов (Курчатовский Институт) и Юрий Николаевич Хайдуков (ОИЯИ, MPI), спасибо вам за обучение премудростям экспериментальной физики. Зоя Анатольевна Пальгова, Сергей Владимирович и Владимир Иванович Калашниковы, Андрей Сергеевич Рудкевич, Роман Григорьевич Хазанкин, спасибо вам за то, что привили любовь к точным наукам. Благодарю всех русскоговорящих друзей за то, что скрасили мое пребывание в Амстердаме: Сергей Безрукавников, Инна Медведева, Наташа Втюрина, Миша Белоносов, Давид Давтян, Сергей Пятченков, Денис Курлов, Володя Гритцев, Маша Чугай, Дина Петрова.

Успешное завершение аспирантуры было бы не возможно без поддержки моей большой семьи. Мама и Папа, спасибо вам огромное за постоянную поддержку, любовь и понимание. Вы, как никто другой, знаете, как не просто мне иногда было продолжать. Спасибо вам за то, что научили меня трудолюбию собственным примером. Пока я занимался наукой, мои братья успели увеличить количество членов нашей семьи, с чем их сердечно поздравляю. Алексей, ты был для меня примером еще с ранних лет и продолжаешь им быть. Поздравляю тебя и Эльвиру с рождением Софьи и желаю не останавливаться на этом! Дима, твоя энергия и позитивный взгляд на мир всегда меня вдоновляют. Желаю тебе, Вике, Максимке и Анне счастья и любви! Спасибо Ирине Дортман за дизайн обложки. Бабушка, дедушка, спасибо, что вы с нами, желаю вам долгих лет жизни. Благодарю всех моих родственников за поддержку и веру в меня. И в завершении, хочу поблагодарить Ирину Росете Полякову. Иришка, спасибо тебе за поддержку и любовь.